DEPARTMENT OF PHYSICS
UNIVERSITY OF JYVÄSKYLÄ
RESEARCH REPORT No. 4/2005

PROBING NON-YRAST STRUCTURES OF ^{186}Pb IN A RDT MEASUREMENT EMPLOYING THE JUROGAM ARRAY

BY
JANNE PAKARINEN

Academic Dissertation
for the Degree of
Doctor of Philosophy

Jyväskylä, Finland
August 2005

ISBN 978-951-39-3161-2
URN:ISBN:978-951-39-3161-2

Preface

The work presented has been carried out during the years 2000-2005 at the Accelerator laboratory of the University of Jyväskylä, where I had the privilege of being a member of the γ-group. The members of the group have changed during my post-graduate studies, but the spirit has always been warm and inspiring. The close co-operation with the RITU group has created a pleasant, stressless and educational working environment. This also holds for the staff of the mechanical and electronics workshops as well as for the cyclotron crew, with whom it has been an honour to work with.

I am grateful to my supervisor Professor Rauno Julin for his invaluable guidance not only in my studies, but also for his help with numerous applications, writing of publications and, especially, this thesis. Dr. Sakari Juutinen's contribution to the data analysis and his enlightenment of various phenomena in nuclei are highly acknowledged.

I wish to thank Dr. Paul Greenlees for his comments during the writing of my thesis. Thanks to Mr. Panu Rahkila for his help with the GRAIN software package and sort code. These two gentlemen deserve thanks also for some of the figures presented in this work. I would also like to thank Dr. Pete Jones for always providing help with the data acquisition problems when it was needed and Dr. Juha Uusitalo for fruitful discussions about the RITU separator and fusion-evaporation reactions.

I am indebted to my closest colleagues, especially Mr. Ari-Pekka Leppänen, Mr. Tuomas Grahn, Mr. Markus Nyman and Mr. Iiro Riihimäki with whom I have shared the glorious working hours, lunch breaks, international summerschools and conferences as well as hilarious freetime.

Financial support from the Graduate School in Particle and Nuclear Physics, Vilho, Yrjö and Kalle Väisälä and Magnus Ehrnrooth foundations is gratefully acknowledged.

To my mother and father, sister and brother and my loving wife Sanna,

Jyväskylä, August 2005

Janne Pakarinen

Abstract

The Ge-detector array JUROGAM has been constructed and combined with the gas-filled recoil separator RITU, novel focal-plane detection set-up GREAT and total data readout system (TDR) for recoil-decay tagging (RDT) measurements in the Accelerator Laboratory of the University of Jyväskylä. In one week of beam time, high quality $\gamma\gamma$-coincidence data were collected for the very neutron-deficient mid-shell nucleus ^{186}Pb. For the first time, non-yrast states in ^{186}Pb have been observed using in-beam γ-ray spectroscopic methods. Also, the recoil-decay tagging method was successfully employed for ^{186}Pb for the first time.

Competing structures in the light Pb isotopes have been under extensive investigation. Still, they remain a challenge for both theoretical and experimental studies. The present work reports on the extension of the yrast band and three new collective bands in ^{186}Pb associated with different intrinsic structures. The results have been compared to both the level-energy systematics of Pb nuclei and bands of different underlying structures in the neutron-deficient Pt and Hg nuclei. Based on the analysis of the decay pattern and comparison with interacting boson model calculations, a low-lying non-yrast band has been associated with oblate shape. Evidence for octupole and γ-vibrational bands has also been collected. These new results shed light on the triple-shape coexistence phenomenon and particle-hole excitations in neutron-deficient Pb nuclei. These structures intrude down to energies close to the spherical ground state when approaching the neutron mid-shell at N=104.

Contents

1 Introduction

The study of nuclear structure is an extremely complex task. This is best illustrated by the large variety of nuclear models in existence. Their validity is often based on fits to one and the same data set. Nevertheless, a few basic models have been able to explain a large amount of nuclear spectroscopic data. Noteworthy are the shell model [Goe49, Hax49, Hey90], the pairing model [Boh58] and the axially symmetric rotor model [Boh52], which all have survived, with slight modifications, through decades of spectroscopic investigations. However, improved spectroscopic techniques and methods have revealed various new interesting phenomena. The interplay between single-particle motion, collectivity and pairing in atomic nuclei is seen as a rich tapestry of coexisting nuclear shapes and exotic excitations. One of the goals of modern nuclear physics research is to understand the origin of these structures and their relation to the fundamental interactions between the nuclear constituents. It remains a challenge for both experimental and theoretical studies to obtain a consistent and detailed description of all the observed phenomena.

Nuclear structure studies of the proton drip line nuclei and the super-heavy elements took a giant leap when Ge-detector arrays were combined with the RITU gas-filled recoil separator [Lei95] for the Recoil-Decay Tagging (RDT) [Sim86, Pau95] experiments at JYFL. For the first time, proton drip line nuclei with production cross sections as low as 200 nb were probed using in-beam γ-ray spectroscopy [Gre04]. In the present work, a new Ge-detector array, JUROGAM, has been combined with the RITU separator, the GREAT focal-plane detector [Pag03] and the Total Data Readout (TDR) system [Laz03] for RDT experiments. This upgraded spectrometer has improved in the γ-ray detection efficiency, granularity, peak-to-total ratios and energy resolution when compared to previous Ge-detector arrays at JYFL. The new focal-plane detector GREAT together with the novel TDR data acquisition system enables exploration of nuclei with significantly longer lifetimes or alternatively via weaker reaction channels than the previous set-ups. These improvements have pushed the limits of the in-beam spectroscopy of exotic nuclei further. In the present work, this is demonstrated in in-beam γ-ray spectroscopy of ^{186}Pb.

In Pb isotopes close to the neutron mid-shell at N=104, experimental evidence for shape coexisting configurations and associated collective bands has been observed. These structures intrude down to energies close to the spherical ground state and can be associated with intruder $2p$-$2h$ and $4p$-$4h$ proton shell-model excitations across the Z=82 energy gap [Hey83, Woo92, Dup84, Dup90, Hey91, Jul01]. Calculations using

the deformed mean-field approach, essentially equivalent to the shell-model method, reveal three different shapes (spherical, oblate and prolate configurations).

In α-decay studies, the first two excited states of the mid-shell nucleus ^{186}Pb were observed to be 0^+ states [And00]. On the basis of α-decay hindrance factors the 0^+_2 state at 532 keV was associated with the oblate $2p$-$2h$ configuration and the 0^+_3 state at 650 keV with the prolate $4p$-$4h$ configuration. Consequently, together with the spherical ground state, the three 0^+ states form a unique shape-triplet in ^{186}Pb.

The 0^+_3 state is assumed to be the band head of a collective yrast band, which due to similarities with yrast bands in the Hg and Pt isotones has been assigned to a prolate shape [Hee93, Bax93, Rev03]. As pointed out by Andreyev *et al.* [And00], for a verification of the conclusions drawn from the α-decay studies, it is important to observe also the oblate band on top of the 532 keV 0^+_2 state.

In this thesis, an introduction to the experimental methods and instrumentation that have been used in the ^{186}Pb experiment is given in Chapter 2. As the author has had the privilege of being involved in the JUROGAM project from the beginning, deeper insight into the JUROGAM array is presented. Analysis of the ^{186}Pb experiment is described in Chapter 3 and the results discussed in Chapter 4.

The project has offered diverse responsibilities from the reconstruction of the measurement cave to the fine tuning of the Ge detectors. The author was the spokesperson for the ^{186}Pb experiment. The results of the experiment have been reported in the present work and in papers 1 and 2. The author was involved in the planning and implementation of the experiments reported in papers 3-16, in which the shape coexistence phenomenon in the light Pb region were studied.

1. **Evidence for an oblate structure in ^{186}Pb**
   J. Pakarinen, I.G. Darby, S. Eeckhaudt, T. Enqvist, T. Grahn, P.T. Greenlees, V. Hellemans, K. Heyde, F. Johnston-Theasby, P. Jones, R. Julin, S. Juutinen, H. Kettunen, M. Leino, A.-P. Leppänen, P. Nieminen, M. Nyman, R.D. Page, P.M. Raddon, P. Rahkila, C. Scholey, J. Uusitalo and R. Wadsworth,
   Phys. Rev. C **72**, R011304 (2005).

2. **Probing the three shapes in ^{186}Pb using in-beam γ-ray spectroscopy**
   J. Pakarinen, I.G. Darby, S. Eeckhaudt, T. Enqvist, T. Grahn, P.T. Greenlees, F. Johnston-Theasby, P. Jones, R. Julin, S. Juutinen, H. Kettunen, M. Leino, A.-P. Leppänen, P. Nieminen, M. Nyman, R.D. Page, P.M. Raddon, P. Rahkila, C. Scholey, J. Uusitalo and R. Wadsworth,
   Eur. Phys. J. A direct, (2005).

3. **RDDS Lifetime Measurement with JUROGAM + RITU**
   T. Grahn, A. Dewald, O. Möller, C.W. Beausang, S. Eeckhaudt, P. Greenlees, J. Jolie, P. Jones, R. Julin, S. Juutinen, H. Kettunen, T. Kröll, R. Krücken, M. Leino, A.-P. Leppänen, P. Maierbeck, D.A. Meyer, P. Nieminen, M. Nyman, J. Pakarinen, P. Petkov, P. Rahkila, B. Saha, C. Scholey, J. Uusitalo and R. Wadsworth,
   Eur. Phys. J. A direct, (2005).

4. **α decay and recoil decay tagging studies of ^{183}Tl**
   P.M. Raddon, D.G. Jenkins, C.D. O'Leary, A.J. Simons, R. Wadsworth, A.N. Andreyev, R.D. Page, M.P. Carpenter, F.G. Kondev, T. Enqvist, P.T. Greenlees, P.M. Jones, R. Julin, S. Juutinen, H. Kettunen, M. Leino, A.-P. Leppänen, P. Nieminen, J. Pakarinen, P. Rahkila, J. Uusitalo and D.T. Joss,
   Phys. Rev. C **70**, 064308 (2004).

5. **Recoil decay tagging of γ rays in the extremely neutron deficient nucleus ^{162}Os**
   D.T. Joss, K. Lagergren, D.E. Appelbe, C.J. Barton, J. Simpson, B. Cederwall, B. Hadinia, R. Wyss, S. Eeckhaudt, T. Grahn, P.T. Greenlees, P.M. Jones, R. Julin, S. Juutinen, H. Kettunen, M. Leino, A.-P. Leppänen, P. Nieminen, J. Pakarinen, P. Rahkila, C. Scholey, J. Uusitalo, R.D. Page, E.S. Paul and D.R. Wiseman,
   Phys. Rev. C **70**, 017302 (2004).

6. **Decay studies of ^{170,171}Au, ^{171,173}Hg and ^{176}Tl**
   H. Kettunen, T. Enqvist, T. Grahn, P.T. Greenlees, P. Jones, R. Julin, S. Juutinen, A. Keenan, P. Kuusiniemi, M. Leino, A.-P. Leppänen, P. Nieminen, J. Pakarinen, P. Rahkila and J. Uusitalo,
   Phys. Rev. C **69**, 054323 (2004).

7. **Shape isomerism and spectroscopy of ^{177}Hg**
   A. Melarangi, D.E. Appelbe, R.D. Page, H.J. Boardman, P.T. Greenlees, P. Jones, D.T. Joss, R. Julin, S. Juutinen, H. Kettunen, P. Kuusiniemi, M. Leino, M. Muikku, P. Nieminen, J. Pakarinen, P. Rahkila, J. Simpson and J. Uusitalo,
   Phys. Rev. C **68**, R041301 (2003).

8. **Prolate deformation in the ^{187,189}Bi isotopes**
   A. Hürstel, Y. Le Coz, E. Bouchez, A. Chatillon, A. Görgen, P.T. Greenlees, K. Hauschild, S. Juutinen, H. Kettunen, W. Korten, P. Nieminen, M. Rejmund, Ch. Theisen, J. Wilson, A.N. Andreyev, F. Becker, T. Enqvist, P.M. Jones, R. Julin, H. Kankaanpää, A. Keenan, P. Kuusiniemi, M. Leino, A.-P. Leppänen, M. Muikku, J. Pakarinen, P. Rahkila and J. Uusitalo,
   Eur. Phys. J. A **21**, 365-368 (2004).

9. **In-beam spectroscopy at the RITU gas-filled recoil separator**
P.T. Greenlees, A.N. Andreyev, J. Bastin, F. Becker, E. Bouchez, P.A. Butler, J.F.C. Cocks, Y. Le Coz, K. Eskola, J. Gerl, K. Hauschild, K. Helariutta, R.-D. Herzberg, F.-P. Heßberger, R.D. Humphreys, A. Hürstel, D.G. Jenkins, G.D. Jones, P. Jones, R. Julin, S. Juutinen, A. Keenan, H. Kankaanpää, H. Kettunen, T.-L. Khoo, W. Korten, P. Kuusiniemi, M. Leino, A.-P. Leppänen, M. Muikku, P. Nieminen, R.D. Page, T. Page, J. Pakarinen, P. Rahkila, P. Reiter, Ch. Schlegel, C. Scholey, Ch. Theisen, J. Uusitalo, K. Van de Vel, R. Wadsworth and H.-J. Wollersheim,
Eur. Phys. J. A **20**, 87 (2004).

10. **Alpha-decay studies of the new isotopes ^{191}At and ^{193}At**
H. Kettunen, T. Enqvist, T. Grahn, P.T. Greenlees, P. Jones, R. Julin, S. Juutinen, A. Keenan, P. Kuusiniemi, M. Leino, A.-P. Leppänen, P. Nieminen, J. Pakarinen, P. Rahkila and J. Uusitalo,
Eur. Phys. J. A **17**, 537 (2003).

11. **Spectroscopy of the neutron-deficient nuclide ^{171}Pt**
T. Bäck, B. Cederwall, K. Lagergren, R. Wyss, A. Johnson, P.T. Greenlees, D. Jenkins, P. Jones, D.T. Joss, R. Julin, S. Juutinen, A. Keenan, H. Kettunen, P. Kuusiniemi, M. Leino, A.-P. Leppänen, M. Muikku, P. Nieminen, J. Pakarinen, P. Rahkila and J. Uusitalo,
Eur. Phys. J. A **17**, 1 (2003).

12. **First observation of gamma-rays from the proton emitter ^{171}Au**
T. Bäck, B. Cederwall, K. Lagergren, R. Wyss, A. Johnson, D. Karlgren, P.T. Greenlees, D. Jenkins, P. Jones, D.T. Joss, R. Julin, S. Juutinen, A. Keenan, H. Kettunen, P. Kuusiniemi, M. Leino, A.-P. Leppänen, M. Muikku, P. Nieminen, J. Pakarinen, P. Rahkila and J. Uusitalo,
Eur. Phys. J. A **16**, 489 (2003).

13. **First observation of excited states in the very neutron deficient nucleus ^{165}Os and the yrast structure of ^{166}Os**
D.E. Appelbe, J. Simpson, M. Muikku, H.J. Boardman, A. Melarangi, R.D. Page, P.T. Greenlees, P. Jones, R. Julin, S. Juutinen, A. Keenan, H. Kettunen, P. Kuusiniemi, M. Leino, P. Nieminen, J. Pakarinen, P. Rahkila, J. Uusitalo and D.T. Joss,
Phys. Rev. C **66**, 014309 (2002).

14. **Confirmation of triple shape coexistence in ^{179}Hg: Focal plane spectroscopy of the alpha decay of ^{183}Pb**
D.G. Jenkins, A.N. Andreyev, R.D. Page, M.P. Carpenter, R.V.F. Janssens, C.J. Lister, F.G. Kondev, T. Enqvist, P.T. Greenlees, P.M. Jones, R. Julin, S. Juutinen, H. Kettunen, P. Kuusiniemi, M. Leino, A.-P. Leppänen, P. Nieminen, J. Pakarinen, P. Rahkila, J. Uusitalo, C.D. O'Leary, P. Raddon, A. Simons, R. Wadsworth and D.T. Joss,
Phys. Rev. C **66**, 011301 (2002).

15. **Isomeric states in proton-unbound ^{187,189}Bi isotopes**
A. Hürstel, M. Rejmund, E. Bouchez, P.T. Greenlees, K. Hauschild, S. Juutinen, W. Korten, Y. Le Coz, P. Nieminen, Ch. Theisen, A.N. Andreyev, F. Becker, T. Enqvist, P.M. Jones, R. Julin, H. Kankaanpää, A. Keenan, P. Kuusiniemi, M. Leino, A.-P. Leppänen, M. Muikku, J. Pakarinen, P. Rahkila and J. Uusitalo,
Eur. Phys. J. A **15**, 329 (2002).

16. **In-beam studies of very neutron-deficient heavy nuclei**
R. Julin, P.T. Greenlees, K. Helariutta, P. Jones, S. Juutinen, A.-P. Leppänen, H. Kankaanpää, A. Keenan, H. Kettunen, P. Kuusiniemi, M. Leino, M. Muikku, P. Nieminen, J. Pakarinen, P. Rahkila, J. Uusitalo, D.T. Joss, S.J. Williams, D.G. Jenkins, N.-S. Kelsall, R. Wadsworth, K. Hauschild, A. Hürstel, W. Korten, Y. Le Coz, A.N. Andreyev, P. Van Duppen, M. Huyse, K. Van de Vel, C.J. Moore, C.D. O'Leary, R.D. Page, M.J. Taylor, W. Reviol and M.B. Smith,
Eur. Phys. J. A **15**, 189 (2002).

2 Experimental aspects

In this chapter, the production of neutron-deficient Z=82 nuclei and instrumentation used in in-beam γ-ray spectroscopy employing the Recoil-Decay Tagging (RDT) method are discussed. More weight is given to the description of the JUROGAM array due to the author's significant contribution in its construction.

2.1 Production of very neutron-deficient Pb nuclei

In the present work, neutron-deficient Pb nuclei were produced via fusion-evaporation reaction by bombarding a stationary target with heavy ions. The process can be expressed as

$$(A_p, Z_p) + (A_t, Z_t) \xrightarrow[\text{formation}]{} (A_c, Z_c) \xrightarrow[\text{decay}]{} (A_{er}, Z_{er}) + EP + \gamma \text{ rays}, \tag{2.1}$$

where A and Z are the mass and proton number of the nucleus indicated by the subscript, where p, t, c and er denotes the projectile, target, compound nucleus and the evaporation residue, respectively. EP stands for evaporated particles. Consequently, the reaction can be treated as a two-step process, the formation and the decay of the compound nucleus.

Reaction kinematics and time scale

A nuclear reaction can occur, if the projectile can penetrate through or if the bombarding energy exceeds the Coulomb barrier (cf. Bass interaction barrier). This can be written as

$$B_{Coul} = \frac{e^2}{4\pi\epsilon_0} \frac{Z_p Z_t}{r_p + r_t}, \tag{2.2}$$

where $Z_{p(t)}$ is the projectile (target) proton number and $r_{p(t)}$ is the radius of the projectile (target) nucleus. At a center of mass energy (E_{cm}) close to the Coulomb

barrier (B_{Coul}), the colliding nuclei can be brought within the range of nuclear forces giving rise to quasi-elastic surface reactions. At this distance, the resultant of the Coulomb and nuclear forces is still repulsive for heavy nuclei and additional energy is required to get the fragments over their mutual potential barrier [Bas74]. The threshold energy (cf. Bass fusion barrier) for a fusion reaction can be calculated by using the masses of interacting atoms as follows

$$E_{cm}^{threshold} = -Q = -931.49 \times (m_p + m_t - m_c) MeV, \quad (2.3)$$

$$E_{lab}^{threshold} = -Q \frac{m_t}{m_t + m_p}, \quad (2.4)$$

where m_p, m_t and m_c are the atomic masses of the projectile, target and compound nuclei in atomic mass units, respectively. At beam energies higher than $E_{lab}^{threshold}$, the projectile and the target nuclei can be brought together and the so-called contact point can be reached. If then the density distributions of these nuclei start to penetrate each other the kinetic energy of nucleons will be dissipated in collisions between the nucleons originating from different nuclei. The energy dissipation can be imagined as a result of a frictional force. Qualitatively, this force slows down the radial motion and transforms the relative angular momentum into intrinsic angular momentum of the compound nucleus [Bas74]. The extra energy brought into the system is stored as excitation energy of the compound nucleus. Using the former notation, the excitation energy can be expressed as

$$E^* = Q + E_{cm} = Q + \frac{m_t}{m_t + m_p} E_{beam}, \quad (2.5)$$

where E_{beam} is the beam energy. It should be noted, that a heavy-ion induced fusion-evaporation reaction (A_1+A_2>100) is an endothermic process (Q<0) and more energy must be supplied to overcome the Coulomb repulsion than is gained from nuclear binding energies [Bas74]. In lighter systems with higher$Q$-values, the threshold energy is lower (Equation 2.3) than the Coulomb-barrier energy. In those cases, fusion can occur if the bombarding energy overcomes the Coulomb barrier. Thus, it can be easily established that the production of a cold compound nucleus is impossible.

If the compound nucleus is stable against fission, the excitation energy is released via particle and γ-ray emissions as the nucleus cools down. Due to the reaction kinematics, the fusion-evaporation residues fly in a narrow forward cone with respect to the beam axis. This kinematic focusing is utilized in the RDT measurements described in Section 2.2. In such measurements, the projectile velocity is of the order of 10%

of the speed of light. It then follows, that the transit time of the incident projectile across the target nucleus is approximately 10^{-22} s. The first particles are evaporated $10^{-20} - 10^{-16}$ s after the impact [Bas80]. As the interaction time in collisions between the heavy nuclei is significantly larger than the time needed for nucleus rearrangement, it can be concluded that the energy is shared between the nucleons in the compound nucleus and the system has no memory of entrance channel. The fusion-evaporation process with a typical time scale is illustrated in Figure 2.1. Competition between different evaporation channels will be discussed later.

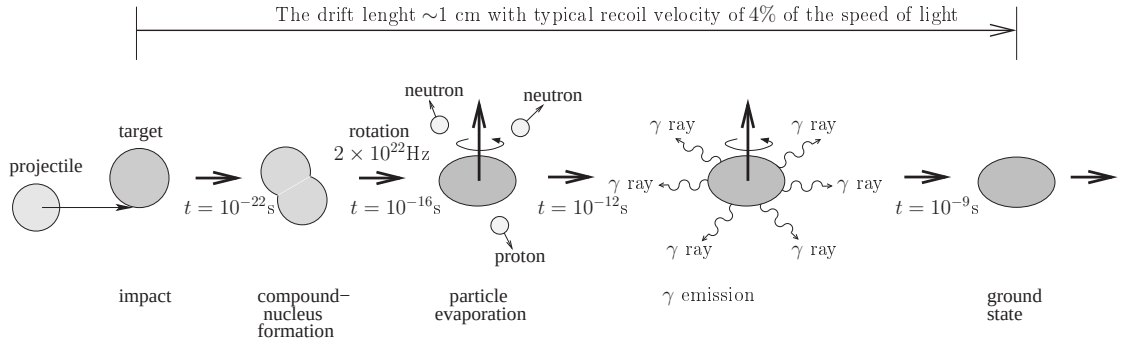

Figure 2.1: Different steps of a typical fusion-evaporation reaction ending up to the ground state. The average time scale of each step in case of heavy compound-nucleus formation is indicated [Bas80].

The reaction kinematics described above is a classical simplification and more detailed analysis based on a two-body potential derived from the liquid drop model is discussed in Reference [Bas74]. However, the given description is both illustrative and good approximation of the heavy-ion induced fusion-evaporation reaction.

Production cross section

The fusion cross section defines the formation probability of the compound nucleus, which can decay via several fusion-evaporation channels or by fission. Therefore,

$$\sigma_{fusion} = \sum \sigma_{ER} + \sigma_{fission}, \tag{2.6}$$

where σ_{ER} is the cross section of an individual evaporation residue and$\sigma_{fission}$ denotes fission cross section.

In the present work, excited states in ^{186}Pb were populated using the ^{106}Pd(^{83}Kr, 3n)^{186}Pb reaction at a beam energy of 355 MeV (E_{cm}=199 MeV). Calculated cross sections of various evaporation channels for this projectile–target combination as a function of excitation energy are visualized in Figure 2.2. In order to illustrate the

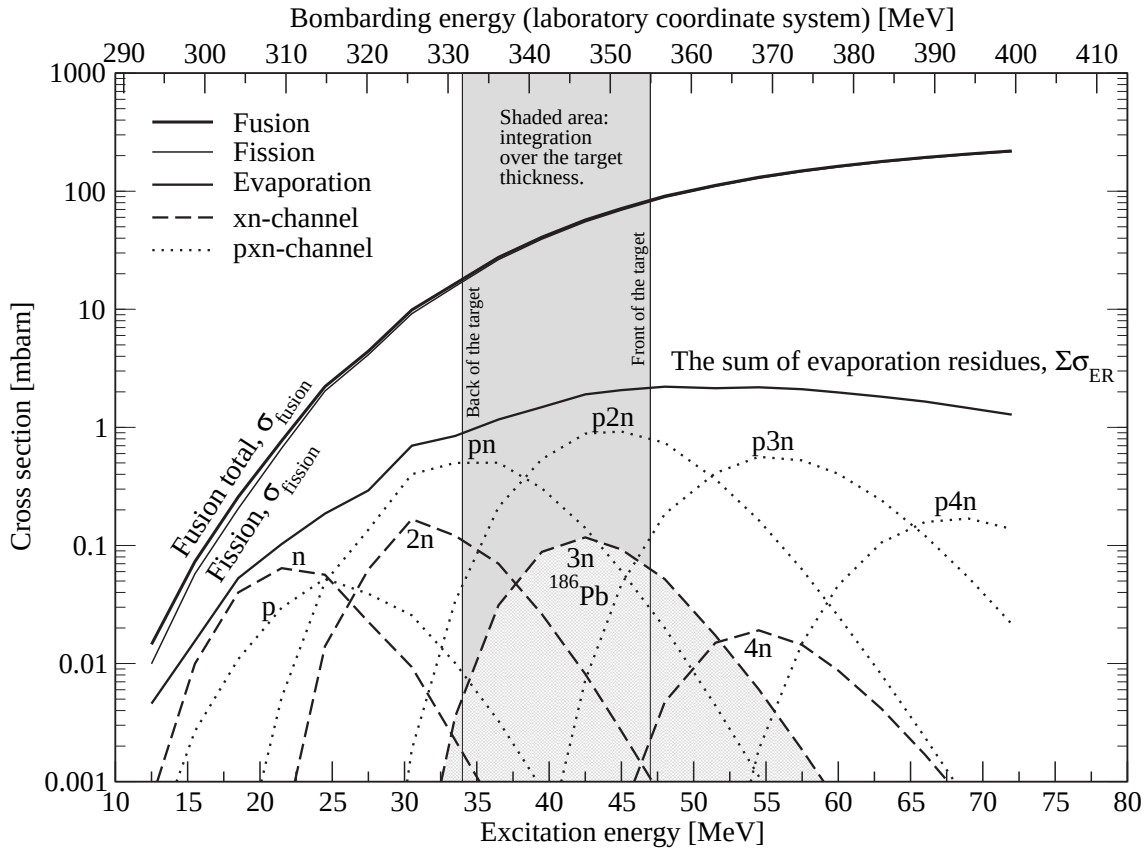

Figure 2.2: HIVAP calculation for the reaction ^{83}Kr+^{106}Pd$\rightarrow^{189}$Pb* [And04]. Cross sections for xn and pxn evaporation channels together with the total fusion, fission and the sum of evaporation residue cross sections are shown. The shaded area visualizes the projectile energy range over the target in the present work.

magnitudes of the competing decay channels, also the total fusion, fission and the sum of the fusion-evaporation cross sections are shown. It can be clearly seen, that the dominant compound-nucleus decay mode in the present case is fission, over 96% of the total fusion cross section. Due to the energy loss in the target it is better to use a higher beam energy than the calculated optimum due to the drastic drop in the cross section below the optimum excitation energy.

Measured cross sections for the light Pb nuclei range from 200 nb for ^{182}Pb to 1.1 mb for ^{188}Pb depending on the chosen reaction. In practice, this means that with an incident particle rate of 37.5 GHz (6 pnA) the production rate of evaporation residues with a cross section of 200 μb for a A=106 target of thickness 1 mg/cm^2 is only 40 Hz.

Experimentally, the production cross section of a fusion-evaporation residue can be determined from

$$\sigma_{ER} = \frac{R_{ER}}{I_p N}, \tag{2.7}$$

where I_p is the flux of incident particles, R_{ER} the rate of evaporation residues and N the number of target nuclei per unit area. In the present work, the cross section was measured to be 185 μb by assuming 30% RITU transmission efficiency, 55% α-detection efficiency, 80% recoil image coverage, and using the knownα branch of 40% for ^{186}Pb [And99a]. The average beam current was 6 pnA and the target thickness was 1 mg/cm^2 and the average ^{186}Pb α rate was 2.3 Hz.

Compound-nucleus model

A specific compound nucleus can be formed through several reaction processes. Experimentally, one can affect the compound-nucleus formation probability only by choosing the projectile–target combination (entrance channel) and the bombarding energy. In practice, not all elements can be utilized as a projectile or target material due to their chemical properties. In addition, the use of certain projectile or target material may be restricted by radiation safety rules (like at JYFL) or by the price of an isotope of small natural abundance. The lack of available projectile–target combination lays more emphasis on the importance of the choice of the bombarding energy. The dominant evaporation channel depends on the excitation energy, which again is proportional to the bombarding energy. In practice, the excitation function is often measured to get the best yield for reaction products.

Compound-nucleus fission can occur at any step of the compound-nucleus formation and the decay process. The competition between fission, light-particle evaporation and γ-ray emission continues from the compound-nucleus formation down to the ground state of evaporation residue [Bas80]. Consequently, this competition has to be taken into account in cross-section estimates.

The decay pattern of a compound nucleus at a given excitation energy depends in general on the angular momentum distribution and hence on the entrance channel; the angular momentum of the compound nucleus increases with increasing projectile mass. Excitation energy and angular momentum are removed from the compound nucleus stepwise. During each step, different decay possibilities are considered. The present ^{186}Pb case, as illustrated in Figure 2.3, is a good example of the typical decay pattern of a compound nucleus. Three evaporated neutrons carry away approximately 27.4 MeV (separation energy) plus 9 MeV (kinetic energy) of excitation energy and only a few units of angular momentum. Most of the angular momentum is removed via γ-ray emission. The so-called statistical γ-ray transitions (typically E1) take place approximately 10^{-15} s after impact and are followed by a cascade of γ-ray transitions

approximately 10^{-12} s after impact (typically E2 transition for quadrupole deformed nuclei). The γ-ray emission competes with particle evaporation and is the dominant decay mode at excitation energies below the neutron-separation energy and in the vicinity of the yrast line. In this sense, fusion-evaporation reactions favour the study of collective behaviour of nucleons in proton-rich nuclei by employing in-beamγ-ray spectroscopy. They provide a unique possibility to study nuclear properties under conditions unattainable via other types of reactions.

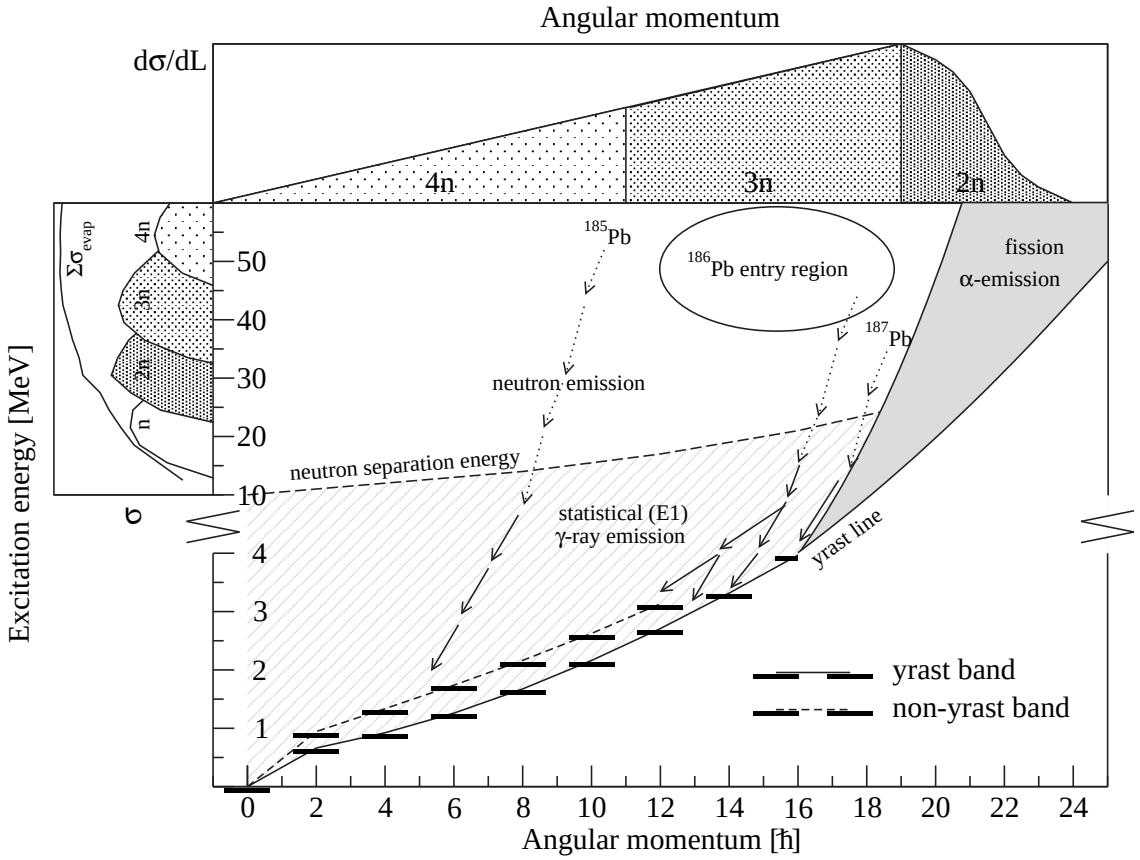

Figure 2.3: Decay pattern of compound nuclei ^{189}Pb as a function of angular momentum. The yrast and non-yrast states are plotted quantitatively, whereas particle emission is described qualitatively. Differential cross section is shown schematically above to describe the possible exit channels. Cross sections for different neutron-evaporation channels are shown as a function of excitation energy on the left.

In the compound-nucleus model of nuclear reactions, it is essential to note, that a specific set of final decay products is independent of the incident nuclei in the compound-nucleus formation process. The decay probability depends only on the total energy given to the system, not on the nature of the initial nuclei, whereas the angular momentum limit in a certain compound nucleus at a given excitation energy is dependent on the entrance channel [Kra88, Bas80]. This has to be considered especially in the

production of super-heavy elements, where an asymmetric reaction can have an order of magnitude higher cross section than a symmetric reaction [Sea90].

2.2 The RDT method

To probe a nucleus produced in a fusion-evaporation reaction using in-beam γ-ray spectroscopy, an appropriate method to distinguish between the γ ray of interest and the γ-ray background is required. The overwhelming background is created, for example, by the reaction (fission, fusion and transfer) products, compound-nucleus decay and Coulomb de-excitation. At the target area, the evaporation residues can only be 'identified' in-directly by observing the evaporated particles. Such measurements require an efficient 4π particle-detector array of high granularity. This method enables the γ-ray background to be reduced by gating on the evaporated particles, but it does not provide selection of a pure exit channel. Obviously, such an array has only limited capacity to probe multi-neutron exit channels. In practice, an efficient neutron-detector array around the target would also reduce the γ-ray detection efficiency and be blocked by γ-ray flux originating from various reaction processes.

Direct observation of the fusion-evaporation residues requires a special technique. Due to reaction kinematics, the evaporation residues fly into a small forward cone away from the hostile environment at the target area. Thus, they can be observed off the beam axis or separated in flight. When in-flight separated, the evaporation residues are observed in the focal-plane implantation detector. Then the identification is made by using the information of the time-of-flight and the kinetic energy of the evaporation residues. The coincidence relation between the transported evaporation residues and the prompt γ rays enables the γ-ray spectroscopic study of the evaporation residues (recoils from now on) produced via very weak reaction channels. The selectivity of this so-called recoil-gating method is determined by the mass resolving power of the separator.

In heavy-element studies, when usually only one fusion-evaporation channel is open, the mass resolving power of an in-flight separator (RITU in this context) is usually sufficient to separate recoils from the primary beam. In the light Pb region, where several fusion-evaporation channels are open, the resolving power is inadequate to separate recoils with a similar mass/charge ratio. Therefore, the γ-ray energy spectra obtained in such experiments contain γ rays from various nuclei produced via different fusion-evaporation channels. However, the recoil-gating method can be applied, for example, in in-beam γ-ray spectroscopy of ^{186}Pb as established by Baxter *et al.* [Bax93].

The Recoil-Decay Tagging (RDT) method is an extension of the recoil-gating method.

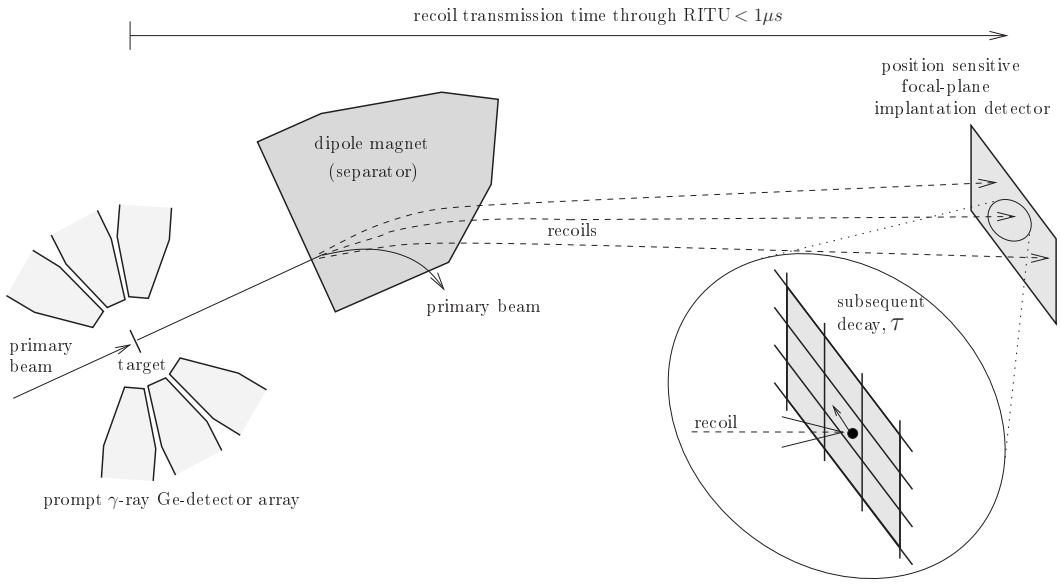

Figure 2.4: Schematic figure illustrating the RDT method. Prompt γ rays are correlated with recoils, which are separated before being implanted into the focal-plane detector. Implanted recoils can be tagged by their subsequent decay within the same detector pixel.

The idea of taking advantage of the characteristic decay of recoils led to an outstanding improvement in selectivity. In the RDT method, the subsequent decay (α, electron, proton, fission) of the implanted recoil is observed in the same position as the recoil within a certain time window. Thus, the implanted recoil can be 'tagged' with the unique signature from the subsequent decay (extra detectors at the focal plane can be used for tagging with the β particles or γ rays). As the recoils are identified using their decay properties, the prompt γ rays can be correlated with the recoils in the same way as in the recoil-gating method. Therefore, the capability of the separator to distinguish between the beam and recoils is often adequate for an RDT measurement.

The RDT method is visualized in Figure 2.4. The principle of the RDT dates back to mid eighties, when Simon *et al.* [Sim86] carried out the first in-beam experiment with recoil separator SHIP at GSI in which the prompt γ rays detected by a NaI(Tl)-detector array were tagged with the α decay of the respective nucleus. Later on, the method was named by Paul *et al.* [Pau95]. They demonstrated the power of the method in the first RDT measurement by combining the EUROGAM Ge-detector array with the RMS recoil separator at Daresbury Laboratory in the UK.

In the present work, the RDT method was employed using the instrumentation shown in Figure 2.5. The Recoil Ion Transportation Unit (RITU) [Lei95] was used to separate recoils from the primary beam particles and to transport them to the focal-plane detection system GREAT [Pag03]. At the focal plane, the energy deposited in the Si detector, the recoil time-of-flight and decay energy were used to distinguish between

the nucleus of interest and other recoils. The RITU and GREAT apparatus will be discussed in Sections 2.4 and 2.5, respectively. The emitted γ rays were observed with the JUROGAM array, which is discussed in the following section. A more detailed description of the data analysis methods is given in Chapter 3.

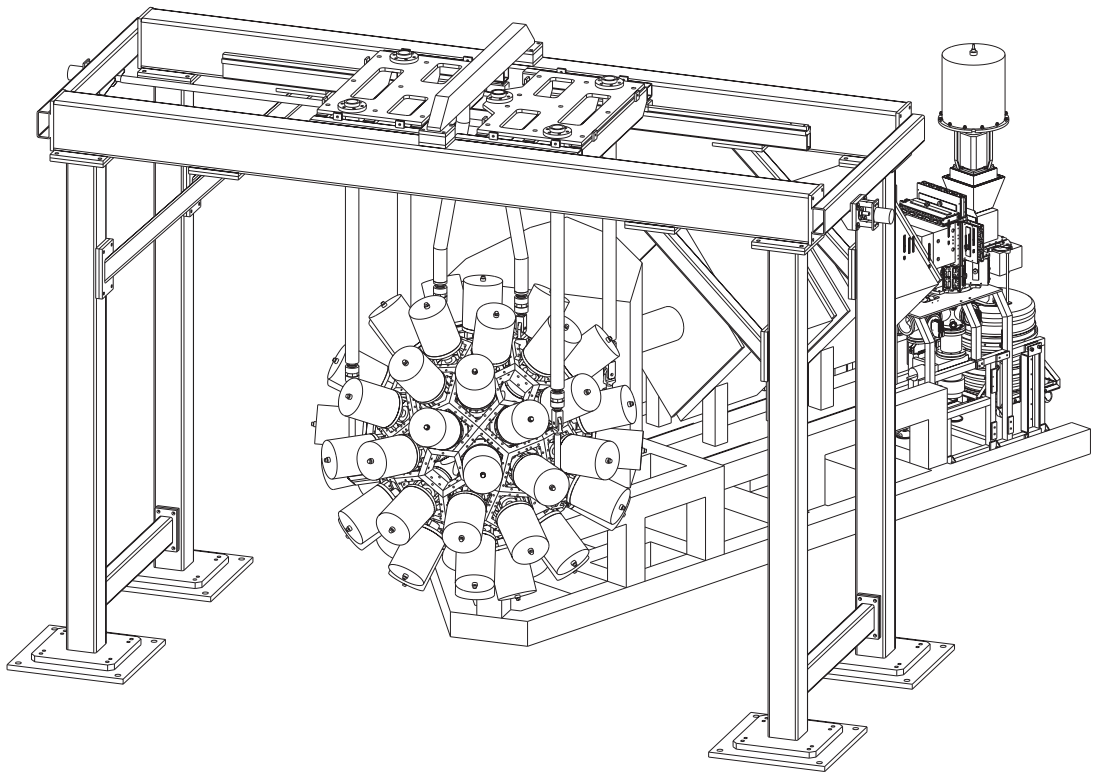

Figure 2.5: Schematic drawing of the instrumentation used in the present work. The JUROGAM array stands in the front of the RITU separator. The GREAT focal-plane detection set-up is shown behind RITU.

2.3 The JUROGAM Ge-detector array

The JUROGAM Ge-detector array has been constructed and combined with the RITU gas-filled separator, the GREAT focal-plane detector and the TDR data acquisition system. Properties of the JUROGAM array are discussed in this section, following a review of in-beam γ-ray detection.

2.3.1 In-beam γ-ray detection

Gamma-ray spectrometers have gone through several stages of development to attain the resolving power of a modern Ge-detector array. When using in-beam γ-ray spectroscopy as a tool to probe nuclear structure, the spectrometer must be capable of measuring γ rays in a wide energy range with high efficiency and good spectral response. This requires a simultaneous optimatization of several properties. These requirements are briefly described below.

Peak-to-total ratio

A significant part of the spectral background arises from Compton scattered γ rays escaping the Ge detector. This is described by the peak-to-total (PT) ratio, which is defined as the ratio of photopeak events to the total number of counts in the measured spectrum. Even for a large single crystal Ge detector, this ratio is not more than 0.2 ie. 80% of the total counts in the γ-ray spectrum fall into the background. The PT ratio can be improved by suppressing the scattered events in the final spectrum. This is achieved by surrounding the Ge crystal with an efficient veto detector (a Compton-suppression shield). The firing of the veto detector in coincidence with the inner Ge detector rejects the γ-ray event. Inorganic scintillator detectors are optimum for this purpose as they are fast and efficient (good energy resolution is not needed). Especially, bismuth germanate (BGO) of high density and high γ-ray absorption efficiency (high Z value) as a scintillator material enables the construction of a compact shielding geometry.

The use of suppression is emphasized in coincidence measurements. If the PT ratio can be improved from 0.2 to 0.6 (300%) for γ-ray singles, the improvement for 3-fold coincidences rises from 0.008 to 0.216 (2700%). A high PT ratio is essential in the measurement of low statistics, when the observed events must be in the photopeak instead of the background.

The Doppler effect

The Doppler effect occurs whenever the source of waves is moving with respect to the observer. In in-beam measurements, the source is the recoiling nucleus which emits electromagnetic radiation (γ rays) whereas the Ge detector plays the role of the observer. The γ-ray energy shifts as the wavelength changes. The observed change in the γ-ray energy (E_γ) is proportional to the recoil velocity (v):

$$E_\gamma = E_0 \left(1 + \frac{v}{c} cos\theta\right), \tag{2.8}$$

where E_0 is the initial γ-ray energy, c is the speed of light and θ is the detector angle with respect to the velocity vector of the recoil. The Doppler-shift problem can be overcome by determining the recoil velocity. In the present experiment, a recoil velocity of 3.73% of the speed of light was deduced by using the knownγ-ray energies and detector angles with respect to the beam axis. The Doppler shift ofγ rays emitted by recoils drifting at this velocity is shown in Figure 2.6. However, the Doppler effect can worsen the energy resolution of a detector. Doppler broadening (ΔE_γ) arises from the opening angle of a single detector and can be expressed as

$$\Delta E_\gamma = E_0 \frac{v}{c} sin\theta \cdot \Delta\theta, \tag{2.9}$$

where $\Delta\theta$ is the opening angle of the detector. The effect of the Doppler broadening decreases with decreasing opening angle of the detector module ie. with increasing granularity of the detector array. It should be noted, that the Doppler broadening is related not only to the opening angle and the recoil velocity, but is also proportional to the emitted γ-ray energy.

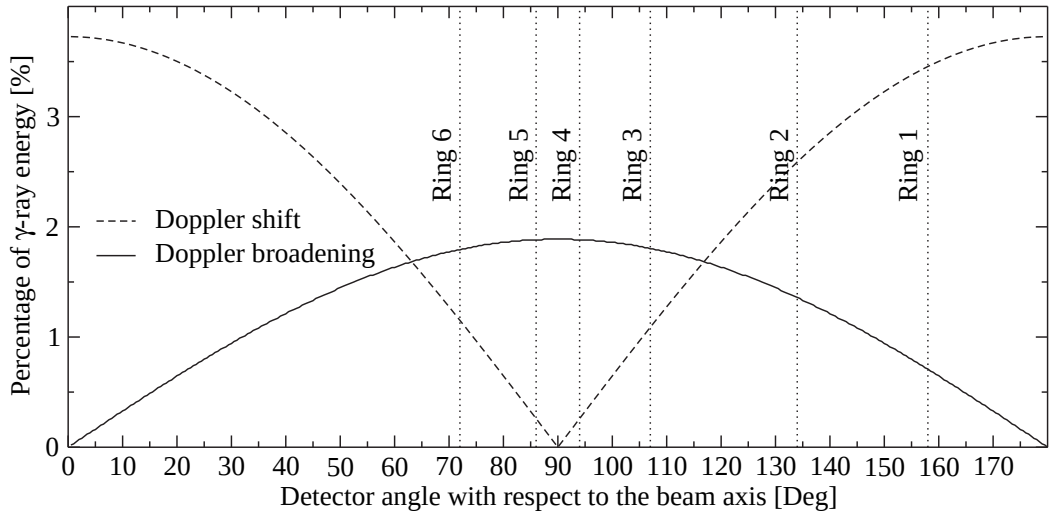

Figure 2.6: The maximum Doppler broadening and the Doppler shift ofγ rays in the JUROGAM Ge detectors at a recoil velocity of 3.7% of the speed of light. The values are expressed as a percentage of the γ-ray energy as a function of detector angle with respect to the beam axis. For angles greater than 90° the Doppler shift is negative. The angles of the detector rings (see Section 2.3.4) have been marked.

The Doppler shift and Doppler broadening of theγ rays in the JUROGAM Ge detectors for the recoil velocity in the present study is illustrated in Figure 2.6. The Doppler

broadening is larger for the detectors close to 90° with respect to the beam axis and for high-energy γ rays. In the calculation, the maximum angular acceptance of $\pm 4.6°$ of the RITU separator and the opening angle of $\pm 9.9°$ of a single JUROGAM Ge detector are taken into account.

Detection efficiency

The total photopeak efficiency of a Ge-detector array is determined by the total solid angle covered by the Ge detectors and by their individual photopeak efficiencies. The total solid angle can be increased by bringing the detectors closer to the target. The disadvantages are then Doppler broadening and coincidence summing. The importance of the detection efficiency is emphasized in coincidence measurements as the γ^n-coincidence efficiency is proportional to the n^{th} power of the efficiency (as is PT ratio). The absolute photopeak efficiency of the JUROGAM array is shown in Figure 2.7 for the energy range used in the present measurement. The efficiency of each detector ring is also plotted. Deviations in the efficiencies for different detector rings arise from the different number of detectors in each ring and from the deviations in individual detector efficiencies.

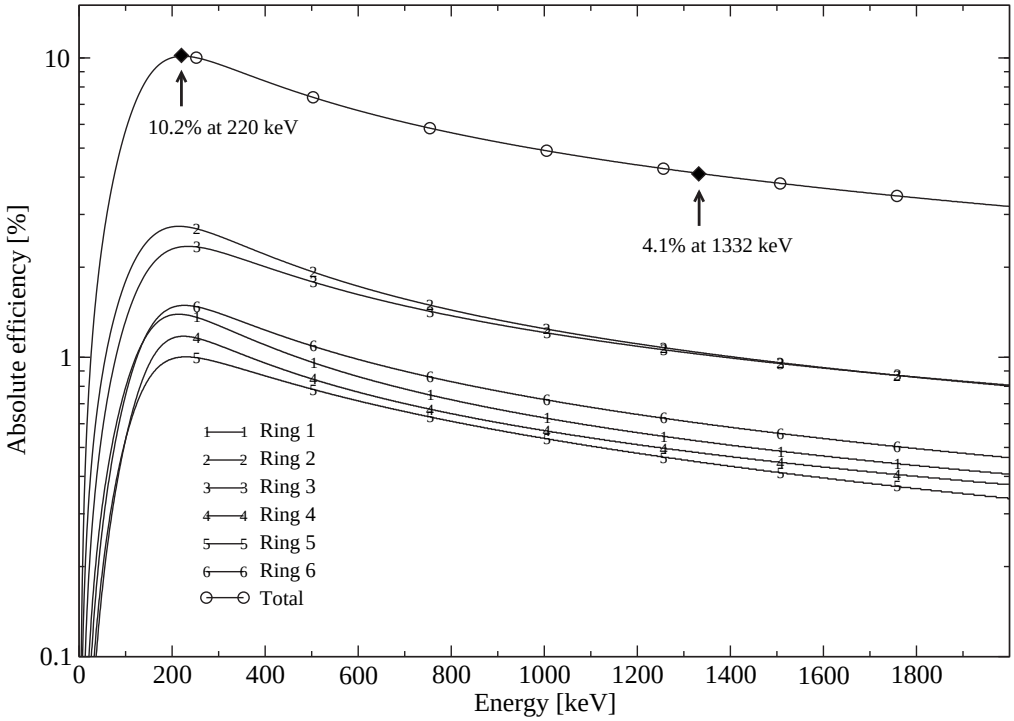

Figure 2.7: Total and detector ring efficiencies of the JUROGAM array as a function of γ-ray energy. The values of maximum efficiency and efficiency at 1332 keV (γ rays emitted by a ^{60}Co source) are shown by solid diamonds.

Granularity and coincidence summing

Coincidence summing arises from multiple γ rays hitting the same Ge detector. The probability of multiple hits decreases with increasing granularity and, naturally, increases with the γ-ray multiplicity. In the γ-ray energy spectrum, these events fall into the background or to sum peaks.

The number of n-fold coincidences (N_n) is proportional to the γ-ray multiplicity (M_γ) and to the photopeak efficiency of the detectors (ϵ_p). In the case of identical detectors, this can be expressed as [Jul02]

$$N_n \propto \binom{N_{Ge}}{n} \epsilon_p^n M_\gamma \propto \binom{N_{Ge}}{n} \frac{1}{d^{2n}}, \tag{2.10}$$

where N_{Ge} is the number of detectors and d is detector to target distance. The formula can be used to compare arrays with different numbers of detector modules at different distances. For example, an array of 6 detectors at 20 cm from the target has comparable coincidence efficiency with an array of 12 similar detectors at a distance of 29 cm from the target for 2-fold coincidences. It is obvious that two detectors mounted face to face cover a solid angle close to 4π and give high efficiency, but provide poor granularity.

The beam current is often limited by the Ge detector counting rates. Higher beam currents can be employed by increasing the detector granularity. In the present experiment, the average beam current was limited to 6 pnA due to the maximum operational counting rate of 10 kHz of a single Ge detector. With higher counting rates, the preamplifier signals start to pile-up giving rise to a poor energy resolution.

Gamma-ray resolving power

In high-spin studies, the concept of γ-ray resolving power has been used to describe the selectivity of the Ge-detector array in in-beam γ-ray detection. The resolving power is defined for rotational bands with an average γ-ray energy separation (SE_γ). For an n-fold coincidence event this can be quantified as [Nol90]

$$R_{\gamma n} = \left(\frac{SE_\gamma}{\Delta E_\gamma} PT \right)^n, \tag{2.11}$$

where ΔE_γ is the energy resolution and PT the peak-to-total ratio. It can be immediately seen, that high peak-to-total ratio and energy resolution improves the resolving

power. It should be noted, that the resolution includes the Doppler broadening. Consequently, the array geometry (granularity) is put into this term and in practice, it is the only adjustable parameter with the available detection technology. It is also remarkable, that efficiency is not taken into account in Equation 2.11.

In RDT measurements, the γ-ray resolving power does not play such a crucial role as it does in high-spin measurements. That is since a) the RDT method enables an efficient selection of the reaction channel and b) the γ-ray multiplicity of nuclei produced in heavy-ion induced fusion-evaporation reaction close to the proton drip line is relatively low. In RDT measurements, the statistics is often only sufficient for γ-ray singles or $\gamma\gamma$-coincidence analysis due to the low production cross section. In low-fold coincidence measurements, the γ-ray resolving power between different arrays varies little (n^{th} power). Thus, the γ-ray resolving power does not describe the capability of the array in such measurements. Instead, the PT ratio and the total efficiency should be maximized.

2.3.2 History

Gamma-ray spectrometers have been important tools in nuclear structure research. The first attempts to measure the evolution of nuclear structure as a function of angular momentum and excitation energy by employing in-beam γ-ray spectroscopy were made using set-ups consisting only of a few NaI(Tl) scintillation detectors. These experiments suffered from the poor energy resolution and the small number and size of the scintillation detectors. Despite this, the low-spin rotational structures for example in even-even $^{156-162}$Dy nuclei were observed by Morinaga *et al.* [Mor63].

The development of reverse-biased Ge detectors in the mid-1960's heralded the next generation of γ-ray detection set-ups. The first experiments taking the advantage of these high resolution detectors were carried out in the early 1970's. Using only two Li drifted Ge detectors, Johnson *et al.* discovered backbending in ^{160}Dy at spin 16^+ [Joh71].

The study of nuclear properties took a giant step in the 1980's, when Ge-detector arrays (e.g. the TESSA arrays [Twi83]) were equipped with Compton-suppression shields. The quality of the γ-ray spectra improved significantly as the peak-to-total ratio improved by a factor of three due to Compton suppression. This was a remarkable development especially for high-spin studies, where the γ-ray multiplicity is high. The first shielding material was NaI(Tl), but not until the invention of high density BGO material, was the construction of compact array geometries possible [Nol85]. This revolutionary development led to an improved understanding of both the characteristic of the individual excitations and the collective behaviour in nuclei. One of the highlights was the observation of superdeformation in ^{152}Dy [Twi86].

After the breakthrough in γ-ray detection, a joint European Collaboration started operation in the end of 1980's. It launched the EUROBALL campaign [Bec92a, Sim97] dedicated to high-spin physics. In the first stage of the campaign, the GASP [Ros93] and EUROGAM I [Nol90] arrays were constructed. The EUROGAM I array was set up in Daresbury Laboratory, UK, whereas the GASP array was situated in the Laboratori Nazionale di Legnaro, Italy. After a short period at Daresbury, the Phase I detectors of EUROGAM I were moved to Centre de Recherches Nucleaire, Strasbourg, France, to be combined with composite Ge detectors (Clover) [Bec92b] in the EUROGAM II array. At that time, detector development had led to an invention of a segmented Ge crystal, which is a novel way to increase the granularity of an array. Later on, the campaign continued in the form of the EUROBALL III and IV arrays with increased granularity and with further improved γ-ray resolving power. A short overview of the evolution of the γ-ray detector arrays in Europe is shown in Table 2.1.

Table 2.1: Evolution of high-spin γ-ray spectrometers. Different detector arrays reflecting the era from the early NaI(Tl) detector set-ups to the modern high granularity Ge arrays have been compared from the JUROGAM perspective.

Array	Operational year	Number of the crystals in the array	Photo-peak efficiency at 1332 keV	Highlights
NaI(Tl) scintillators	60's	few	-	Rotational band
Ge(Li)	70's	<5	-	Backbending
TESSA3	83-85	30	1%	Superdeformation
EUROGAM I	92-93	60	5.6%	Bifurcation
EUROGAM II	94-96	126	8.1%	Segmented Ge
EUROBALL III	97-98	250	11%	High granularity
JUROGAM	03-	43	4.2%	

Several in-beam γ-ray spectroscopy campaigns have been carried out at the Accelerator Laboratory of Jyväskylä (JYFL). Their success has been based on the instrumentation facilitating the recoil-gating and RDT methods. After the DORIS, JUROSPHERE and SARI campaigns, a bid for a larger Ge-detector array was accepted by the Euroball Owners Committee. This was the start of the JUROGAM project. JUROGAM was put into commission in April 2003. At the moment it is running the second campaign and further plans have already been discussed.

Based on the former EUROGAM I array, the properties of the JUROGAM array are mostly the same as its predecessor [Nol90]. At the time EUROGAM I was commissioned (1992), it made a significant improvement in PT ratio, photopeak efficiency and γ-ray resolving power [Sim97] compared to earlier arrays like TESSA3. At JYFL, the improvement compared to the previous arrays, especially in $\gamma\gamma$-coincidence efficiency, was tremendous. The power of JUROGAM is based on the high efficiency (4.2% at 1332 keV), moderate granularity and high PT ratio. As a stand alone γ-ray spec-

trometer, JUROGAM is classed among the most powerful modern γ-ray spectrometers. Thus, combined with the efficient recoil separator RITU, novel focal-plane spectrometer GREAT and the TDR data acquisition system, they comprise the best instrument currently available to explore proton-rich nuclei in the A=180 region. In such measurements, the γ-ray resolving power is not a relevant parameter to measure the selectivity of the array for weak reaction channels as mentioned earlier.

The JUROGAM array consists of three main parts; 1) the supporting structure (Figure 2.8), 2) the detector frame (Figure 2.9) and 3) the detector modules (Figure 2.10). The adaptation of the JUROGAM array to the RITU separator and K130 cyclotron beam line required some modification. These topics will be discussed below.

2.3.3 Supporting structure

The JUROGAM supporting structure with the detector frame and mounted Ge detectors is illustrated in Figure 2.8. The supporting structure was used earlier with the EUROGAM II array. It holds two carriages on the top. Each carriage bears the load of one hemisphere. The carriages can be driven back and forth with two-gear motors to open/close the sphere. Closing is controlled by two sensors for each hemisphere. When the first one fires, approximately 1.0 cm before the closed-position, the motor shifts into the low gear. The second sensor is at the contact point of the hemisphere and stops the motor when the sphere is closed. This prevents driving the hemisphere across the target chamber and the beam line. The supporting structure is used also as a dock for the cable patch panels, the liquid nitrogen (LN_2) manifolds and the pre-amplifier power units of the Ge detectors and the BGO shields.

The height of the cyclotron beam line at JYFL is 135 cm. As the EUROGAM II array was built for a beam line 175 cm high, the legs of the supporting structure had to be shortened. Also the roof of the measurement cave had to be raised by 1 meter to make the supporting structure to fit in.

2.3.4 Detector frame

The JUROGAM array employs the spherical EUROGAM I detector frame. It splits into two hemispheres opening perpendicular to the beam axis. This allows easy access to the target chamber and enables RITU stand-alone runs with high beam currents without exposing the Ge detectors to high neutron fluxes. The detector frame hangs from the carriages in the supporting structure via six adjustable brackets ie. each of the carriages holds the hemisphere with three brackets (Figure 2.8). The sphere was aligned by adjusting the length and the mounting of each bracket. The top brackets

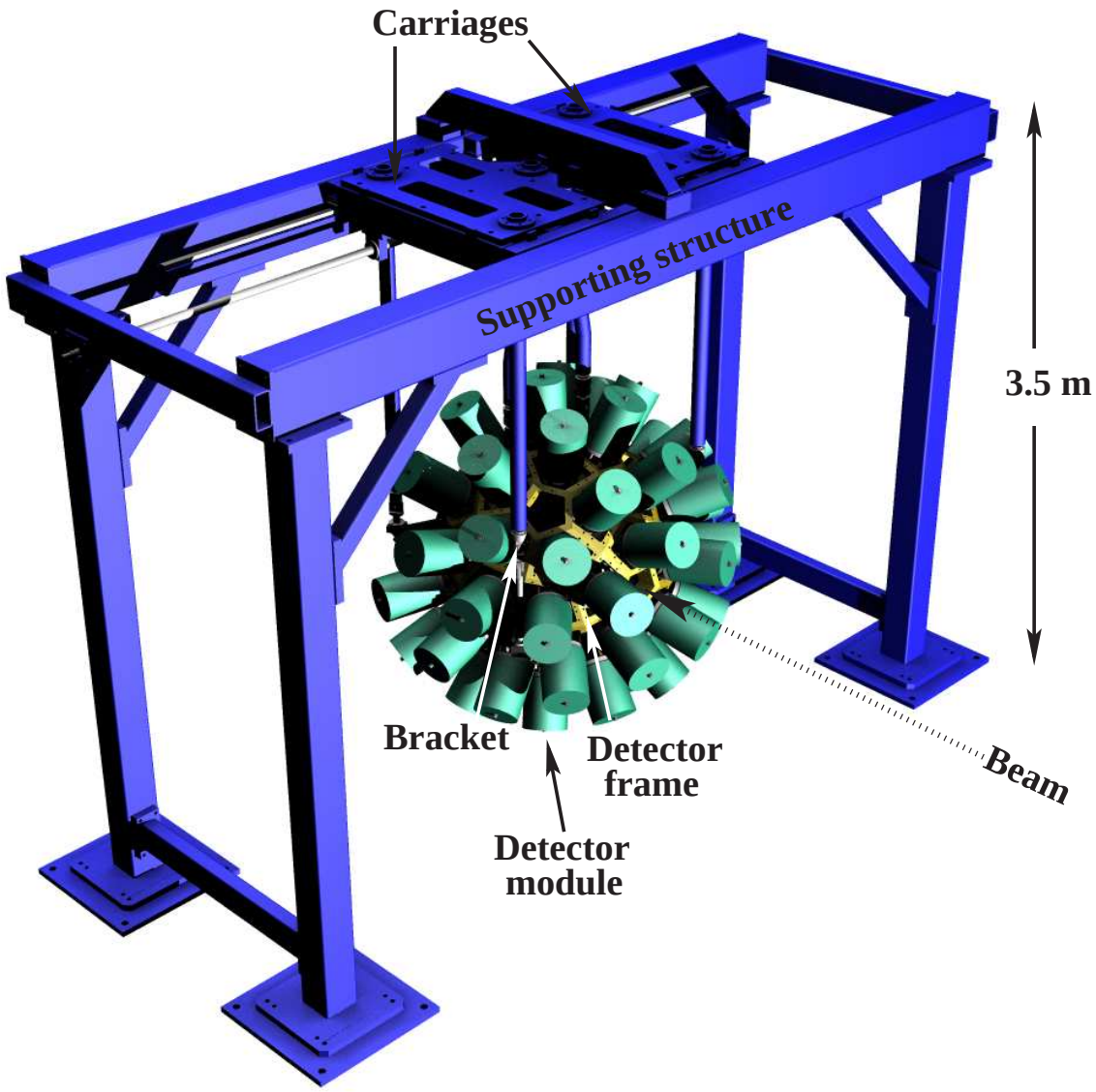

Figure 2.8: Schematic drawing of the JUROGAM supporting structure with the detector frame and the mounted detector modules.

were shortened and folded to fit into the JUROGAM geometry. New connecting parts for other brackets were also designed.

The detector frame consists of 12 regular pentagons (large) forming a dodecahedron (Figure 2.9). Each pentagon is divided into 6 sections, where a small regular pentagon is surrounded by 5 irregular pentagons. Detector modules occupy the irregular pentagons. The entire sphere thus has 60 positions. In such an arrangement, the detector modules can be grouped into rings by the angle of the detector module with respect to the beam axis. Due to this geometry, the whole array holds the detector

modules in eight different rings divided in the following way: 5 detector modules at 158°, 10 at 134°, 10 at 107°, 5 at 94°, 5 at 86°, 10 at 72°, 10 at 46°, 5 at 22°. The close vicinity of RITU forced the two detector rings at forward angles (22° and 46°) to be removed. In addition, two detector modules had to be removed from the ring at 86° due to the space reserved for the RITU support. Consequently, the JUROGAM array consists of 43 detector modules.

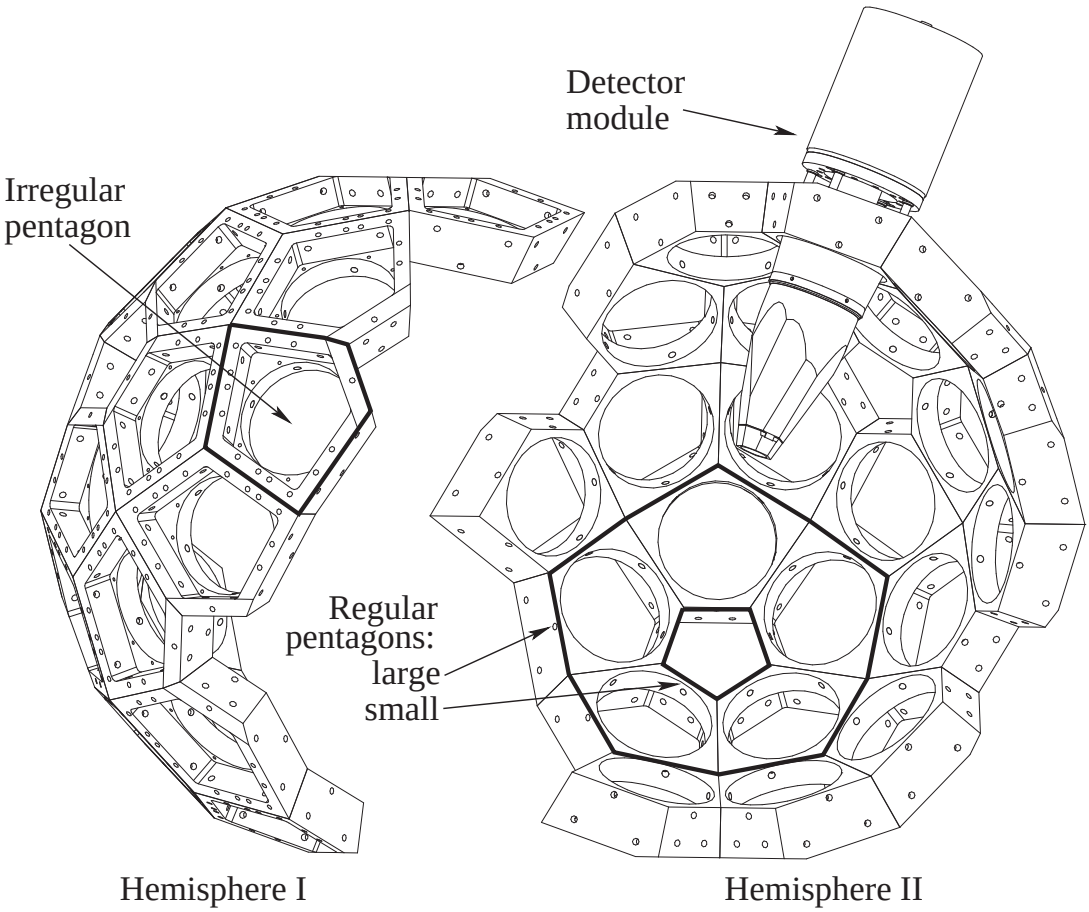

Figure 2.9: Technical drawing of the open detector frame with a mounted Phase I module seen from the end of the RITUseparator. The complete dodecahedron consists of 12 pentagons (large), which are divided into 5 irregular (the detector module positions) and 1 regular pentagons (small).

The detector frame is aligned with the beam line going through a small regular pentagon. Two small regular pentagons are blocked by the sphere brackets and another two are used to allow access to the target chamber window and to the beam viewer camera.

2.3.5 Detector modules

A detector module consists of a high-purity Ge detector and a Compton-suppression shield. They are mounted to the detector frame in the geometry described above. Each module is equipped with a heavy-metal collimator to prevent γ rays from the target hitting the BGO shields. Depending on the experiment, various absorbers in front of the Ge detectors can be used to attenuate the low-energy γ-ray background consisting mainly of the target X-rays. The assembly of a EUROGAM Phase I Ge detector equipped with a BGO Compton-suppression shield is shown in Figure 2.10.

The performance of the detector module (the detection efficiency and energy and time resolution) depends on the properties of the Ge crystal and the signal processing electronics. To maximize the detection efficiency, the Ge crystal must fill the available solid angle completely in the given geometry. On the other hand, the charge collection in the Ge crystal has to be efficient in order to achieve high energy and time resolution ie. the crystal has to endure high electric field (bias voltage). To fulfill these requirements, the Ge crystal is tapered at the front and coaxial at the back. This close-end coaxial form provides high detection efficiency also for the low-energy γ rays, low leakage current, homogeneous electric field across the Ge crystal and wide heat contact with the cold finger [Kno89]. To provide better signal-to-noise response, the signal is first amplified inside the cryostat using a cooled field effect transistor (FET). Thereafter, the signal goes to the pre-amplifier, where it is divided into time and energy channels feeding the shaping amplifiers. The detectors used in in-beam experiments are equipped with an n-type Ge crystal, thus having an extended low-energy efficiency owing to the thin p^+ (0.5 μm) contact on the outside of the crystal. The use of n-type crystals also allows annealing to be performed.

When the EUROBALL campaign was completed, the detectors were delivered to several different user sites, JYFL being one of them. The JUROGAM array consists of detectors of different type and origin. The first JUROGAM campaign started with 49 detectors. Most of them (27) originated from the Euroball collaboration (Phase I-type) [Sim97], 12 detectors were of GASP-type [Ros93] and the rest (10) belonged to the France-UK loan-pool (Phase I-type). The relative efficiency of these detectors compared to a $3'' \times 3''$ NaI(Tl) scintillation detector varies between 54–60%.

The Phase I detectors were produced by two different companies, Ortec and Canberra-Eurisys. Their products differ mainly by the pre-amplifier and cryostat valve. The location of the Ge crystal inside the cryostat varies for different detectors being roughly at a distance of 2 cm from the tip of detector end-cap. However, that does not affect the efficiency of the JUROGAM array as the solid angle of each detector is defined by the collimation, not by the distance between the target and Ge crystal. Some detectors are prototypes with slightly varying crystal dimensions.

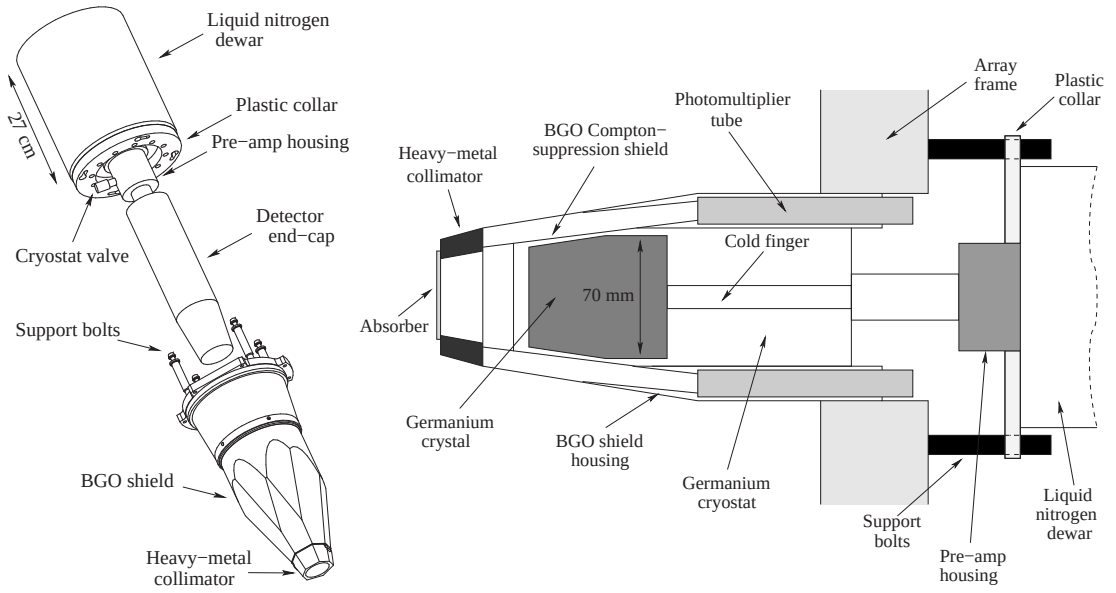

Figure 2.10: Technical and schematic drawing of a Phase I EUROGAM detector module [Nol94].

The GASP detectors were manufactured by Ortec. The crystal volume is larger than in the Phase I detectors due to the larger length. This results in slightly higher photopeak efficiency at higher energy. The geometry is similar to the Phase I detectors, but the tapered form at the front face of the crystal is a little steeper. The dewar is much smaller compared to the Phase I dewars. Consequently, the LN_2 filling cycle was determined by the GASP detectors to maintain stable crystal temperatures. Different JUROGAM detector modules are compared in Table 2.2.

Table 2.2: Properties of the detector modules used in the JUROGAM array. The absolute efficiencies were measured at a distance of 25 cm from the detector end-cap.

Detector	Number of detectors used	Crystal length [mm]	Crystal diameter [mm]	Average absolute efficiency at 1332 keV	Average resolution at 1332 keV	Peak to total [%]
Phase I-Eurisys	27	$\geq$70	69-75	0.063(4)%	2.75(5)	54–58
Phase I-Ortec	10	$\geq$70	69-75	0.070(4)%	2.68(5)	54–58
GASP	12	80	72	0.083(4)%	2.85(5)	60

Several types of Compton-suppression shields have been designed for different Ge-detector arrays. Some of them comprise different scintillator materials (e.g. the TESSA shields). The performance and background suppression of the Phase I detectors is discussed in more detail by Beausang *et al.* [Bea92].

Maintenance of the JUROGAM detectors is taken care of by the γ-group of JYFL.

Repair of the pre-amplifier, detector annealing and change of the cryostat FET have been usual service operations. Detector annealing has to be performed regularly as the Ge crystals are exposed to neutrons produced in fission and fusion-evaporation reactions. Four new annealing stations were constructed for this purpose.

2.3.6 Liquid nitrogen cooling

Ge detectors must be operated at very low temperatures. Typically, the crystal is cooled down to approximately 90 K by using LN_2. A low temperature is maintained via cold finger providing a heat contact with LN_2 stored in a thermally isolated dewar (Figure 2.10). The Ge detectors employed in the experiments are exposed to neutrons. In the course of time the neutrons generate defects in the Ge-crystal lattice. This induces trapping of the charge carriers giving rise to incomplete charge collection. This effect can be delayed by keeping the detectors biased and cold. If a detector warms up, the bias voltage is automatically switched off and the possible neutron damage takes place. In this case, the detector must then be annealed. Therefore, it is essential that the filling system is reliable. The detectors are kept cold, biased and exposed to a strong ^{60}Co source between the experiments. The strong ^{60}Co source creates a low DC-current through the Ge crystal recovering part of the neutron damage.

The LN_2 autofill system can be divided into hardware and software parts. The hardware consists of two subsystems: the storage and the transfer lines of the LN_2 and a Valve Block Assembly (VBA) system. The main storage tank of 11000 liters is located outside the laboratory building and refilled once a week by a private company. A new transfer line was installed to couple the three 300 liter dewars in the measurement cave to the main tank. The LN_2 is delivered from these dewars to eight manifolds through flexible metal hoses. The manifold consists of six outlets. From the manifold, the LN_2 flows through tygothane hoses, which are connected to the detector dewars with bayonets. To avoid LN_2 losses, the hoses are insulated with 10 mm thick foam sleeves. The VBA system is used to control the LN_2 flow in different steps of the filling process. When the filling starts, most of the LN_2 evaporates as the manifolds and transfer lines are at the room temperature. Therefore, purge valves are open until the system has reached LN_2 temperatures preventing the overpressurising of the system. After the VBA system has detected LN_2 in the exhaust sensor of the manifold, the purge valve is closed and valves feeding the detector dewars are opened. The LN_2 flows into the detector dewar until the VBA has detected the LN_2 in the exhaust sensor of the detector. The filling system is controlled by computer software. The JUROGAM detector dewars are filled every 8 hours. Many practical features have been coded into the system. The system can, for example, fill a detector automatically if it observes an increase in the detector temperature. It also sends an alarm to the mobile phone of the liaison person via the WAP-network for unexpected events. The feeding of the

300 liter dewars is independent of the VBA system. The dewars are automatically refilled when they have purged 80% of the contents.

2.4 The RITU gas-filled recoil separator

The gas-filled recoil separator RITU was originally designed for heavy-element studies [Lei95]. Those experiments require high recoil transmission efficiency because of very low ($<$1 μb) production cross sections. Beside the heavy-element studies, the RITU separator has been successfully combined with different γ-ray and electron spectrometers at the target area to study prompt de-excitation employing the recoil-gating or RDT methods.

In-flight recoil separators employ electric and/or magnetic fields to discriminate between the primary beam particles and recoils. The transmission efficiency of a magnetic separator can be increased by filling the field region with dilute gas [Coh58, Ghi88]. The continuous collisions between the recoils and gas atoms result in a narrow charge state distribution of the drifting ions. This enables the separator to transport the ions of an average charge state (q_{ave}) to the focal plane with a minimal image size. As RITU was designed to operate mainly in a gas-filled mode, electric deflecting and focusing elements were not considered.

The layout of the RITU separator is shown in Figure 2.11. The magnetic configuration of RITU is QDQQ, where Q stands for a magnetic quadrupole and D for magnetic dipole. The first, vertically focusing quadrupole element enables improved matching of the recoils to the acceptance of the dipole magnet. The dipole magnet is the deflecting element, which determines the separation properties of the apparatus. The purpose of the quadrupole doublet is to deliver an evenly distributed image of the reaction products over the focal-plane implantation detector. RITU is typically operated at a pressure of 0.6 mbar of He filling gas. Thorough design and continuous development has made RITU one of the most productive recoil separators ever constructed.

The trajectory of a single ion penetrating into a homogeneous magnetic field with a momentum mv can be derived from the Lorentz force as follows

$$\begin{aligned} F = ma = \frac{mv_\perp^2}{\rho} &= Q|(\vec{v} \times \vec{B})| = eq_{ave}v_\perp B \\ \frac{mv_\perp}{eq_{ave}} &= B\rho, \end{aligned} \tag{2.12}$$

where m is the mass of the recoiling ion, a is the centrifugal acceleration of the recoil,

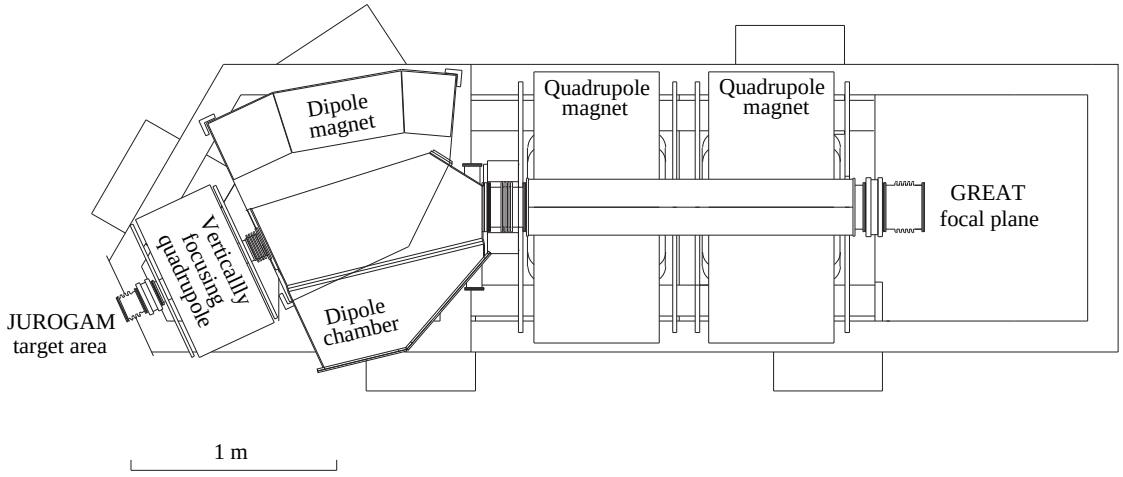

Figure 2.11: Schematic drawing of the gas-filled separator RITU.

$v_\perp$ is the perpendicular velocity of the ion with respect to the magnetic field, ρ is the radius of curvature, Q is the charge state of the ion and B is the magnetic field flux. The product $B\rho$ defines the magnetic rigidity. It describes the capability of a magnet to deflect an ion from the reference track. RITU can operate with magnetic rigidities up to 2.2 Tm.

From the Thomas-Fermi model of an atom [Boh41], the expression

$$q_{ave} = \frac{v}{v_0} e Z^{\frac{1}{3}}, \tag{2.13}$$

where e is a unit charge, $v \approx v_\perp$ and v_0=2.19 $\times 10^6$ m/s (Bohr velocity), can be deduced. Mass m may be written as uA, where u is the atomic mass unit and A is the mass number. Combining these with Equation 2.12, the magnetic rigidity can be given as

$$B\rho = \frac{v_\perp uA}{\frac{v_\perp}{v_0} e Z^{\frac{1}{3}}} = \frac{v_0 uA}{e Z^{\frac{1}{3}}} = 0.0227 \frac{A}{Z^{\frac{1}{3}}}. \tag{2.14}$$

For the recoils, the radius of curvature is fixed and $Z^{\frac{1}{3}}$ is roughly a constant. Thus, RITU can be considered as a mass separator. The bending angle of the RITU dipole is 25° and the radius of curvature is 1850 mm. The focal plane is located at a distance of 4800 mm from the production target. RITU is employed in measurements where high mass-resolving power is not needed. Such measurements are the RDT and recoil-gating measurements, where a small number of fusion-evaporation channels are open.

The transmission efficiency of RITU for the recoils produced in the heavy-ion induced fusion-evaporation reactions employed in the present study, is approximately 30%.

2.5 The GREAT focal-plane detection system

The Gamma Recoil Electron Alpha Tagging (GREAT) spectrometer comprises gas, Si and Ge detectors for the identification and decay spectroscopy of implanted ions. It was designed by a large group of U.K. institutes and funded mainly by the U.K. EPSRC [Pag03]. A schematic drawing of GREAT is shown in Figure 2.12 and the role of different detection elements is briefly discussed below.

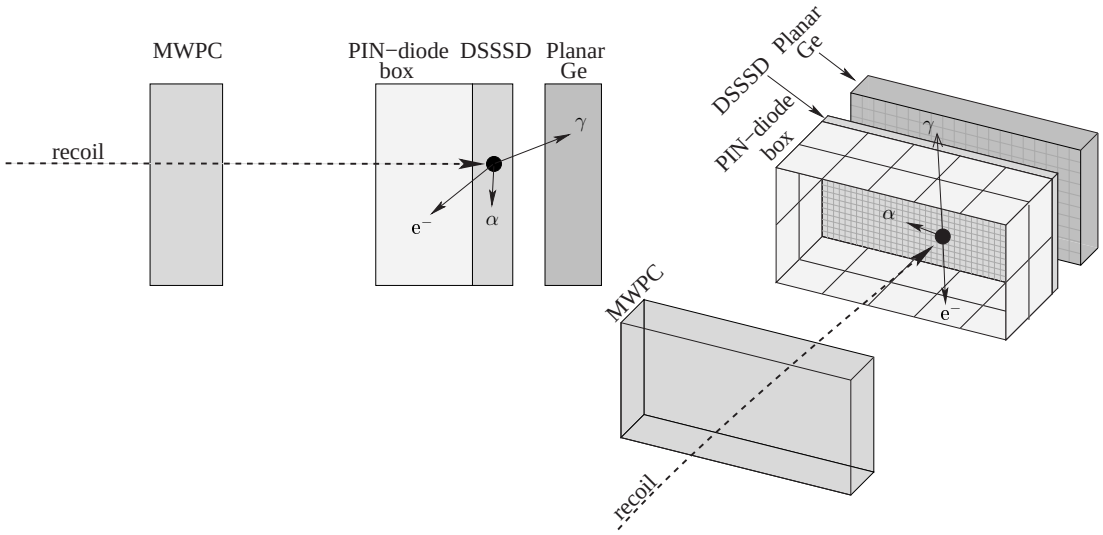

Figure 2.12: Schematic drawing of the GREAT spectrometer.

Before being implanted into the focal-plane detector, the recoils are detected by the transmission MultiWire Proportional Counter (MWPC). The MWPC comprises four cathode wire planes, an anode wire plane and two mylar windows. Its entrance window (131 mm × 50 mm) separates the isobutane of the MWPC from the RITU He gas whereas the exit window separates the isobutane from the GREAT vacuum. The ions propagating through the MWPC detector generate energy loss and timing signals. The position information is obtained by comparing the delay line readouts from the ends of vertical and horizontal wire planes with a fast signal from the anode. The MWPC can be used to distinguish between the recoils passing through it and their subsequent decays, both detected by the implantation detector. Together with the DSSSDs it can be used to discriminate the recoils from the scattered beam particles. The MWPC can operate with counting rates of up to 20 kHz.

The recoils are implanted into two Double-Sided Si Strip Detectors (DSSSD) at the focal plane, each with an active area of 60 mm × 40 mm and a thickness of 320 μm. They are mounted side by side, each consisting of 60 vertical strips in the front and 40 horizontal strips in the back face giving a total of 4800 pixels, thus the strip pitch of each DSSSD is 1 mm in both directions. The active area of the DSSSDs covers approximately 85% of the focal-plane recoil distribution. The DSSSDs are used to detect the incoming recoils and their subsequent decay. The high granularity of the DSSSDs enables a longer search time for the subsequent decay or higher recoil rate in the RDT measurements than the previous implantation detectors employed at RITU.

Degrader foils of two different thicknesses can be used before and after the MWPC to enhance the discrimination between the recoils and scattered beam particles. They can also be used to manipulate the recoil energies when low gains in the DSSSDs are needed and to stop low energy scattered beam.

A box of 28 PIN diodes is mounted upstream of the DSSSDs. Each PIN diode has an active area of 28 mm × 28 mm and a thickness of 500 μm. The PIN diode array was designed to measure energies of conversion electrons emitted in the radioactive decay of recoils implanted into the DSSSDs. In the present work, the PIN diodes were used to observe α-particles which escaped from the DSSSDs.

Low-energy γ rays are measured using a planar double-sided Ge strip detector located behind the DSSSDs. This is enabled by using a thin beryllium entrance window. The rectangular crystal has an active area of 120 mm × 60 mm and a thickness of 15 mm. Each strip is 5 mm wide on both faces giving rise to 288 pixels. The close vicinity of the DSSSDs and position sensitivity could also be utilized in β-tagging experiments.

The planar Ge detector is too thin for efficient γ-ray detection at high energies. Thus, additional detectors are needed for full energy range focal-plane γ-ray spectroscopy. In the present study, two Phase I detectors were mounted above and behind the DSSSDs in transverse geometry. Later on, a clover Ge detector was mounted above the DSSSDs for further experiments. The clover detector has four crystals in close geometry, which are electrically divided into four segments resulting in a total of 16 active detection regions. Segmentation reduces the counting rates and multiple hits in each channel and enables a spatial correlation with the planar Ge detector. The clover is surrounded with a BGO Compton-suppression shield to improve its PT ratio. A future plan is to construct a focal-plane Ge-detector array of four similar clover detectors.

2.6 The Total Data Readout novel data acquisition system

The challenges in nuclear structure studies maintain the development of experimental devices and methods. To take the maximum advantage of the modern techniques, the data losses are unacceptable. This sets requirements for the data acquisition system.

A conventional method in the recoil-gating and RDT experiments has been the use of a common hardware trigger. It opens up a time window for the event data collection. This causes dead time losses as data cannot be processed until the event is read out. The dead time in conventional systems can easily reach tens of percents. The dead time problem has been solved by means of the Total Data Readout (TDR), which is a triggerless data acquisition system. In the TDR, each channel is run independently and associated in software with data words. Each data word is timestamped with a global 100 MHz clock. The data are then reconstructed in the Event Builder using temporal and spatial correlation. The only dead time arises from the analog shaping and conversion times of the individual channels, which is typically of the order of 10 μs. There is no system dead time as no hardware generated master gate is used.

The TDR data acquisition system is shown schematically in Figure 2.13. The front-end electronics comprises commercial NIM/CAMAC units. All the signals are fed into the VXI ADCs via shaping amplifiers and gated by logic signals from the corresponding Constant Fraction Discriminators (CFDs), except a few MWPC signals. They are processed with Time-to-Amplitude Converters (TACs) making use of delay line readouts and are further directed to the VXI ADCs, where they are gated with corresponding CFD signals. The timestamp is recorded for each channel at the start of its gate. The VXI ADCs pass the converted data with associated timestamps to an Event Builder. It merges and formats the data for transfer to storage media and to the on-line sorting devices.

The JUROGAM+GREAT detection system consists of several hundred electronics channels (512 channels available in total) and generates large amounts of data. The data are filtered in the Event Builder by using a software trigger. This reduces the required storage space and lightens the data processing. The DSSSD OR gate is a typical software trigger when employing the RDT measurements at JYFL. TDR provides the user with a large variety of event reconstruction possibilities. It was developed as a part of the GREAT project, but its advantages are also employed in the JUROGAM measurements.

The TDR system was employed in the present work. The data were stored to DLT-tapes for further analysis, which was carried out by using the GRAIN software package [Rah05]. The $\gamma\gamma$-coincidence analysis was completed with the RADWARE software

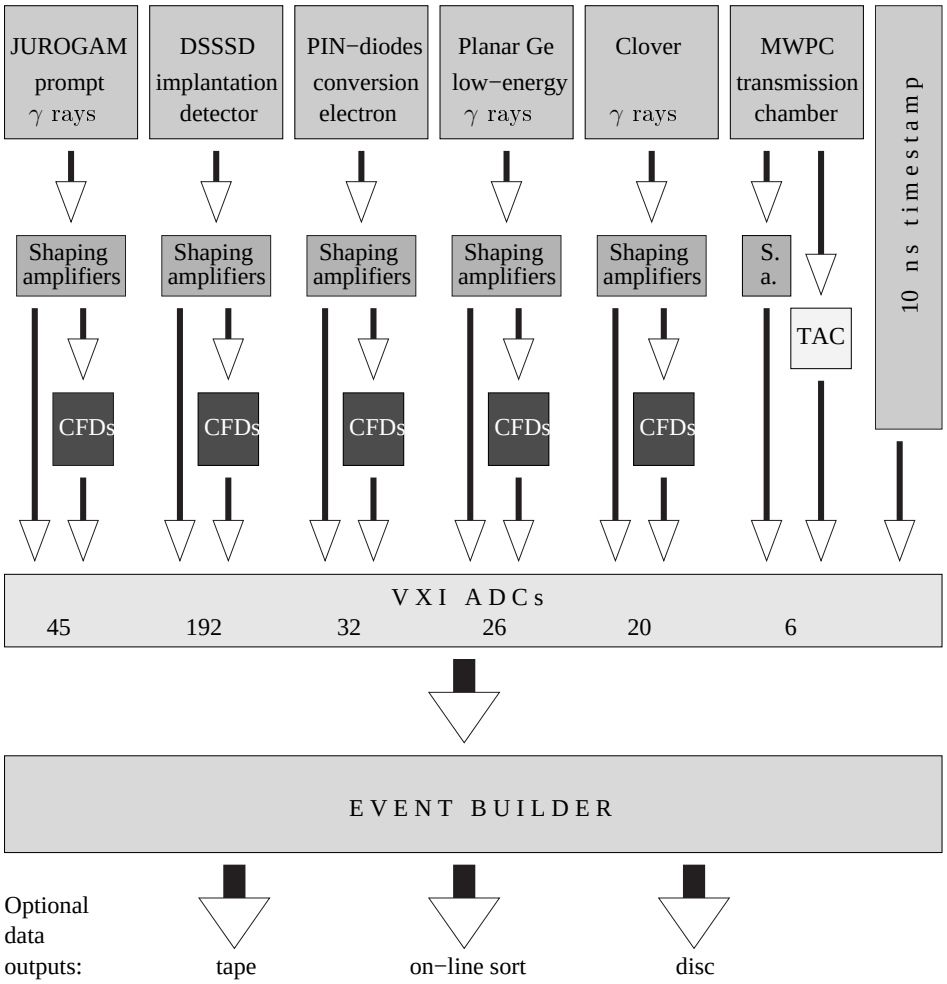

Figure 2.13: A block diagram of the TDR electronics for the JUROGAM and GREAT detectors.

package [Rad00]. Sorting of the data will be described in more details in the following chapter.

3 Experimental study of ^{186}Pb

In the present work, the structure of the neutron mid-shell nucleus ^{186}Pb was investigated for the first time in a RDT measurement. The experiment was performed at the Accelerator Laboratory of the University of Jyväskylä (JYFL) using the JUROGAM+RITU+GREAT set-up combined with the TDR system. The bombarding heavy ions were produced in the 14 GHz ECR ion source [Koi01] and accelerated by the K130 cyclotron [Hei95]. A beam of ^{83}Kr ions was accelerated to an energy of 355 MeV and used to populate excited states of ^{186}Pb via the ^{106}Pd(^{83}Kr,3n)^{186}Pb reaction. The ^{106}Pd target was a metallic foil of thickness 1 mg/cm^2 and 98.5% isotopic enrichment. The average beam current of 6 pnA yielded an average counting rate of 200 Hz in the focal-plane DSSSDs. During 151 hours of effective beam time approximately 10^6 ^{186}Pb α particles, including escape events, were recorded. This resulted in 6×10^5 recoil-gated α-tagged prompt $\gamma\gamma$-coincidence events associated with ^{186}Pb.

Earlier attempts to perform an in-beam RDT measurement for ^{186}Pb have been difficult due to relatively long life-time of 4.83 s [Wau94], thus they have been based on recoil-γ^n coincidence measurements. The first observation of the yrast band in ^{186}Pb was reported by Heese *et al.* [Hee93], where the yrast states up to I^π=12$^+$ were measured. In a simultaneous measurement, Baxter *et al.* were able to extend the band up to I^π=14$^+$ [Bax93]. A similar study employing an improved detection system was recently carried out by Reviol *et al.* [Rev03]. They confirmed the yrast-band states and assigned the level spins on the basis of γ-ray angular distribution analysis. They also observed a few non-yrast transitions, but were not able to place them into the level scheme. All these three experiments utilized recoil-$\gamma\gamma$ coincidences.

In following sections, the analysis of the ^{186}Pb data and the results achieved in the present work are discussed.

3.1 Energy calibrations

Si-strip detectors

The calibrations of the GREAT strip detectors were made in two steps. First, every vertical and horizontal strip was gain matched using an external open α source con-

taining a mixture of ^{239}Pu, ^{241}Am and ^{244}Cm nuclei giving rise to an α spectrum with three dominant peaks at 5155, 5486 and 5805 keV, respectively [Fir96]. In the experiment, decaying recoils were implanted into the DSSSDs and the recoil energy of the daughter nuclei was measured together with the α-decay energy. To take into account the recoil energy of the daughter nuclei, an internal calibration was made for each strip. This was done by using α peaks originating from known isotopes ^{185,183}Hg and ^{186}Pb, implanted in the DSSSDs during the same irradiation. After the calibration, the energy resolution (FWHM) of the DSSSDs at 5805 keV was approximately 40 keV.

PIN diodes

The PIN diodes were calibrated using the same three-line α source that was used for the DSSSD calibration. Internal calibration was not needed, since the particles of interest penetrated into the PIN diodes from outside of the detectors. Accurate calibration was anyway necessary, since the PIN diodes were used for the detection of escaping α particles. A resolution of 60 keV for the PIN diodes was obtained after calibration.

JUROGAM Ge detectors

Energy calibration and gain matching of the JUROGAM Ge detectors were done using two different sources, ^{152}Eu and ^{133}Ba. These sources emit several γ rays over a wide energy range from 80 keV to 1408 keV. Due to the non-linearity of the ADCs at low energies ($<$120 keV), the γ-ray energy range was narrowed to 244-1408 keV. This was found reasonable as no γ rays below 261 keV were observed in the present experiment. Thirteen different γ-ray energies were used, which was sufficient to obtain a reliable energy calibration for the γ-ray transitions observed in the present work. Moreover, the Doppler effect (see Section 2.3.1) was considered to establish a precise energy calibration over the different Ge-detector rings. After calibrations and the Doppler shift corrections, the resolution of 4.5 keV at 662 keV for the JUROGAM array was obtained.

The ^{152}Eu and ^{133}Ba sources were also employed in the efficiency calibration of the JUROGAM Ge detectors. The relative efficiency calibration was based on the known γ-ray intensities of these sources [Trz90]. The absolute detection efficiency curves shown in Figure 2.7 have been normalized using the measured absolute efficiency for the 1332 keV γ rays from a calibrated ^{60}Co source.

3.2 Gating conditions

This section describes the gating procedure used in the present RDT-measurement. The total singles spectrum of the DSSSDs is shown in Figure 3.1. Alpha particles are clearly seen as discrete peaks in the expected energy range of 5-6.5 MeV, while the recoils exhibit as a smooth distribution around 17 MeV. The escaping α particles leave only a part of their energy in the DSSSDs, resulting in a tail on the low-energy side of the α peaks. The scattered beam particles have higher energies (>30 MeV). The primary beam particles did not reach the focal plane and they would have been outside of the plotted energy range.

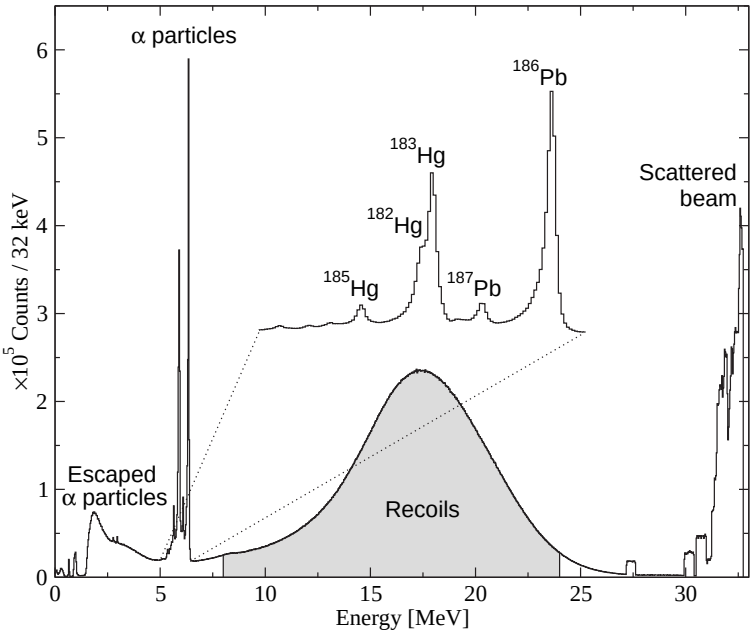

Figure 3.1: Total singles energy spectrum observed in the GREAT strip detectors from the reaction ^{106}Pd+^{83}Kr at the beam energy of 355 MeV. Magnified part shows the α-particle spectrum from decaying recoils.

Recoil identification

In the Event builder, the DSSSD OR signal was chosen to be the software trigger defining the event time. It also reduced the needed storage space by demanding the trigger signal to be present when recording an event to the disc and tape.

Any event in the DSSSDs could trigger an event. Therefore, three conditions were set to discriminate recoils from, for example, the scattered beam particles:

1. Recoil energies measured in the GREAT strip detectors, shown as a shaded area in Figure 3.1 (8-24 MeV).
2. Recoil time-of-flight between the MWPC and the DSSSDs, as shown in Figure 3.2(a).
3. Recoil energy loss in the MWPC (dE), as shown in Figure 3.2(b).

The last two conditions were combined by constructing a two dimensional (2D) gate on the dE vs. ToF matrix as shown in Figure 3.2(c). Projections from this matrix are shown in Figures 3.2(a) and (b). Recoils, depositing more energy than the scattered beam particles, are again shaded. Good separation between recoils and scattered beam can be already seen from these two figures, but the best discrimination was achieved by using the 2D gate shown Figure 3.2(c).

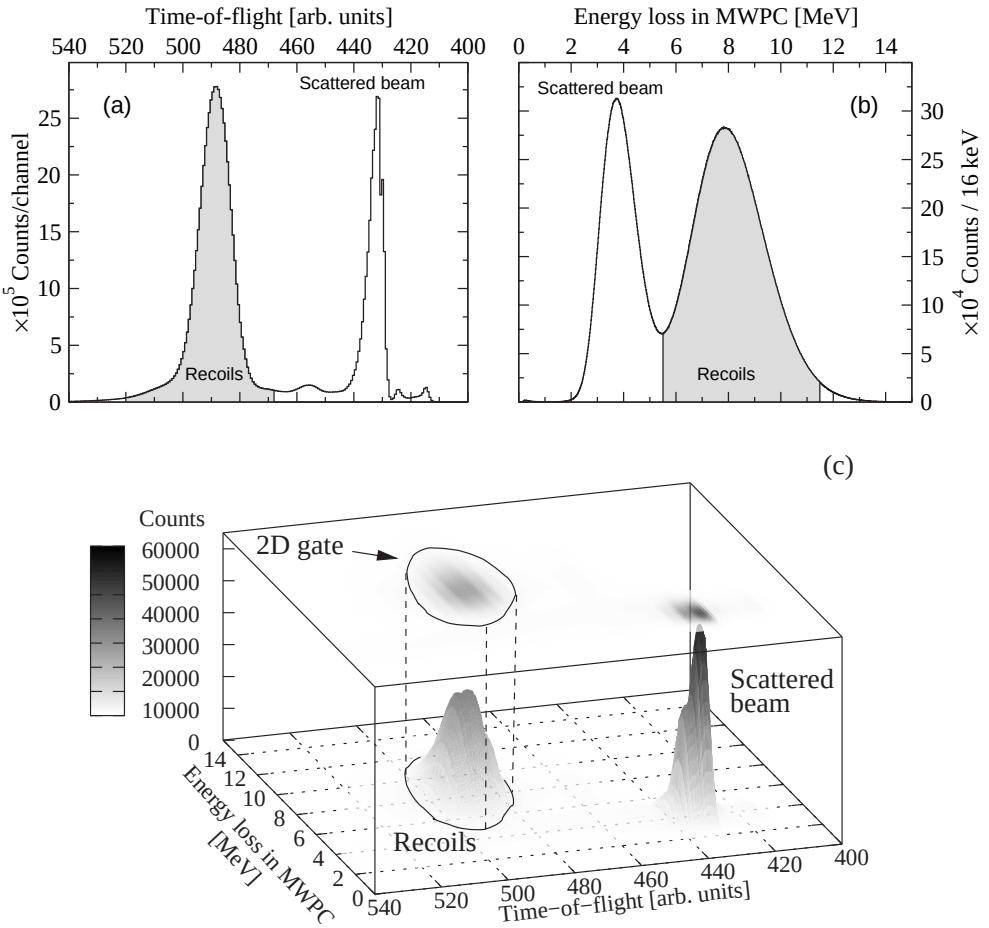

Figure 3.2: (a) Time-of-flight of particles from the MWPC to the DSSSDs. (b) Energy loss of particles in the MWPC. (c) Energy loss in the MWPC vs. the time-of-flight with 2D gate shown as a projection in xy-plane.

Alpha tagging

The α spectrum correlated with recoils is presented in Figure 3.3. The figure shows a clear separation between ^{186}Pb α particles and α particles resulting from other reaction products. Prompt γ rays corresponding to the observation of a recoil together with a subsequent α decay at the same position in the focal plane DSSSDs within 15 s were selected in the data analysis. This was approximately three times the half-life of ^{186}Pb ($T_{1/2}$=4.83 s [Wau94]).

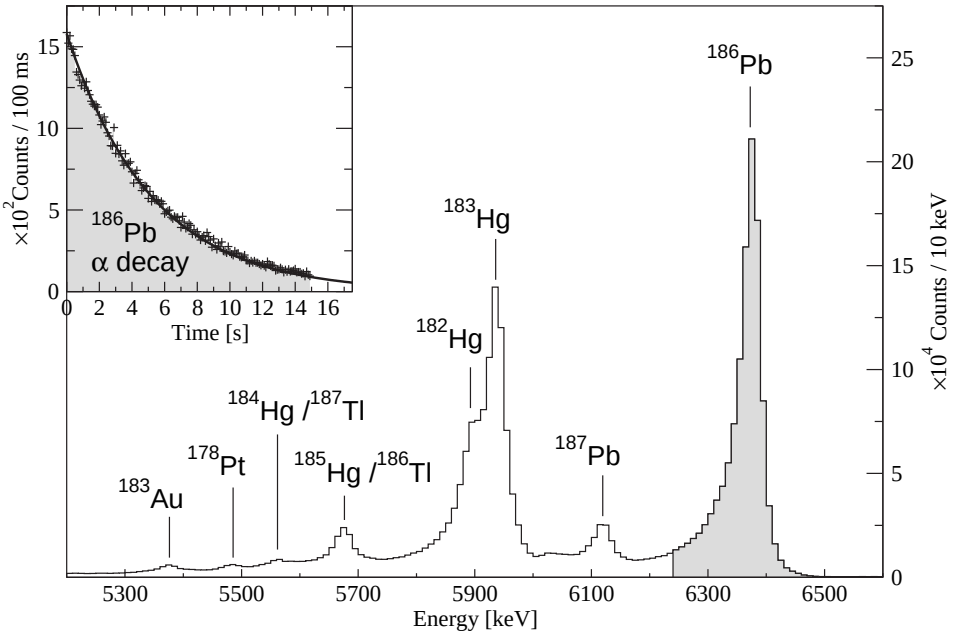

Figure 3.3: Energy spectrum of α particles from the ^{83}Kr+^{106}Pd reaction detected in the DSSSDs of the GREAT spectrometer within 15 s of the implant of a recoil. The inset shows the time difference between the implantation of a recoil and the observation of a ^{186}Pb α decay in the same pixel within 15 s. The shaded areas represents the energy and time gates.

Escaping α particles within the same time window were collected using the PIN diode box. The collection was established by summing the energies measured in coincidence by the DSSSDs and PIN diodes (within 500 ns). If the sum energy corresponded to the α-decay energy of ^{186}Pb, the event was used for tagging. The sum gate is visualized in Figure 3.4(c), where the PIN diode energy vs. the DSSSD energy is plotted. Again, the 2D gate was found to give the best response. It is obvious, that the PIN diode energy does not decrease linearly with the increasing DSSSD energy. This non-linearity arises from the drift length of α particles in the dead layer of the DSSSDs; the longer the drift length inside the DSSSD, the higher the energy loss inside the DSSSD and in its dead layer. Therefore, the 2D curve bends down at higher DSSSD energies. The functionality of the method is demonstrated in Figures 3.4(a) and (b). In Figure

3.4(a) a half-life comparison between α particles leaving full energy in the DSSSDs and escaping α particles has been carried out. The fitted half-lives agree to within 2%. Figure 3.4(b) shows the sum energy of escaped α particles. It is obvious that α peaks are broadened due to the energy losses in the dead layers of the DSSSDs and PIN diodes. This is displayed as a tail on the low-energy side of the dominant α decays (marked). Different threshold and offset conditions of the PIN diodes resulted in the peak-like structures at low energy. They consist mainly of noise and a small contribution from β decays and internal conversions. The shaded area demonstrates the correlated α particles, detected inside the DSSSDs, which have been used for tagging.

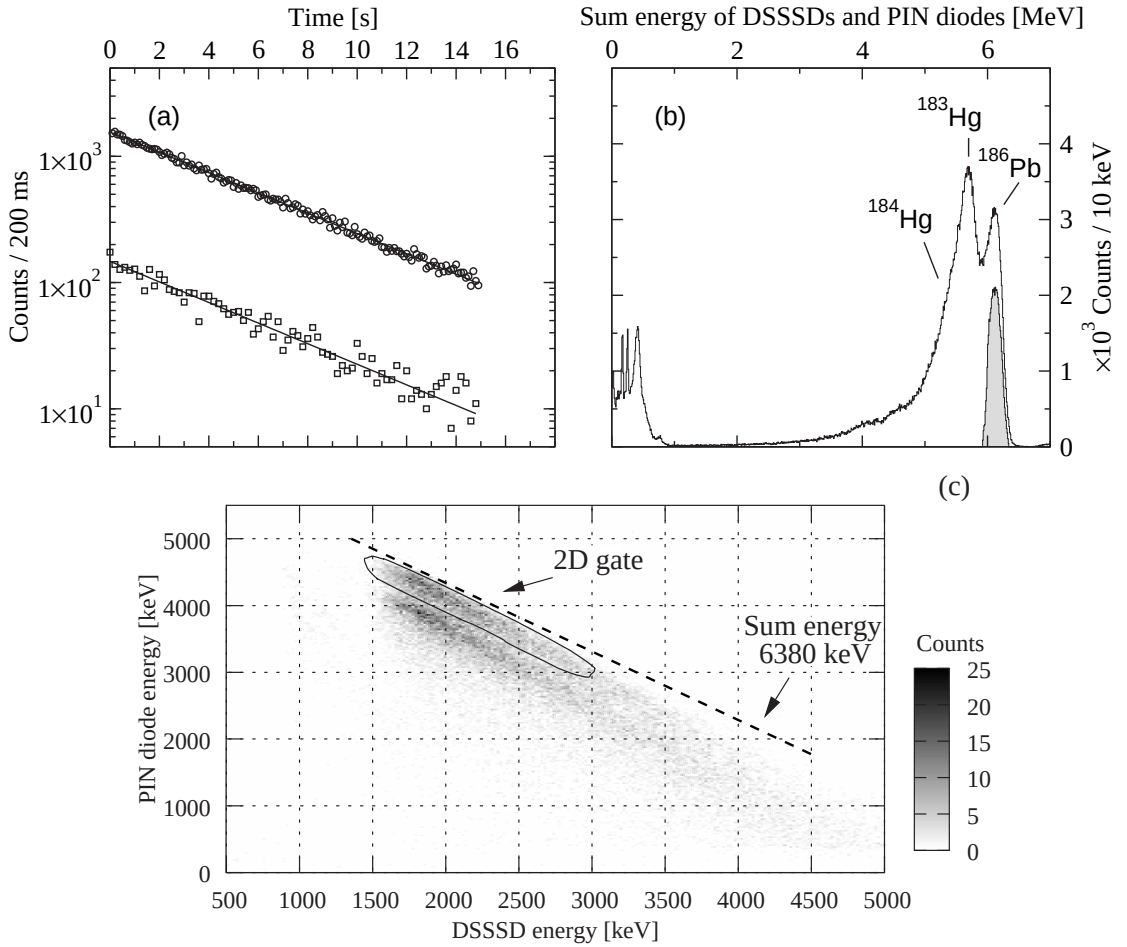

Figure 3.4: (a) Decay curve of ^{186}Pb measured by observing the escaping α particles (open squares). The corresponding decay curve obtained via observation of α particles inside the DSSSD is shown for comparison (solid circles) (b) The sum energy of the DSSSDs and PIN diodes in coincidence. The shaded area corresponds the escaped α particles used for tagging. (c) PIN diode energy vs. escaped α-particle energy with the combined 2D gate. The dashed line shows the sum energy corresponding ^{186}Pb α decay.

Alpha particles, including escape α's, fulfilling the conditions mentioned above were

used for tagging. A comparison of the γ spectra obtained by tagging with the ^{186}Pb α decay events inside the DSSSDs and with the escaping ones is made in Figure 3.5. Correspondence between these two spectra is perfect establishing the feasibility of the method. The use of escaping α particles for tagging enhanced the $\gamma\gamma$-coincidence data by approximately 6%. Higher enhancement would have required wider 2D gate on PIN-DSSSD matrix and thus given rise to wrong α-recoil correlations.

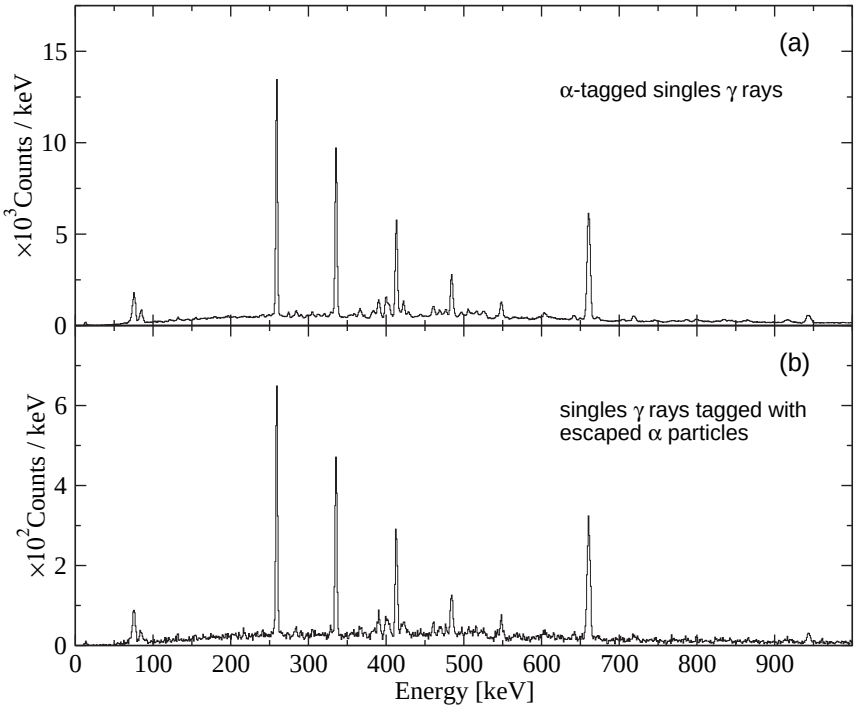

Figure 3.5: The comparison of γ spectra obtained by (a) tagging with ^{186}Pb α decay inside the DSSSDs and (b) tagging with escaping ^{186}Pb α particles.

The power of the JUROGAM+RITU+GREAT set-up combined with the TDR-system is demonstrated in Figure 3.6, which shows γ-ray energy spectra from the ^{83}Kr+^{106}Pd reaction using different gating conditions. Figure 3.6(a) shows the total singles γ-ray energy spectrum. The spectrum is dominated by the 511.8 keV transition from the Coulomb excited 2_1^+ state in ^{106}Pd. The large width of the peak is due to the Doppler shift arising from incorrect velocity correlations. Figure 3.6(b) shows the γ rays in coincidence with recoils, where the most intense peaks originate from the nuclei produced via dominant fusion-evaporation channels. Figure 3.6(c) presents γ rays tagged with ^{186}Pb α decays and reveals yrast-band transitions in ^{186}Pb. To give a scale for the selectivity, in a spectrum projected from the recoil-gated α-tagged $\gamma\gamma$-coincidence data with a gate on the $10_2^+ \rightarrow 8_2^+$ transition, the $12_2^+ \rightarrow 10_2^+$ transition (508 keV) peak contained approximately 30 counts. The corresponding region in the total γ-ray singles spectrum contained over 10^7 counts. It should also be noted, that these spectra have been BGO vetoed ie. the true γ-ray flux is even higher.

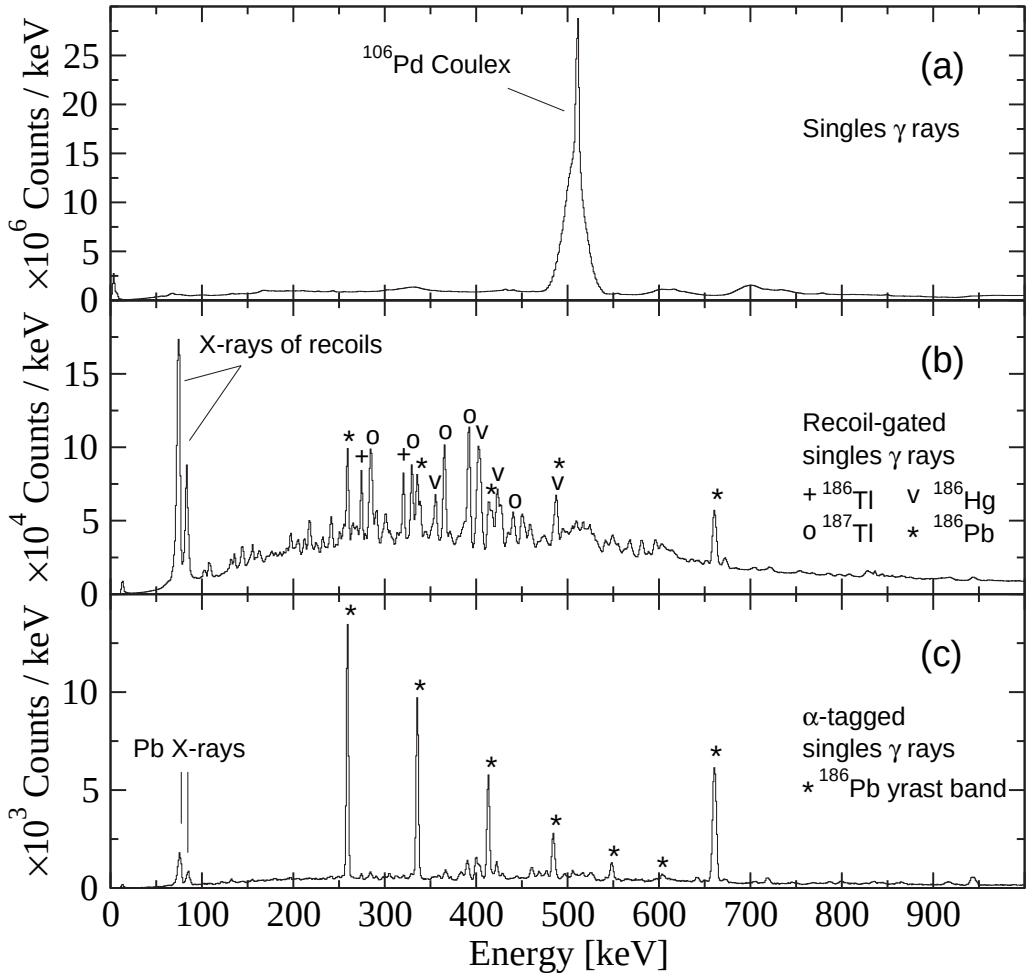

Figure 3.6: Gamma-ray energy spectra detected by the JUROGAM from the ^{106}Pd+^{83}Kr reaction at the beam energy of 355 MeV. (a) the total γ-ray energy spectrum. (b) Gamma-ray energy spectrum gated by recoils. (c) Gamma-ray energy spectrum extracted by tagging with ^{186}Pb α decays.

Gamma-ray timing constraints

Recoil transmission time through RITU is constant, which makes RDT measurements feasible. The prompt γ rays were associated with the corresponding α-tagged recoils observed in the DSSSDs by demanding a delayed-coincidence relation. With the present reaction kinematics the delay was approximately 500 ns. For comparison, the average time between two recoil-$\gamma\gamma$ events was approximately 40 ms (25 Hz). As the event time was set zero by the DSSSDOR signal, the γ rays were detected 500 ns in advance. This is confirmed in Figure 3.7, where a Ge time is plotted (time goes "backwards" as the DSSSDOR signal was used as a virtual start signal). It is dominated by one clear peak (50 μs at FWHM), originating from prompt γ rays following nuclear reactions. The regular small humps in the spectrum correspond the γ rays originating from random

events. Thus, the cyclotron frequency can be deduced from the distance between the humps. The shaded area in the figure shows the gate set for the recoil-γ coincidence condition. In the inset of Figure 3.7, the time spectrum of recoil-α-$\gamma\gamma$ events fulfilling the gating conditions is shown.

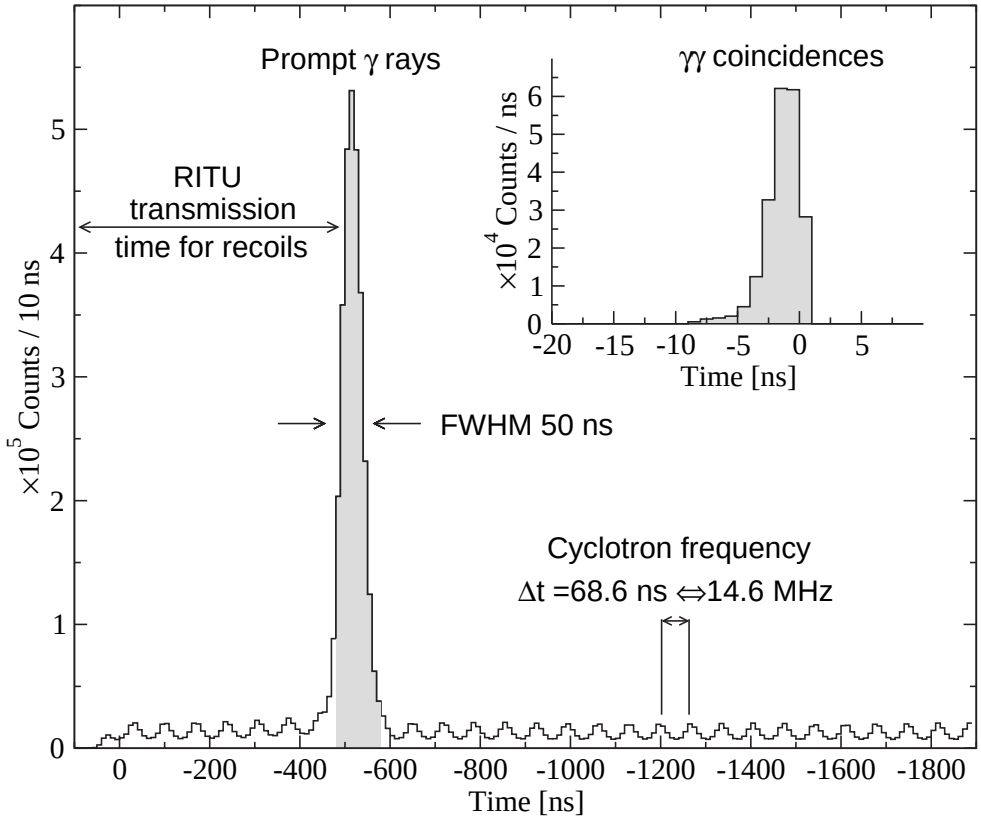

Figure 3.7: Time spectrum of the JUROGAM detectors. Event time was set zero by the DSSSD OR signal. The time difference of coincidence γ events is shown in the inset. The shaded areas correspond γ rays which passed the time gates.

3.3 Results

The high efficiency of the JUROGAM Ge array enabled a collection of a sufficient amount of RDT $\gamma\gamma$-coincidence events to place a large number of new transitions into a level scheme, some of them being published in References [Pak05a] and [Pak05b]. Due to the long α-decay searching time, random correlations from the ^{186,187}Tl and ^{184,186}Hg nuclei gave rise to contaminant peaks in γ-ray spectra (contaminant level approximately 2% for each major contaminant nuclei). This made the $\gamma\gamma$-coincidence analysis more complicated as several γ rays originating from these nuclei overlapped with the ^{186}Pb γ-ray energies.

Transitions associated with ^{186}Pb are listed in Table 3.1 together with intensities and angular distribution information when available. The level scheme deduced for^{186}Pb, incorporating over 20 new states and 38 new γ rays, is shown in Figure 3.8. The scheme was constructed using the coincidence relations and intensity balances in the recoil-gated, α-tagged $\gamma\gamma$-coincidence data.

Transition multipolarities can be deduced from the angular distribution ofγ rays. In this technique, the Ge detectors are grouped by their detection angles (θ) with respect to the beam direction. The variation ofγ-ray intensity as a function of detection angle can be expressed as

$$W(\theta) = A_0 + A_2 P_2(cos\theta) + A_4 P_4(cos\theta), \tag{3.1}$$

Table 3.1: The γ-ray transitions measured for ^{186}Pb in the present work. Gamma-ray energy (E_γ), level energy (E_i), relative intensity (I_{rel}), (tentatively) assigned initial and final levels(I_i and I_f) and angular distribution information (A_2/A_0 and R) are listed.

E_γ [keV]	E_i [keV]	I_{rel}	I_i	I_f	A_2/A_0	R
260.6(1)	922	790(80)	4_1^+	2_1^+	-0.08(4)	0.9(2)
307(2)	1307	<6	(5_1^+)	(4_2^+)		
337(1)	1643	<7	(5_1^+)	(3_1^+)		
337.1(1)	1259	740(70)	6_1^+	4_1^+	-0.02(3)	1.1(2)
361.8(5)	1306	9(4)	(3_1^+)	(2_2^+)		
369.1(4)	2962	9(3)	(11_1^-)	(9_1^-)		
383.9(4)	1306	11(5)	(3_1^+)	2_1^+		
391.5(2)	1337	40(7)	(4_2^+)	(2_2^+)	-0.1(2)	0.9(4)
401.3(2)	1738	55(7)	(6_2^+)	(4_2^+)		1.1(3)
405.3(6)	2049	7(3)	(7_1^+)	(5_1^+)		
414.5(5)	1337	21(7)	(4_2^+)	4_1^+		
414.8(1)	1674	560(50)	8_1^+	6_1^+		
419.5(3)	3381	4(3)	(13_1^-)	(11_1^-)		
424.1(2)	2162	42(5)	(8_2^+)	(6_2^+)	0.15(5)	1.5(1.0)
461.3(7)	3842	11(3)	(15_1^-)	(13_1^-)		
462.7(2)	2625	39(5)	(10_2^+)	(8_2^+)		
469.5(4)	2518	16(4)	(9_1^+)	(7_1^+)		
478.8(2)	1738	38(5)	(6_2^+)	6_1^+	-0.2(2)	0.6(3)
485.8(5)	2160	280(30)	10_1^+	8_1^+	0.08(7)	1.4(4)
487.4(4)	2162	23(6)	(8_2^+)	8_1^+		
498.4(7)	3842	<2	(17_1^-)	(15_1^-)		
507.6(3)	3132	18(3)	(12_2^+)	(10_2^+)		
527(1)	3045	<4	(11_1^+)	(9_1^+)		

Table 3.1 (continued): The γ-ray transitions measured for ^{186}Pb in the present work. Gamma-ray energy (E_γ), level energy (E_i), relative intensity (I_{rel}), (tentatively) assigned initial and final levels(I_i and I_f) and angular distribution information (A_2/A_0 and R) are listed.

E_γ [keV]	E_i [keV]	I_{rel}	I_i	I_f	A_2/A_0	R
543(1)	3409	<3				
549.6(6)	2710	134(9)	12_1^+	10_1^+	0.16(9)	1.3(4)
551.3(9)	3684	5(3)	(14_2^+)	(12_2^+)		
605.6(8)	3315	71(5)	(14_1^+)	12_1^+		
645(1)	1306	<5				
652.2(5)	3967	22(2)	(16_1^+)	(14_1^+)		
662.2(2)	662	1000(60)	2_1^+	0_1^+	-0.04(2)	1.0(2)
668(2)	4635	<10	(18_1^+)	(16_1^+)		
673(1)	5308	<5	(20_1^+)	(18_1^+)		
674.5(6)	1337	14(5)	(4_2^+)	2_1^+	0.05(13)	
705.5(4)	2866	<3	(3_1^+)	2_1^+		
720(2)	1643	19(6)	(5_1^+)	(4_1^+)	-0.07(15)	
749(3)		<3				
772(3)		<3				
790(4)	2049	9(4)	(7_1^+)	(6_1^+)		
801.2(5)	2961	10(3)	(11_1^-)	(10_1^+)		
835(2)		<4				
844(3)	2518	<3	(9_1^+)	(8_1^+)		
867(3)		<4				
918.1(3)	2592	12(4)	(9_1^-)	(8_1^+)	-0.3(2)	
945.2(3)	945	51(6)	(2_2^+)	0_1^+	0.0(2)	1.0(4)
1026(2)	2288	10(5)			-0.2(3)	
1112(3)		<5				
1207(4)		<10			-0.1(3)	

where A_k are the angular distribution coefficients and $P_k(cos\theta)$ are the Legendre polynomials [Yam67]. The angular distribution coefficients can be expressed as $A_k = \alpha_k A^{max}$, where α_k is an attenuation coefficient and A^{max} denotes completely aligned spins. α_k depends on the spin, the distribution over the m substates and the multipolarity of the preceding transition [Yam67, Mat74].

Alternatively, the transition multipolarity can be extracted from experimental data by means of angular correlations. In such a method, the intensities of two γ rays emitted at different angles are compared [Kra73]. This can be established by constructing two $\gamma\gamma$-coincidence matrices, where the γ-ray energy observed in one Ge detector ring is plotted against γ-ray energy observed by any Ge detector in the array. This method is not sensitive to the multipolarity of the gating transition. The γ-ray intensities are defined from γ-ray spectra, which are gated or projected onto the axis of a single

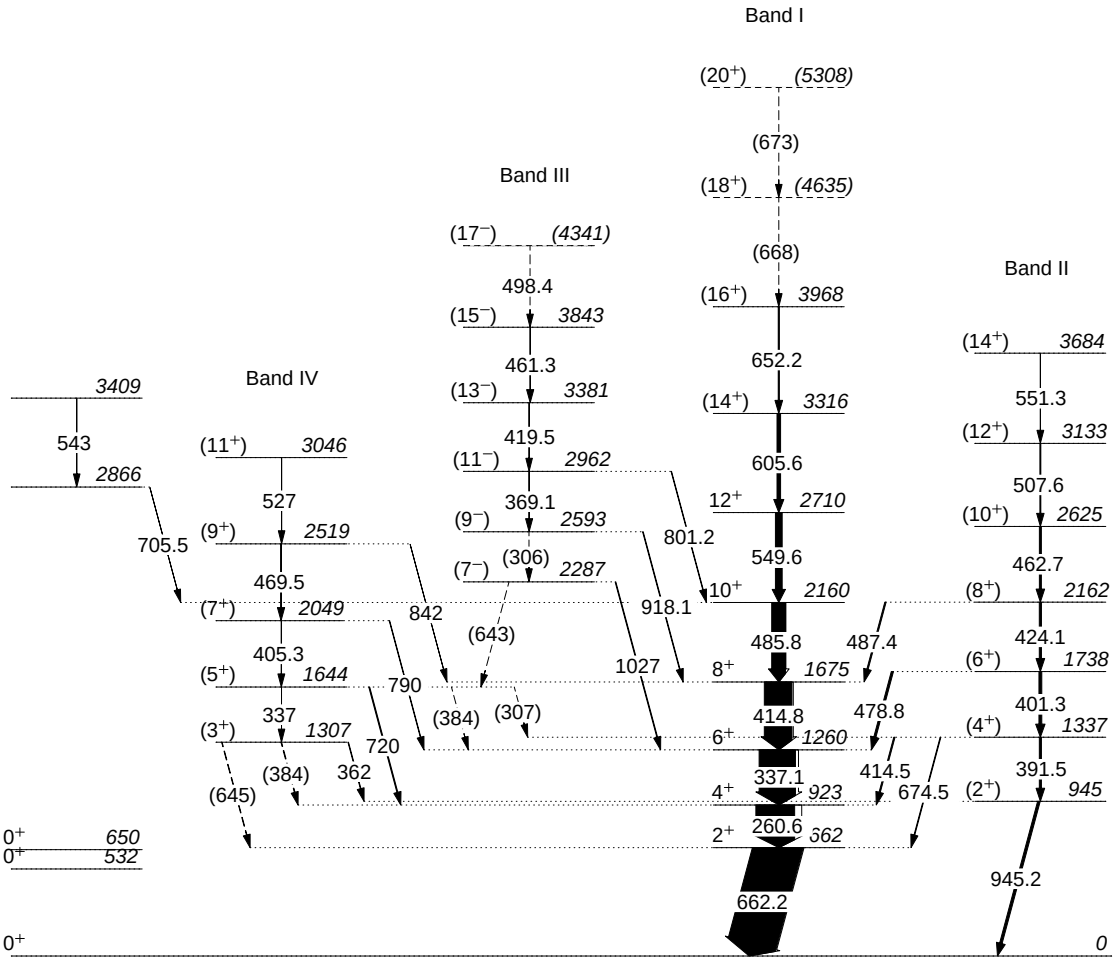

Figure 3.8: Level scheme of ^{186}Pb deduced from the present data (the two 0^+ states on the left side are taken from ref. [And00]). Bands have been named in decreasing order of their intensities.

detector ring in the $\gamma\gamma$-coincidence matrix. Thus R can be read as

$$R = \frac{\text{Intensity of } E_\gamma(157.60^\circ)}{\text{Intensity of } E_\gamma(85.84^\circ + 94.19^\circ)} \tag{3.2}$$

where $E_\gamma(\theta)$ is γ-ray energy at observation angle θ. The method requires greater statistics as it employs $\gamma\gamma$ coincidences.

In the present work, the A_2/A_0 ratios were deduced by fitting the α-tagged γ-ray singles data to Equation 3.1. Angular correlation ratios (R) between two different angles (157.60° and 85.84°+94.16°) were also determined. These values are listed in Table 3.1 when available. Deduced values for A_2/A_0 and R were verified with theoretical predictions and with the values deduced for the known transitions of different mul-

tipolarities. For a known stretched $E2(25/2^+ \rightarrow 21/2^+)$ transition in ^{187}Tl a ratio R of 1.2(2) was observed, while for a dipole $11/2^- \rightarrow 9/2^-$ transition in ^{185}Tl the corresponding value was 0.6(2). These ratios are in accord with the theoretical predictions of 1.45 and 0.73, respectively. Theory predicts an A_2/A_0 ratio of -0.15 for $E2(6^+ \rightarrow 6^+)$ transitions, whereas for R (between angles of 157.60° and 85.84°+94.16°) it gives a ratio of 0.82. The corresponding values for an $M1(6^+ \rightarrow 6^+)$ transition are 0.39 and 1.60, respectively.

Due to de-orientation of recoiling ions [Bil86] (recoil-in-vacuum effect) and overlapping transition energies, information for the spin assignments from γ-ray angular distributions was difficult to obtain, especially at low spin.

3.3.1 Band I: Yrast band

The yrast $E2$ cascade in ^{186}Pb has recently been observed up to $I^\pi=14^+$, where the $I^\pi=12^+$ and $I^\pi=14^+$ states were tentatively assigned [Rev03]. In the present work, this cascade is confirmed up to $I^\pi=10^+$ and the 2710 keV level is assigned with $I^\pi=12^+$, as the 550 keV transition has the angular distribution ratio of a stretched $E2$. The $14^+ \rightarrow 12^+$ transition was measured to have an energy 4 keV higher than that reported in Reference [Bax93] and 10 keV higher than that reported in Reference [Rev03]. Moreover, the $\gamma\gamma$-coincidence data reveal candidates for the extension of the yrast band up to $I^\pi=20^+$ as shown in Figure 3.9.

In order to extend the yrast band, spectra of γ rays gated by the transitions of the top of the band were generated and are presented in Figure 3.9. The spectrum shown in Figure 3.9(a) was gated by the highest yrast-band transition of 550 keV observed firmly by Reviol *et al.* [Rev03]. In the inset the energy range between 640 and 690 keV is magnified. The known and the new yrast-band transitions have been marked with corresponding γ-ray energies.

Figure 3.9(b) shows a spectrum gated by the 668 keV transition. The known yrast-band transitions are clearly seen. In addition, the candidate transitions for the higher band members are in coincidence with the gating γ-ray transition with the exception of the 652 keV transition. The reason for non-observation of this γ ray is most likely due to the difficulties in background subtraction arising from the proximity of the $2_1^+ \rightarrow 0_1^+$ transition. This led to the use of a very narrow gate which resulted in poor statistics.

The lowest spectrum, Figure 3.9(c), shows the sum of gates on the 606, 652 and 668 keV transitions revealing the whole yrast cascade observed in the present work. The spin assignments for the two highest yrast-band levels were based on the assumption of the persistence of the rotational band and on the transition energies and intensities.

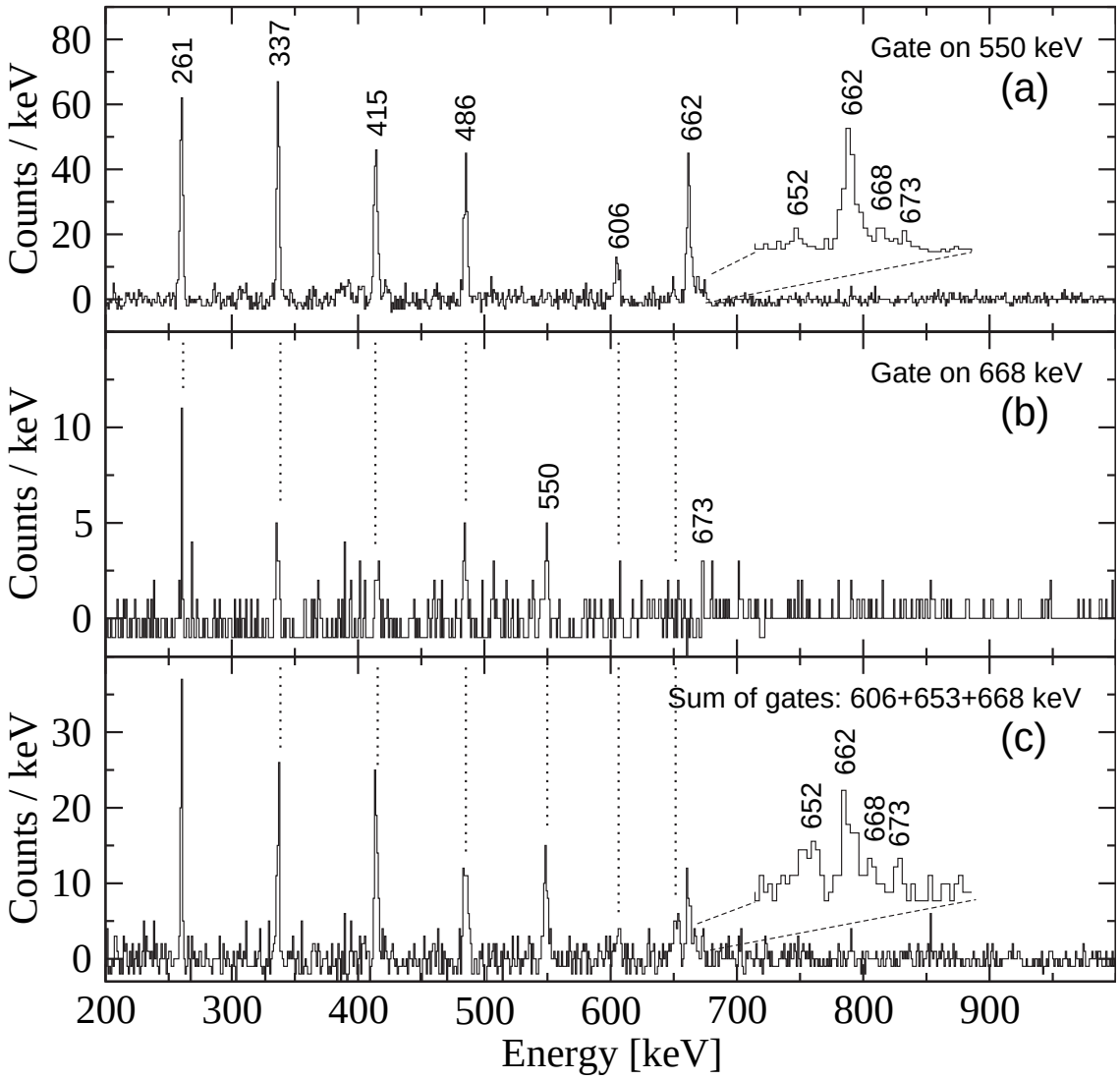

Figure 3.9: Recoil-gated α-tagged $\gamma\gamma$-coincidence spectra with gate on the (a) 550 keV transition, (b) 668 keV transition and (c) sum of gates on the 606, 652 and 668 keV transitions. Insets (a and b) show magnification of the energy range from 640 to 690 keV.

It is highly speculative, where the next transition would lie, but some candidates may be seen at 703 or 723 keV. In the inset, a part of the spectrum is again magnified.

3.3.2 Band II: Oblate band?

Figure 3.10(a) presents a recoil-gated, α-tagged $\gamma\gamma$-coincidence spectrum gated by the 945 keV transition. Since no coincidences with the yrast-band transitions can be seen, the gating transition must be above an isomeric state or feed the ground state. The

former is excluded by means of similar gates on the feeding transitions, which are in coincidence with the yrast-band transitions. Therefore, the transition is assigned to de-excite a (2_2^+) state at 945 keV. This interpretation is analogous to the ^{188}Pb case, where a similar 2_2^+ state exists at 953 keV [Dra03]. Unfortunately, due to the dominant high-energy $E2(2_2^+ \rightarrow 0_1^+)$ ground-state transition and some overlapping transitions, the $E2(2_2^+ \rightarrow 0_2^+)$ transition to the oblate 0^+ state as well as the possible branch to the prolate 0_3^+ state from the 2_2^+ state remain unobserved in ^{188}Pb and in ^{186}Pb. In addition, the $2_2^+ \rightarrow 2_1^+$ transition was not observed in ^{186}Pb. Our intensity limits still allow these transitions in ^{186}Pb to have $B(E2)$ values of 5, 25 and 30 times higher, respectively, than that for the $2_2^+ \rightarrow 0_1^+$ transition (Chapter 4). An I=3 assignment would enhance the $3_1 \rightarrow 2_1^+$ transition of 283 keV and the 945 keV transition would not be observed.

The 1337 keV level is tentatively assigned as $I^\pi = 4_2^+$ as it de-excites to the 2_1^+, 4_1^+ and 2_2^+ states. An I=3 assignment is unlikely as that would make the level highly non-yrast. Further support for this assignment comes from the de-excitation of the states lying above.

For similar reasons the 1738 keV level is tentatively assigned with $I^\pi = 6_2^+$. The assignment is consistent with the angular distribution information for the inter-band 479 keV transition allowing a non-stretched $E2$ character. Figure 3.10(b) shows a spectrum with a gate on the inter-band transition. It clearly shows the yrast-band transitions lying below together with the transitions associated with Band II lying above the gating transition in the level scheme. This transition plays a key role in the spin assignment as it provides strong evidence to assign the 1738 keV level with $I^\pi = 6_2^+$. Moreover, a different assignment would not satisfy the deduced branching ratios.

In addition to the $\gamma\gamma$-coincidence relations and intensities, the 8_2^+ assignment of the 2162 keV level is supported by the angular distribution information for the 424 keV transition. The spectrum in Figure 3.10(c) is gated with this transition and shows Band II transitions up to $I^\pi = 14^+$. Inter-band and yrast-band transitions are also seen.

Based on the $\gamma\gamma$-coincidence relations and intensity balance arguments, the 463, 508, and 551 keV transitions are assumed to form an $E2$ cascade feeding the 8_2^+ state and thus together with the 392, 401 and 424 keV transitions from a K=0 band of $E2$ transitions built on an oblate minimum (Section 4.3).

An attempt was made to obtain support for these assignments by means of a missing γ-ray intensity analysis. This was performed for Band II$\mapsto$Band I inter-band $I \rightarrow I$ transitions, where significant $E0$ components were expected. The importance of the $E0$ components is not only on the spin and parity assignment. A large $E0$ strength is a result of strong mixing of states with different shapes and by that means it is

also a sign of different deformations [Hey88]. Such a study was recently carried out by Dracoulis *et al.* [Dra03]. They reported dominant $E0$ components in several inter-band $I \rightarrow I$ transitions in ^{188}Pb.

The present coincidence data for ^{186}Pb do not indicate any strong $E0$ components in the corresponding inter-band transitions within the statistical error bars. The results are listed in Table 3.2. However, it should be noted that due to the higher energies of these transitions in ^{186}Pb (414.5, 478.8 and 487.4 keV) compared to ^{188}Pb (250.8, 352.6 and 431.7 keV, respectively), possible $E0$ components of similar monopole strength to those in ^{188}Pb may well be obscured by the much faster $E2$ components in ^{186}Pb. The

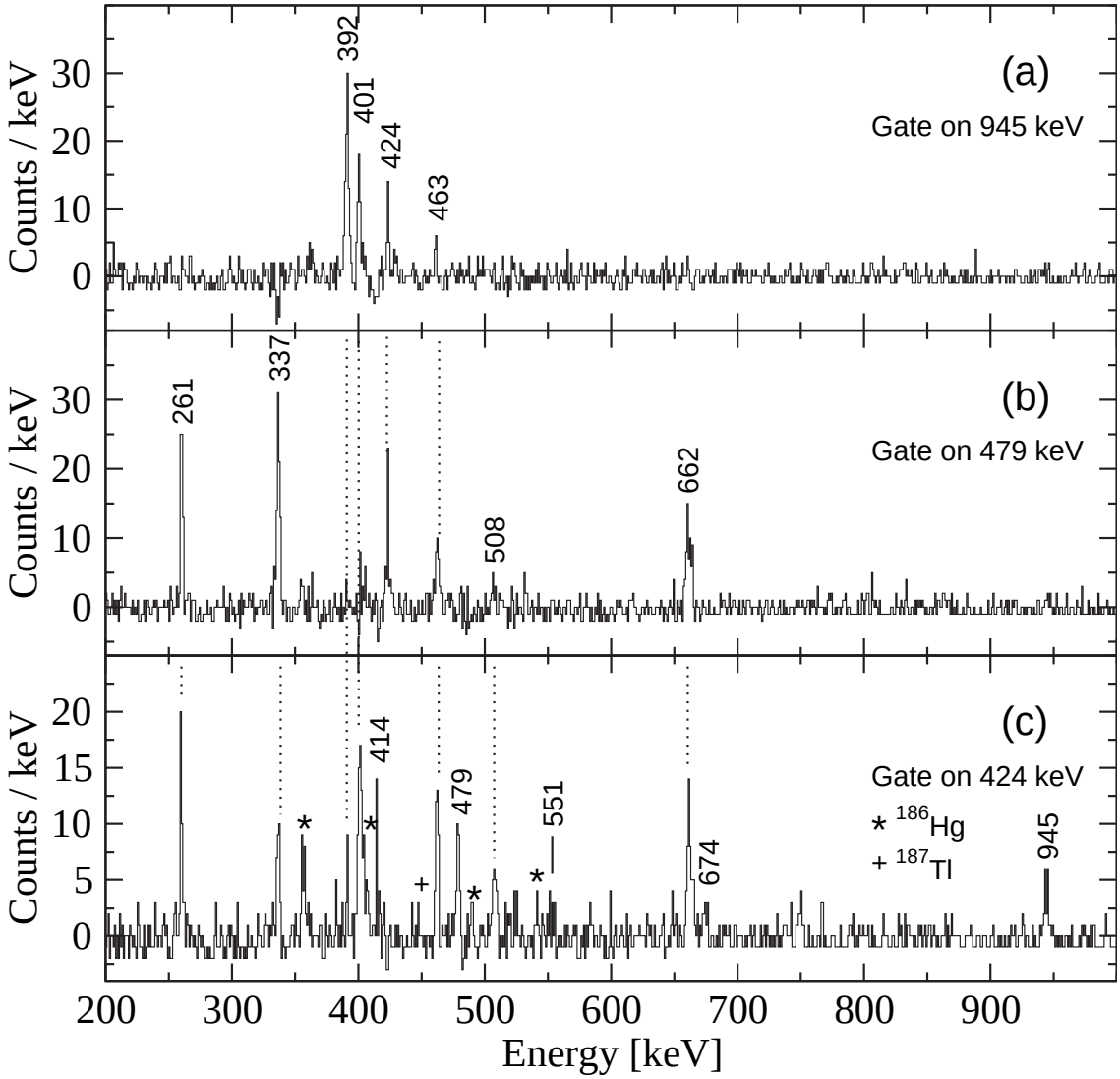

Figure 3.10: (a, b and c) Recoil-gated α-tagged $\gamma\gamma$-coincidence spectra with gates on the 945, 479 and 424 keV transitions, respectively. Contaminant transitions in the lowest spectrum originating from ^{186}Hg and ^{188}Tl nuclei have been marked.

$E0$ transition rate increases very slowly with increasing transition energy [Kan95], whereas the $E2$ transition rate is proportional to the fifth power of the transition energy. For example, assuming the same monopole strength for both ^{188}Pb and ^{186}Pb, it can be deduced that the $E0$ branch for the $6_2^+ \rightarrow 6_1^+$ transition is roughly 10% faster in ^{186}Pb than in ^{188}Pb, whereas the competing $E2$ transition is (479 keV/353 keV)^5=4.6 times more probable. When combined the gain in I($E0$)/I($E2$) ratio in ^{186}Pb is still 4 times smaller than in ^{188}Pb due to the higher transition energy in ^{186}Pb. The last column in Table 3.2 shows the estimated I($E0$)/I($E2$) ratios calculated from the corresponding ratios in ^{188}Pb by assuming the same monopole strength for the $E0$ transitions in both nuclei. They are in agreement with the ratios listed in the fifth column (note the large error bars).

Table 3.2: Comparison of the relative $E0$ intensities for inter-band transitions in ^{186}Pb (present work) and ^{188}Pb [Dra03]. The $E0$ intensities were deduced from the missing γ-ray intensities. The last column shows the I($E0$)/I($E2$) ratios calculated for ^{186}Pb by using the corresponding intensities in ^{188}Pb and by assuming the same monopole strength in both nuclei.

$I^{\pi}_{initial}$	$E_{transition}$ [keV]	I($E0$)$_{rel}$	I($E2$)$_{rel}$	I($E0$)/I($E2$)	I($E0$)/I($E2$) (from ^{188}Pb)
^{186}Pb					
4_2^+	414.5	12(6)	21(7)	0.6(7)	0.2(3)
6_2^+	478.8	5(4)	38(5)	0.2(2)	0.3(2)
8_2^+	487.4	32(17)	23(6)	1.4(1.5)	0.2(2)
^{188}Pb					
4_2^+	250.8	10(1)	6(1)	1.7(3)	
6_2^+	352.6	6(1)	5(1)	1.2(2)	
8_2^+	431.7	3.7(6)	15(2)	0.3	

It should be noted, that the yrast-band transitions had an isotropic γ-ray distribution up to level I^{π}=8^+, whereas for Band II and inter-band transitions the anisotropy was already observed above the 6_1^+ and 4_2^+ levels. This is at least partly due to the overlapping $8_1^+ \rightarrow 6_1^+$ and $4_2^+ \rightarrow 4_1^+$ transitions, the latter resulting in a negative angular distribution coefficient.

3.3.3 Band III: Octupole band?

The 2593 keV level de-excites mainly via the 918 keV transition. The γ-ray energy spectrum gated by this transition is shown in Figure 3.11(a). The spectrum reveals the yrast-band transitions below the 8_1^+ state suggesting that the gating transition feeds in above this state. In addition, the 369 and 420 keV transitions can be seen in coincidence. The 918 keV transition was placed into the level scheme as an inter-band transition connecting Band III with the yrast band. The initial 2593 keV level

is tentatively assigned with $I^{\pi}=9^{\pm}$ according to angular distribution information for the 918 keV transition. The angular distribution allows also an $I^{\pi}=8^{+}$ assignment, but that would be unlikely due to the non-observation of the $E2(8^{+}\rightarrow 6_1^{+})$ transition, which would be the dominant branch due to the energy factor. Further support for the level structure can be obtained from the coincidence relations shown in Figures 3.11(b) and (c).

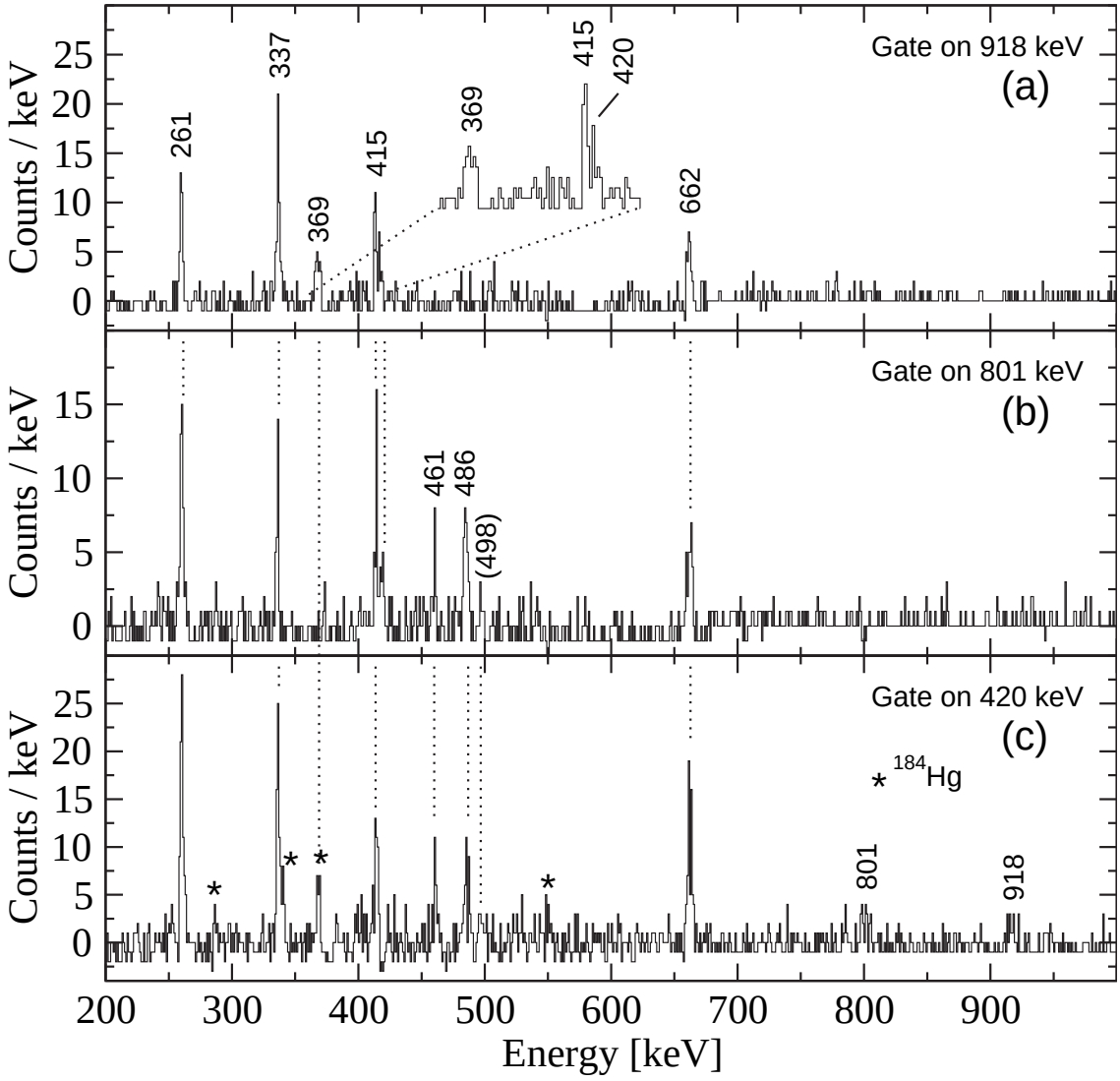

Figure 3.11: (a, b and c) Recoil-gated α-tagged $\gamma\gamma$-coincidence spectra with gates on the 918, 801 keV and 420 keV transitions, respectively. In the inset (a), energy range from 360 to 430 keV is magnified.

To illustrate the structure of Band III it would have been logical to show a spectrum gated by the 369 keV transition. Unfortunately, this transition overlaps with the $2_1^{+}\rightarrow 0_1^{+}$ transition in ^{184}Hg. Therefore, spectrum gated by the 801 keV inter-band transition is shown in Figure 3.11(b). It presents the yrast band transitions up to$I^{\pi}=10_1^{+}$

together with the 420, 461 and 498 keV transitions. Thus the initial state de-exciting by the 801 keV transition lies at 2962 keV matching with the sum of 2593+369 keV.

The third spectrum, Figure 3.11(c), is gated by the 420 keV transition. This transition overlaps with the $8_1^+ \rightarrow 6_1^+$ transition in ^{184}Hg, but was chosen as it shows all the observed transitions firmly associated with Band III. Contaminant transitions originating from ^{184}Hg were easily identified. The contribution of the overlapping $2_1^+ \rightarrow 0_1^+$ transition of 368 keV in ^{184}Hg in the 369 keV peak can be approximated to be minimal by assuming that the contribution is the same as for the $4_1^+ \rightarrow 2_1^+$ transition of 285 keV.

Based on the $\gamma\gamma$-coincidence relations, intensities and angular distribution information for the $9_1 \rightarrow 8_1^+$ transition, the 369, 420, 461, 498 keV transitions are assumed to form an odd spin band of $E2$ transitions.

3.3.4 Band IV: Odd spin candidates for a γ band?

The Band IV members were placed into the level scheme on the basis of$\gamma\gamma$-coincidence relations and energy sum arguments. The inter-band transitions from this band to Band I were weak and no reasonable angular distribution information could be extracted for these transitions. The tentative assignments were based on intensity balance and sum energy arguments and level systematics of neighboring nuclei.

The energy spectra presented in Figure 3.12 reveal a weak band structure at relatively low excitation energies. The topmost spectrum is gated by the 362 keV transition, which is one of the decay out transitions of the lowest observed state at 1307 keV. The transition feeds the 2_2^+ state as the 945 keV transition is seen in coincidence. The absence of the feeding 337 keV transition is most probably due to poor statistics and problems in background subtraction as its energy overlaps that of the yrast $6_1^+ \rightarrow 4_1^+$ transition. The gating 362 keV transition can be seen in the spectrum shown in Figure 3.10(a) (not marked) confirming the coincidence with the 945 keV transition.

Figure 3.12(b) shows the γ-ray energy spectrum gated by the 790 keV inter-band transition assumed to feed the yrast 6^+ state, the initial state lying at 2049 keV. In the spectrum, the lowest yrast-band transitions are present together with the feeding 470 keV transition.

The third gate was set on the 470 keV transition, resulting in the spectrum shown in Figure 3.12(c). It presents both inter-band and intra-band transitions associated with Band IV.

The construction of Band IV was very difficult due to several overlapping transition energies both in ^{186}Pb and in ^{186}Hg. The total projection of the $\gamma\gamma$ matrix shows peaks

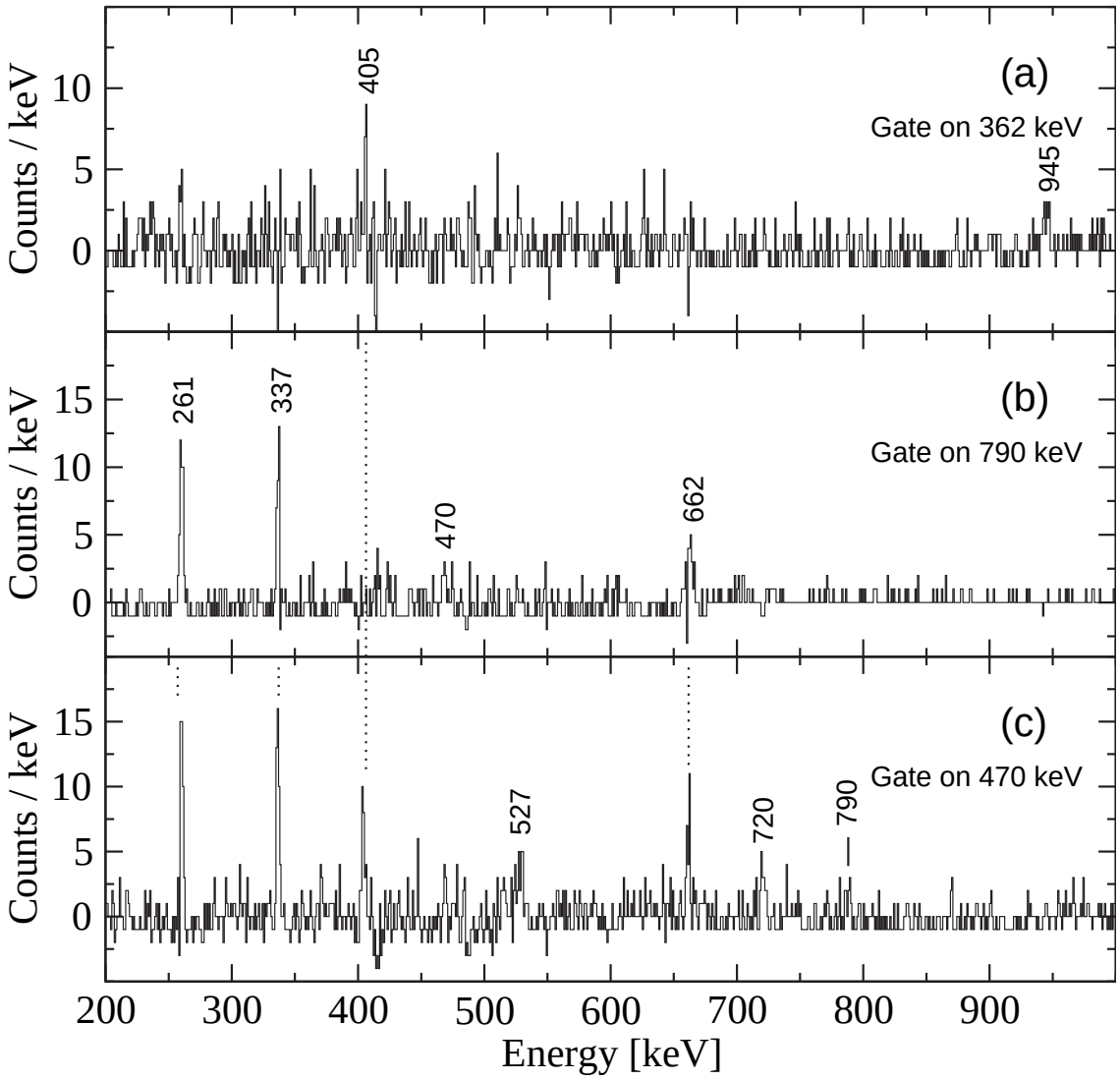

Figure 3.12: (a, b and c) Recoil-gated α-tagged $\gamma\gamma$-coincidence spectra with gates on the 362, 790 and 470 keV transitions, respectively.

at 644 and 385 keV (Figure 3.13), which is in accordance with the energy sum balance associated with Band IV. Partial support from $\gamma\gamma$-coincidence data encouraged association with Band IV. However, due to the insufficient statistics only tentative placement in the level scheme could be made.

3.3.5 Other transitions

The recoil-gated α-tagged $\gamma\gamma$-coincidence data includes several transitions, which could not be placed into the level scheme due to insufficient coincidence data. Such

transitions have been marked in Figure 3.13 and listed in Table 3.1. Figure 3.13 shows the recoil-gated α-tagged singles γ-ray spectrum and the total projection of recoil-gated α-tagged $\gamma\gamma$-coincidence matrix. If these transitions were obtained from random recoil-α correlations, they should originate from contaminant ^{186}Hg, ^{184}Hg, ^{187}Tl or ^{186}Tl nuclei produced via the most dominant reaction channels. The 385 and 644 keV transitions can be associated with nuclei mentioned above, but they also coincide with transitions associated with ^{186}Pb, whereas other marked transitions have not been observed in the contaminant nuclei.

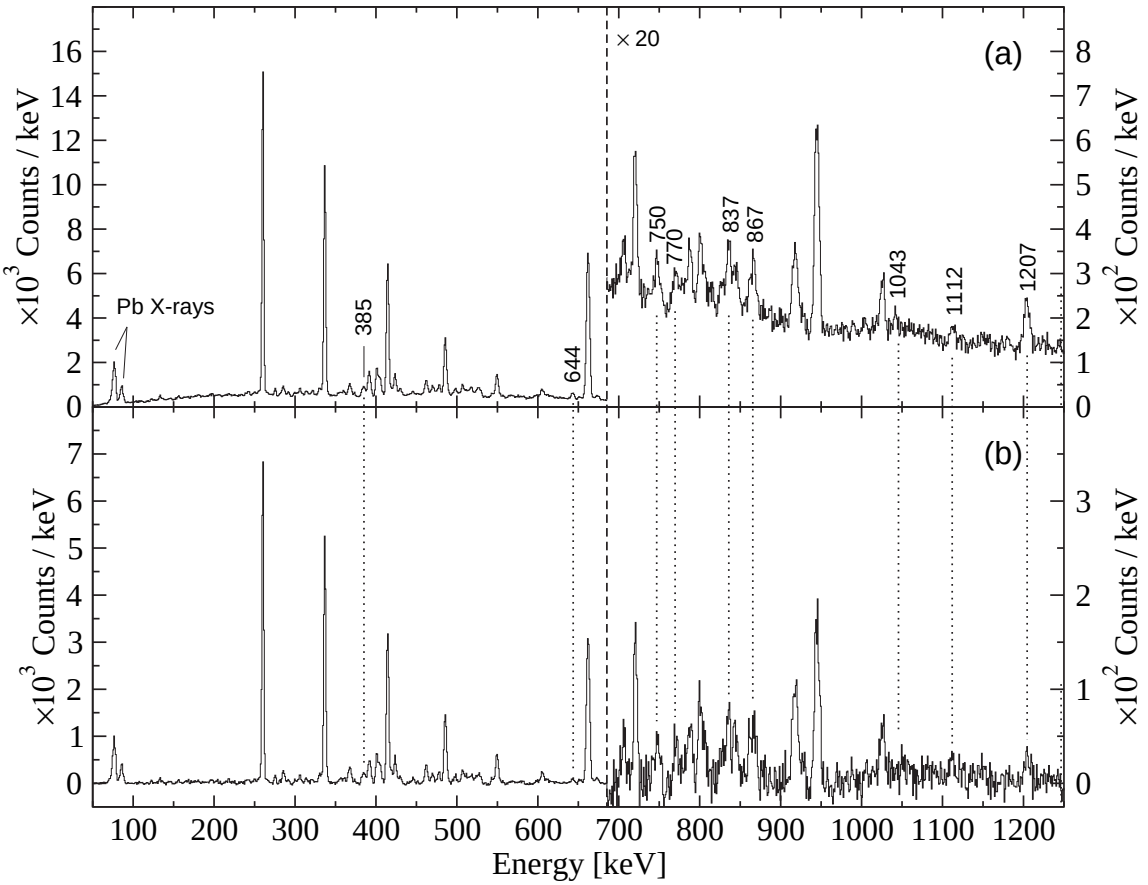

Figure 3.13: The transitions that could not be located into the level scheme. (a) Recoil-gated α-tagged singles γ-ray spectrum (b) Total projection of the background subtracted recoil-gated α-tagged $\gamma\gamma$ matrix.

If a transition is associated with ^{186}Pb, but does not show any coincidences with the yrast-band transitions, it most likely feeds the ground state or takes place above an isomeric state. For example, the 1207 keV transition could be associated with a (1^-) state at 1219 keV analogous to that in ^{188}Pb [Dra04].

3.3.6 Delayed γ rays

The performance of the planar Ge detector at the focal plane was poor in the present experiment. Thus, the only reliable information on the delayed γ rays was obtained with two Phase I detectors mounted at the focal plane. Figure 3.14 shows a recoil-gated α-tagged singles delayed γ-ray spectrum. An event was incremented into the spectrum if it was detected within a 1 s time window after the observation of a recoil, whereas it was subtracted as a background event if the detection took place within a 1 s time window before the implantation of the recoil. No clear evidence of isomers or yrast-band transitions is seen in the spectrum.

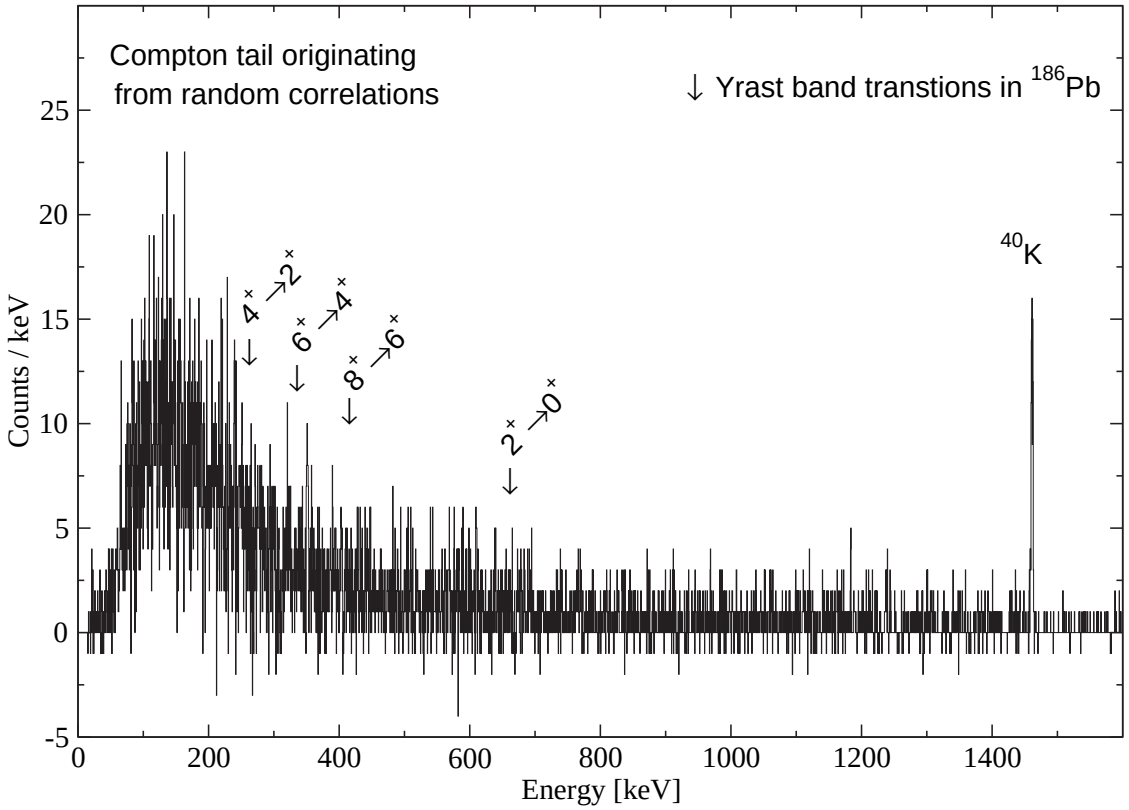

Figure 3.14: Delayed γ rays detected with two Phase I Ge detectors at the focal plane of RITU. The energies of the expected yrast-band transitions in ^{186}Pb are marked. The only clear peak at 1459 keV originates from ^{40}K in the concrete walls of the measurement cave.

4 Discussion

The present data reveal three new bands in ^{186}Pb. They incorporate 24 new levels and 39 new transitions. The bands have been tentatively named after intrinsic structures. Supporting arguments for these assignments are given in this chapter, along with discussion of the properties of the bands.

4.1 Intruder structures in the even-even Pb isotopes

In even-even nuclei, especially in the vicinity of the closed nucleon shells, the low-lying nuclear excitations are in most cases generated by breaking a nucleon pair. The picture changes when moving towards the mid-shell nuclei, where a subtle rearrangement of a few nucleons in the orbitals close to the Fermi surface may result in a macroscopic shape change. In the Pb region, 0^+ states come down to energies close to the spherical ground state in the vicinity of neutron mid-shell at N=104. [Dup84, Dup85, Bij96, And00, And99b]. These 0^+ states are generally associated with intruder $2p$-$2h$ and $4p$-$4h$ ($6p$-$6h$) proton excitations across the Z=82 energy gap [May77, Ben89, Hey91, Woo92, Naz93]. Thus, the neutron-deficient even-even Pb nuclei provide a fertile ground for the shape-coexistence phenomenon. More evidence for the preceding interpretation comes, for example, from the low-lying rotational and vibrational bands. These so-called intruder states are best described and reproduced by three theoretical approaches: 1) shell model with a residual proton-neutron force, 2) deformed mean-field descriptions and 3) Interacting Boson Model (IBM). These approaches have been discussed in details in References [Woo92, Hey92] and references therein.

Figure 4.1 shows the level systematics of the even-even Pb isotopes below the neutron N=126 closure. A systematic lowering of the first excited 0^+ state with decreasing neutron number is apparent. In heavier Pb nuclei, these states are associated with a mainly oblate structure. Evidence for an oblate structure comes, for example, from a low-spin sequence of non-yrast states in ^{196}Pb. These states are also described as $\pi(2p$-$2h)$ shell-model intruder excitations [Pen87]. Below ^{194}Pb the 0^+ intruder state becomes even the first excited state. However, ^{188}Pb is so far the only Pb isotope where a well-developed non-yrast collective band has been observed that may well be indicative of the oblate minimum [Dra04]. The systematics for candidate oblate band members in ^{186}Pb and ^{188}Pb follow the behaviour predicted by theory [Rod04].

The identification of the 650 keV 0_3^+ state in ^{186}Pb represents the only firm observation of a prolate intruder 0^+ state in Pb isotopes [And00], whereas prolate bands have been identified in five even-even $^{182-190}$Pb isotopes [Jen00, Coc98, Bax93, Hee93, Dra98]. In the decay of these bands the 0^+ band head is bypassed due to the competing high-energy $E2$ transition from the 2^+ band member to the spherical ground state. Prolate yrast bands, very similar to those in these Pb isotopes, have also been observed in even-mass Hg and Pt isotopes with $100 \leq N \leq 108$ [Jul01, Woo92], and recently in ^{190}Po [Vel03]. Yrast bands, associated with oblate intruder structures, have been observed in ^{192}Po, ^{194}Po and ^{198}Rn [Jul01].

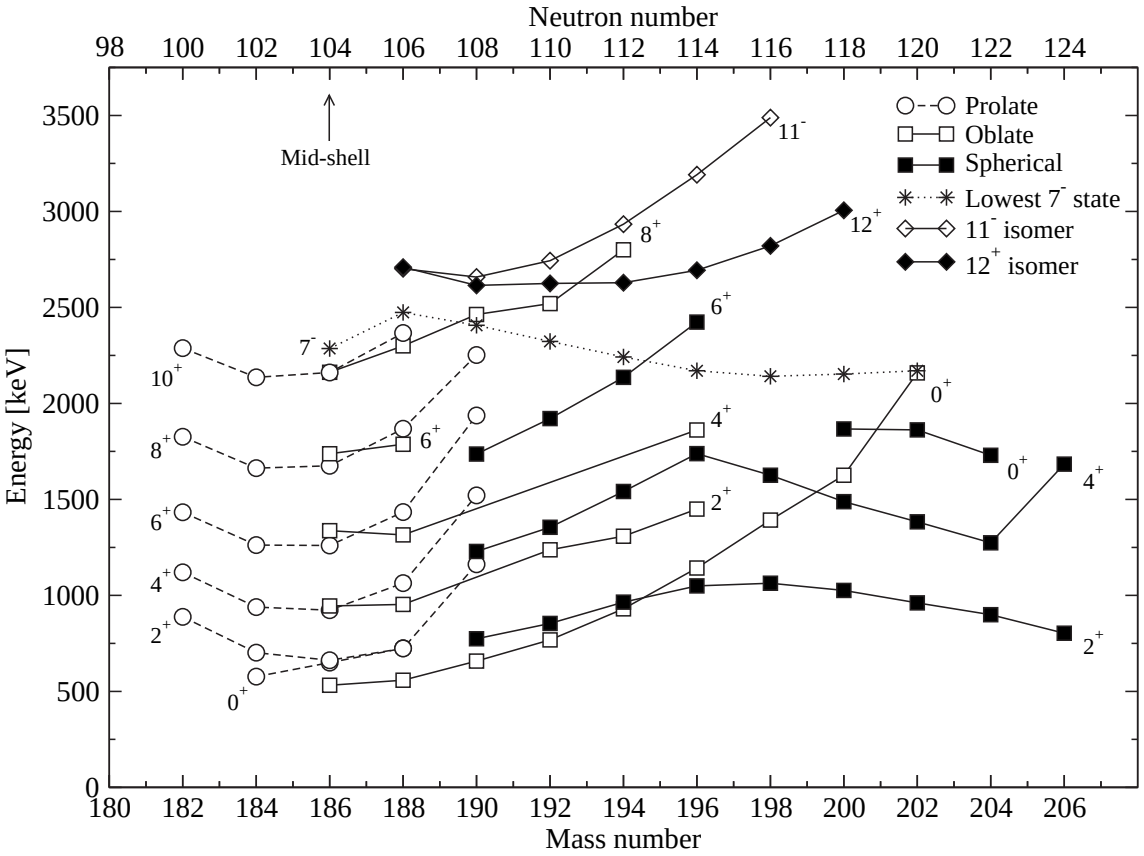

Figure 4.1: Level systematics for even-even Pb isotopes. Data are taken from the present work, References [Jul01, Dra04, Dra98, Nab97, Fan91, Bal96, Gör01, Don78, Jai02, Sch80, Ste83, Sun89, Ste85, Ruy86] and references therein.

4.2 Prolate yrast band

In contrast to the heavier Pb isotopes, well-developed prolate minima were predicted to occur in Pb isotopes with $N \leq 108$ through calculations carried out in the framework of the Strutinsky shell-correction method with a Woods-Saxon potential and a

monopole pairing interaction [May77, Dup90]. However, the first direct experimental evidence for prolate deformation in the light Pb isotopes was provided by Heese*et al.* [Hee93]. They observed collective yrast bands in ^{186}Pb and ^{188}Pb by using in-beam γ-ray spectroscopy. They associated the bands with prolate shape on the basis of similarities with rotational yrast bands in the Hg isotones. The results for ^{186}Pb were confirmed by Baxter *et al.* [Bax93]. Indeed, the similarities are striking as will be described below. Later on, Andreyev *et al.* [And00] determined the first two excited states in ^{186}Pb to be 0^+ states. On the basis of α-decay hindrance factors, the 532 keV 0_2^+ state was associated with a $\pi(2p\text{-}2h)$ configuration, whereas the 650 keV 0_3^+ state was associated with a $\pi(4p\text{-}4h)$ configuration. In the deformation picture, these states are usually associated with an oblate and prolate shape, respectively. The latter is assumed to be the band head of the collective yrast band.

The latest in-beam results for ^{186}Pb (excluding the present work) were reported by Reviol *et al.* [Rev03]. However, they could only confirm earlier results and propose four new transitions, two of them not being confirmed in the present work.

The rotation of a deformed nucleus gives rise to collective nuclear excitations. The relation between the transition energy (E_γ) and the kinematic moment of inertia ($\mathcal{J}^{(1)}$) can be derived from the angular velocity ($\omega(I)$) and the excitation energy ($E(I)$). For a ΔI=2 and K=0 band the relation can be expressed as

$$\begin{aligned} \omega(I) = \frac{dE(I)}{dI}, \quad E(I) &= \frac{\hbar^2}{2\mathcal{J}^{(1)}} I(I+1) \\ \Rightarrow \quad \mathcal{J}^{(1)} &= \frac{2I-1}{E_\gamma}\hbar^2, \end{aligned} \tag{4.1}$$

where I is the total angular momentum. In Figure 4.2, the kinematic moments of inertia as a function of γ-ray energy are plotted for the yrast bands in the isotones ^{182}Pt, ^{184}Hg and ^{186}Pb (circles) and for some of their neighboring nuclei. The yrast band levels in the N=104 isotones of Pt, Hg and Pb normalized to the energy of the 6^+ states are shown as an inset. The curves reveal a smooth increase with increasing γ-ray energy (or rotational frequency) up to $I^\pi \approx 16^+$ indicating considerable softness of these nuclei. The increase may also result or have a small contribution arising from a shape change. The kinematic moment of inertia for a deformed rigid rotor (to first order in β) can be classically expressed as

$$\mathcal{J}^{(1)} = \frac{2}{5} A u R_0^2 (1 + 0.31\beta), \tag{4.2}$$

where A is the mass number, u is the atomic mass unit, R_0 is the nuclear radius and β is the deformation parameter [Ald56]. By using a typical deformation parameter

value β=0.27, deduced for prolate minima in the light Pb region, Equation 4.2 gives $\mathcal{J}^{(1)}\approx 90\hbar^2/\mathrm{MeV}$ for ^{186}Pb. The value is significantly higher than the ones shown in Figure 4.2. It is also remarkable, that even for such a notable deformation, the contribution of the deformation (β) in the kinematic moment of inertia is only about 10%.

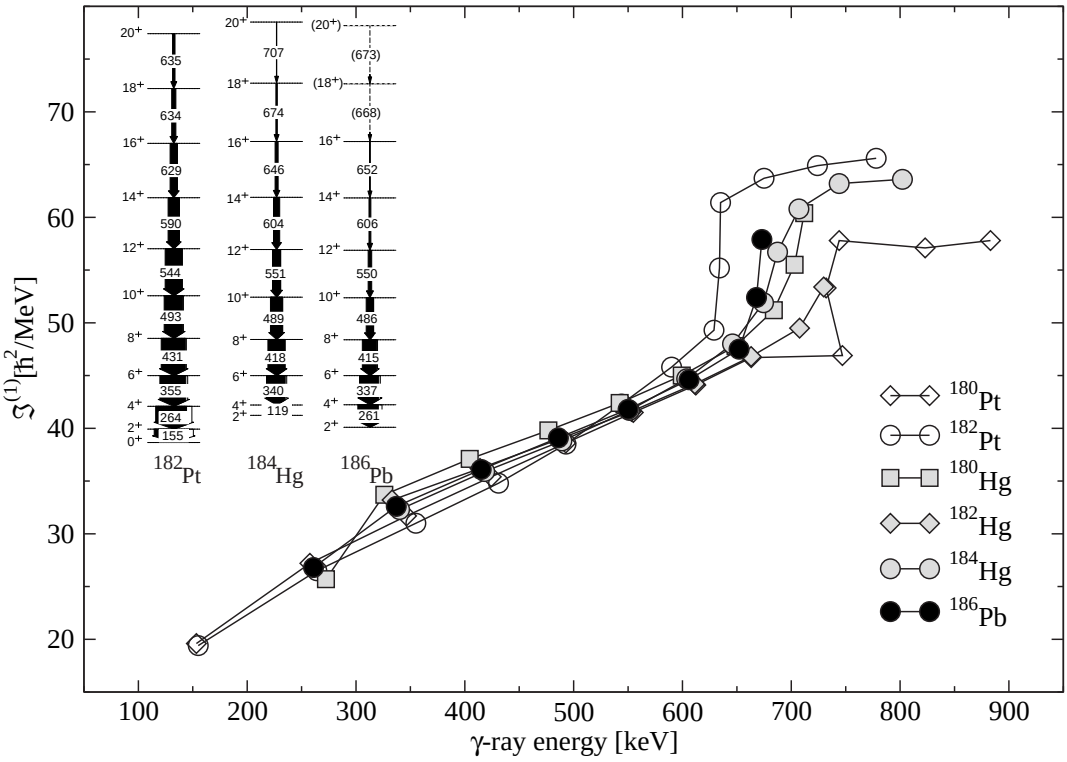

Figure 4.2: Kinematic moment of inertia $\mathcal{J}^{(1)}$ as a function of γ-ray energy for the collective bands in ^{186}Pb, ^{182}Pt and in $^{180-184}$Hg. The inset shows the yrast band levels in N=104 Pb, Hg and Pt isotones lined up with the 6^+ state. The data for ^{186}Pb are taken from the present work and for the other nuclei from the References [Kon00b, Bin95, Ma86].

A sudden increase in the kinematic moment of inertia values can be seen at spin around 16^+. This upbend in ^{186}Pb has been tentatively observed in the present work for the first time. Overall, the kinematic moment of inertia for the yrast band in^{186}Pb follows the one for the corresponding band in ^{184}Hg remarkably well. In the corresponding bands in Hg and Pt nuclei, the upbend has been associated with a rotational alignment of $\nu(\mathrm{i}_{13/2})^2$ or $\pi(\mathrm{h}_{9/2})^2$ according to cranked shell-model calculations.

The properties of these yrast bands are further considered in Figure 4.3, where the aligned angular momenta (i_x) are plotted as a function of rotational frequency. The aligned angular momentum is a measure of the difference between the projection of the angular momentum to the rotation axis ($I_x(I)$) and the calculated angular momentum for a smoothly-behaving reference rotational nucleus. (ωJ_{Ref}). It provides information

on the quasiparticle alignment as a function of spin (I) and can be written as

$$i_x(I) = I_x(I) - \omega J_{Ref} = \sqrt{I(I+1) - K^2} - \omega[J_0 + J_1\omega^2], \tag{4.3}$$

where J_{Ref}=$J_0 + J_1\omega^2$ is a so-called Harris formula [Har65]. The Harris parameters J_0 and J_1 used for all the plots in Figure 4.3 were extracted from the unperturbed yrast band states in ^{184}Hg.

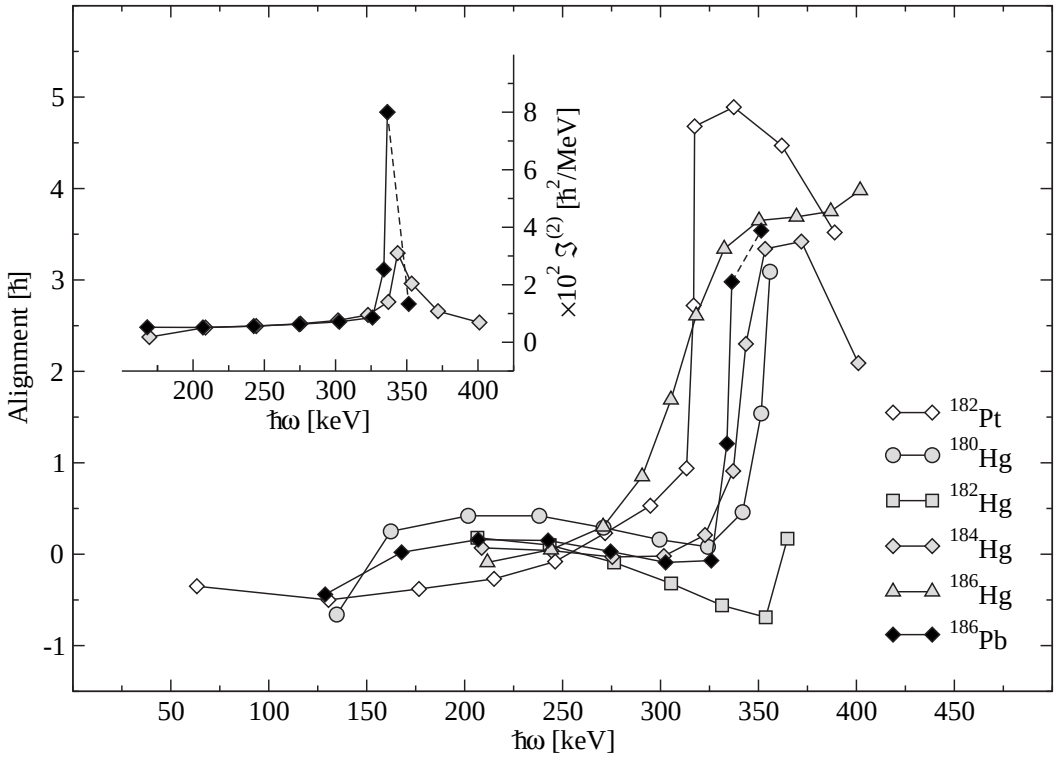

Figure 4.3: Aligned angular momenta of the yrast band in ^{186}Pb and of the corresponding prolate bands in Pt and Hg nuclei close to the neutron mid-shell as a function of rotational frequency. In all cases, a common reference was subtracted with Harris parameters $\mathcal{J}_0$=27.1$\hbar^2/MeV$, $\mathcal{J}_1$=194.7$\hbar^4/MeV^3$. The dynamic moments of inertia for these bands in ^{186}Pb and ^{184}Hg are shown as an inset. Data for ^{186}Pb are taken from the present work and for the other nuclei from the References [Pop97, Kon00b, Bin95, Den95, Ma93].

The inset in Figure 4.3 shows a comparison of the dynamic moment of inertia between the yrast bands ^{184}Hg and ^{186}Pb. The dynamic moment of inertia ($\mathcal{J}^{(2)}$) is the inverse second derivative of $E(I)$ with respect to I. Thus, again for ΔI=2, K=0 band $\mathcal{J}^{(2)}$ can be obtained as

$$\mathcal{J}^{(2)} = \left[\frac{d^2E(I)}{dI^2}\right]^{-1} = \left[\frac{d\omega(I)}{dI}\right]^{-1} = \frac{\Delta I}{\Delta E_\gamma(I)/2\hbar} = \frac{4\hbar^2}{\Delta E_\gamma(I)}, \tag{4.4}$$

where $\Delta E_\gamma(I)$ is the energy difference between two sequential γ-ray transitions. As $\mathcal{J}^{(2)}$ is sensitive to the changes in the transition energy (rotational frequency), it can be used to extract information about the crossing frequencies.

The plots in Figure 4.3 reveal quite similar alignment in ^{186}Pb than in the isotones ^{182}Pt and ^{184}Hg. A crossing frequency of $\hbar\omega\approx$0.33 MeV for ^{186}Pb can be deduced from Figure 4.3. If it is assumed that the $22^+\rightarrow 20^+$ transition has an energy of 703 keV, an alignment gain of $4\hbar$ can be deduced. However, this is strictly a speculative guess.

According to theoretical quasiparticle Routhians, a proton alignment would give rise to more drastic backbending phenomena and take place at a crossing frequency of $\hbar\omega\approx$0.31 MeV, whereas the alignment of a neutron pair would take place at a slightly lower crossing frequency of $\hbar\omega\approx$0.27 MeV with higher interaction strength. The former is in better agreement with the measured crossing frequency, the latter supporting a smoother neutron alignment. In lighter $N\approx$104 nuclei this alignment is attributed to $\nu(\mathrm{i}_{13/2})^2$. Due to these contradictions, the origin of the alignment remains unclear. The alignment has been widely discussed in various articles [Voi90, Ma86, Jan83, Bax93].

4.3 Association of a quadrupole non-yrast band with an oblate shape

The observation of non-yrast bands is an important step towards understanding of the structure of light Pb nuclei. This section provides several arguments to associate Band II with an oblate shape.

Remarkable features of Band II are the strong $I\rightarrow I$ and weak $I\rightarrow I-2$ inter-band transitions to the prolate yrast band as shown in Figure 4.4. The observed 674 keV branch from the 4_2^+ to the 2_1^+ state represents only about 3% of the $B(E2)$ value of the 392 keV intra-band transition. The non-observation of the other $I\rightarrow I-2$ inter-band transitions allows intensity limits to be set. The upper limit for their $B(E2)$ values is determined to be 3% of that of the competing intra-band transitions.

If Band II was a quasi-β band based on the prolate minimum, the competing $I\rightarrow I-2$ and $I\rightarrow I$ $E2$ branches from Band II to Band I should, according to the Alaga rules [Ala55], have similar $B(E2)$ values. Therefore, the $I\rightarrow I-2$ transitions having the highest energy, should be the dominant ones. This is clearly not that what was observed. Similar arguments make a γ band an unlikely explanation for Band II. A possible candidate for a γ band is discussed in Section 4.5.

The observed intensities for the $I\rightarrow I$ inter-band transitions from the 4_2^+, 6_2^+ and 8_2^+ states represent $B(E2)$ values, which are 20-60% of those of the competing intra-band

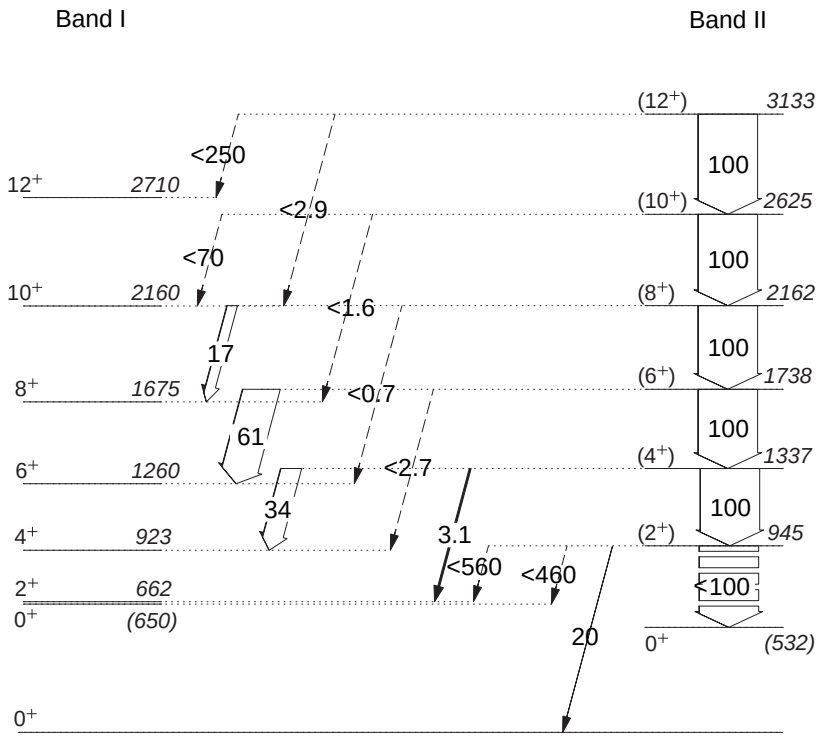

Figure 4.4: Relative $B(E2)$ values deduced for Band II from the present data. The $B(E2)$ values have been normalized to 100 for the corresponding intra-band transition. The width of the arrows are related to the $B(E2)$ values, whereas the transitions with deduced $B(E2)$ upper limits are shown with dashed arrows.

transitions (ΔI=0 $M1$-transitions between K=0 bands are forbidden). The deduced intensity limits for the similar $I \rightarrow I$ transitions from the higher-lying states of Band II do not rule out the existence of $E2$ transitions of a similar strength. As pointed out by Dracoulis *et al.* [Dra03], the strong $I \rightarrow I$ inter-band transitions may be due to mixing of two different shapes.

Further support for association of Band II with $2p$-$2h$ structure can be found in mixing calculations carried out in the framework of the IBM. Starting from the parameters determined in Reference [Fos03], a calculation including both proton $2p$-$2h$ and $4p$-$4h$ excitations across the Z=82 shell gap has been carried out by Hellemans *et al.* [Hel04] (similar to the study of ^{188}Pb [Hel05]). Effective charges were fitted to the two measured $B(E2)$ values in ^{188}Pb [Dew03]. The calculated $E2$ decays (shown in Figure 4.5), starting from the higher spin states, allow the construction of two collective bands. The energies of the bands are in reasonable agreement with the experimental values. The mixing amplitudes of the 0_2^+ and the 0_3^+ states are similar to the results derived by Page *et al.* [Pag01] although the mixing is somewhat more pronounced. Moreover, the calculated $I \rightarrow I-2$ inter-band transitions are considerably weaker than the strong $I \rightarrow I$ inter-band transitions, which is consistent with the observed $E2$ branching.

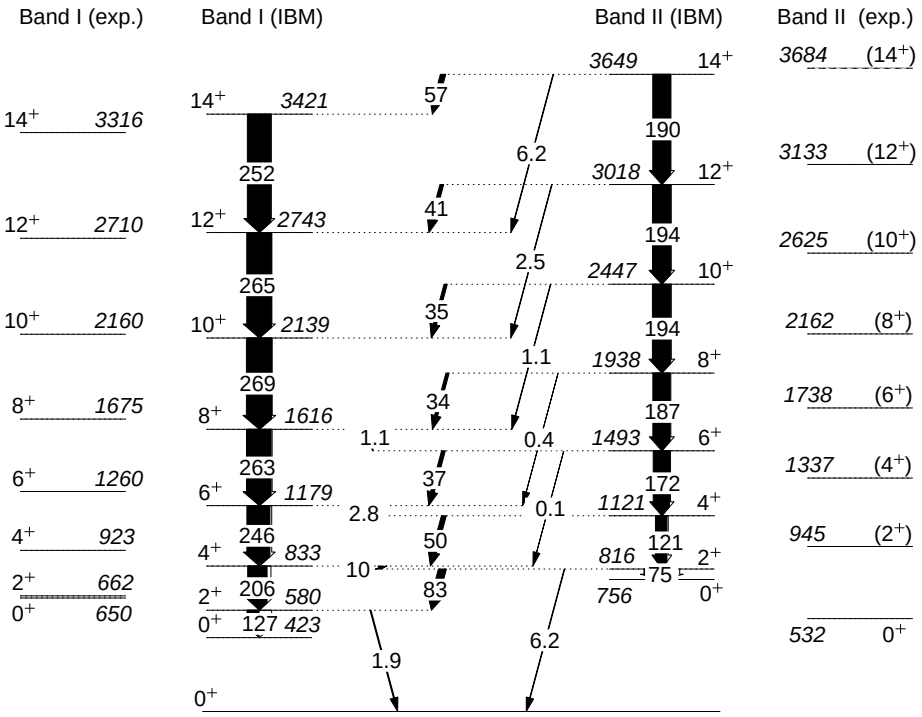

Figure 4.5: Theoretical level scheme of ^{186}Pb deduced in the framework of the IBM [Hel04]. The arrows denote the $B(E2)$-values for a given transition, expressed in W.u.

The IBM quadrupole moment was also equated with the quadrupole moment for K=0 bands within the collective rotational model by Hellemans *et al.* [Hel04]. Thus extracting intrinsic quadrupole moments, a positive sign for the intrinsic quadrupole moments of the band corresponding to the experimental yrast band was found, indicating a prolate deformation. For the non-yrast band, a negative sign indicative of oblate deformation was deduced.

The kinematic moments of inertia ($\mathcal{J}^{(1)}$) for Band II in ^{186}Pb together with oblate bands in ^{182}Pt, ^{188}Pb, ^{192,194}Po and ^{196}Pb are plotted in Figure 4.6. For comparison, the values of $\mathcal{J}^{(1)}$ for the prolate bands in ^{184,186}Pb are also shown (open symbols). In general, the kinematic moment of inertia values for the prolate bands are higher than those for corresponding oblate bands, which is not explained solely by Equation 4.2. The $\mathcal{J}^{(1)}$ values for the ^{192,194}Po nuclei plotted as representatives of well behaving oblate rotational bands (grey symbols) are lower than those for the prolate bands, but still increase smoothly with increasing rotational frequency (γ-ray energy). The $\mathcal{J}^{(1)}$ curve for Band II in ^{186}Pb differs both from the known prolate and the well behaving oblate bands.

Similarities in the kinematic moments of inertia plots can be found between the candidate oblate bands in ^{182}Pt, ^{186}Pb and ^{188}Pb nuclei (black symbols). They extend from

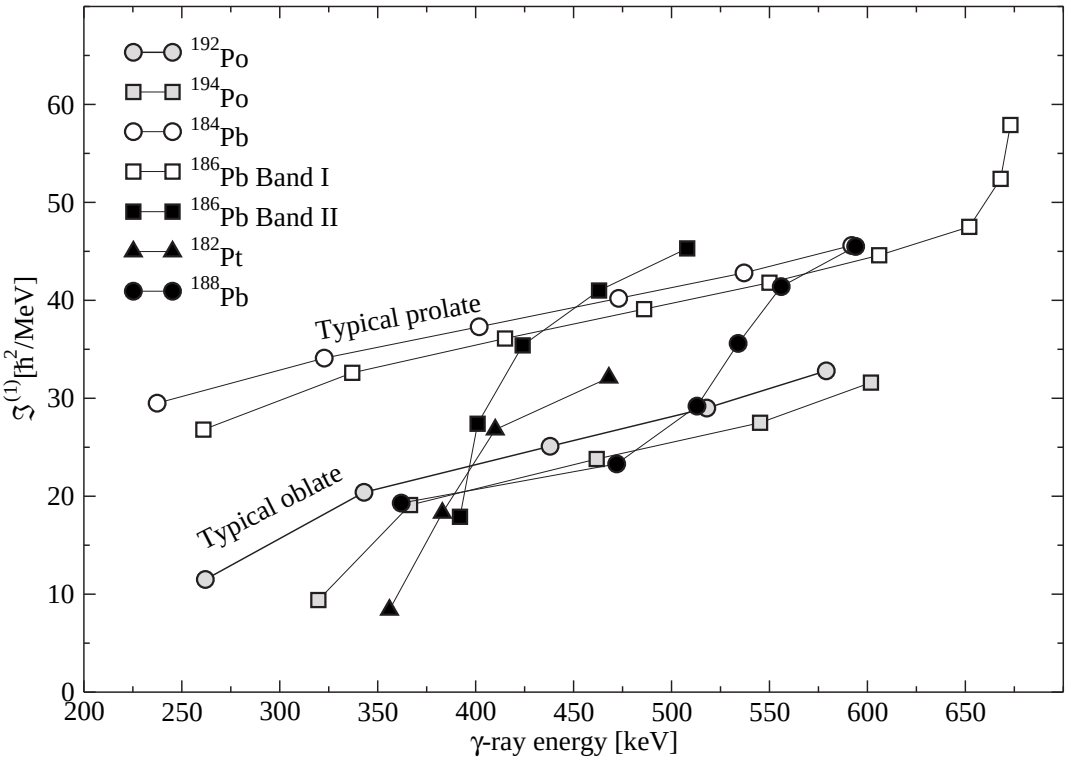

Figure 4.6: Kinematic moment of inertia $\mathcal{J}^{(1)}$ as a function of γ-ray energy for Band I and Band II together with those for known oblate bands in nuclei close to ^{186}Pb. Data for ^{186}Pb are taken from the present work and for the other nuclei from the References [Pop97, Dra04, Hel99, Hug93].

small $\mathcal{J}^{(1)}$ values at low spin to values which are higher than those for the well behaving oblate bands or even higher than those for the prolate bands as shown in Figure 4.6. It is difficult to associate these upbends with any alignment of valence nucleons as they occur at such low spin (see for example Section 4.2 and References therein). One explanation would be a shape change towards a more deformed oblate structure. Highly deformed oblate structures are predicted to occur at relatively low excitation energy in the even-even Pb isotopes close to the neutron mid-shell [Naz93, Ben04, Rod04].

Similar bands in even-even Pt isotopes close to N=104 were interpreted as quasi-β bands [Voi90, Hus76, Fin72]. Those bands were associated with collective vibrations on the basis of the strong $E0$ admixtures in $I \rightarrow I$ transitions, which is a possible signature of β-vibrational states. De Voigt *et al.* associated the band in ^{180}Pt with a quasi-β band even though the branching ratios were in disagreement with the Alaga rules [Voi90].

As pointed out earlier, the mixing of different shapes in heavy nuclei may result in considerable $E0$ components in $I \rightarrow I$ transitions [Hey88]. This argument was used by Popescu *et al.* [Pop97] and Hebbinghaus *et al.*[Heb90] as they both associated the

bands above the 0_2^+ state in ^{182}Pt and in ^{186}Pt, respectively, with an oblate shape. A similar study for ^{188}Pb was recently carried out by Dracoulis *et al.*

4.4 Candidate for an octupole band

As discussed in Section 3.3.3, a firm spin assignment of the Band III members could not be done. The 306 keV transition could not be properly associated with Band III and the band head state is somewhat unclear. Nevertheless, in the following it is assumed that the 2287 keV state belongs to Band III and is assigned as $I^\pi = 7^-$. The possible origin of this band is discussed below.

Negative parity bands have been observed in several even-even Os, Pt and Hg isotopes in the vicinity of the neutron mid-shell. However, there is no consensus regarding their origin. It has been proposed that these structures in $^{176-180}$Os, $^{176-180}$Pt and in $^{178-180}$Hg are built on a single-phonon octupole vibration, crossed by two-quasiparticle excitations at higher frequencies [Dra82, Ced90, Kon00a, Voi90, Kon00b]. In contrast, pure two-quasiparticle assignments for low-lying negative parity structures in ^{184}Hg, ^{182}Pt, and ^{180}Os have also been proposed [Den95, Pop97, Lie99]. The intrinsic structures of negative parity bands in ^{182}Hg and ^{186}Hg remain unclear. Due to the similarity with these bands in the light Os, Pt and Hg isotopes, Band III is associated with negative parity.

The kinematic moment of inertia values for Band I and Band III together with yrast and 5^- bands in ^{182}Pt are plotted in Figure 4.7. The inset shows the aligned angular momentum as a function of rotational frequency. The kinematic moment of inertia values for the negative parity bands follow those for the corresponding yrast bands, albeit approximately $25\hbar^2$/MeV higher in the kinematic moment of inertia. Gradual increase with increasing rotational frequency (γ-ray energy) indicates softness or a shape change of the nucleus as discussed in Section 4.2. The aligned angular momentum values start from approximately $3\hbar$, which is typical for octupole bands. ^{182}Pt is chosen as a reference nucleus since: a) it is an isotone of ^{186}Pb, b) it is rather well studied and c) it is a good representative of nuclei with corresponding negative parity bands in this region.

The similar underlying structure of Band III to the 5^- band in ^{182}Pt is further supported by similar decay pattern above the 7^- state, although feeding of the oblate 6^+ state was not observed in ^{186}Pb.

Band III could be considered as a candidate for an octupole band using the same arguments as Kondev *et al.* [Kon00b], though Popescu *et al.* [Pop97] proposed the two-quasineutron scenario for the 5^- band in ^{182}Pt. Kondev *et al.* deduced from the

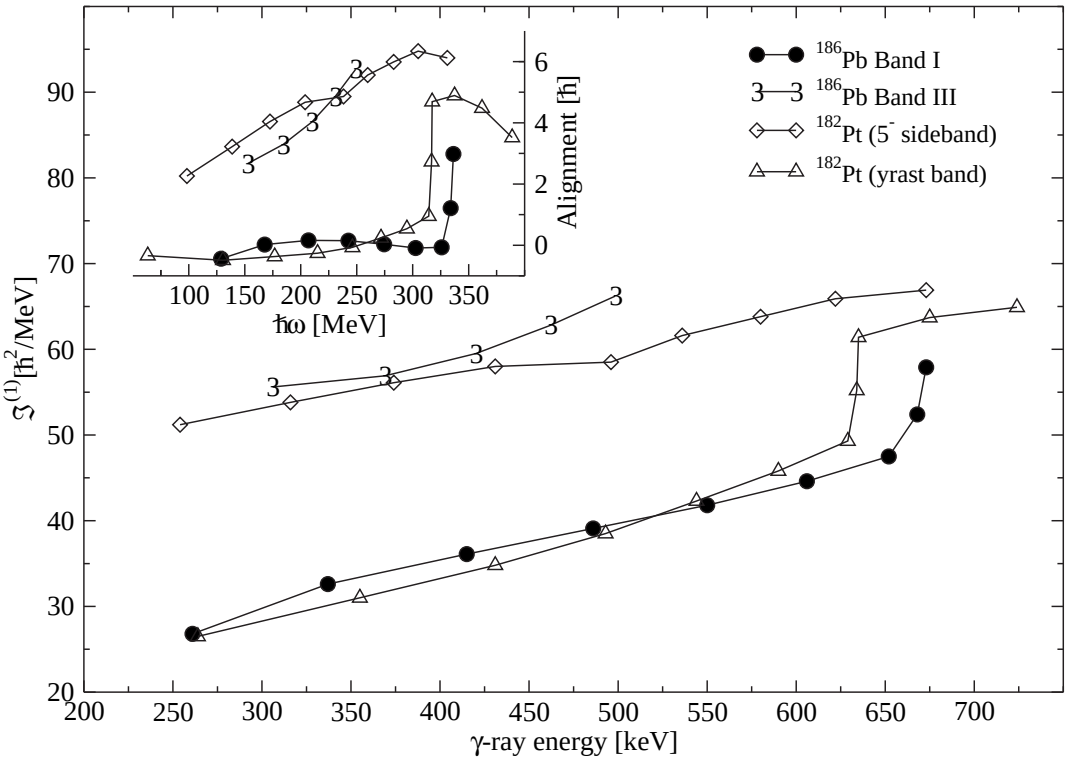

Figure 4.7: Kinematic moment of inertia $\mathcal{J}^{(1)}$ as a function of γ-ray energy for Band I and Band III together with corresponding bands in ^{182}Pt. Aligned angular momenta for these bands with reference parameters of $\mathcal{J}_0$=27.06$\hbar^2/MeV$, $\mathcal{J}_1$=194.67$\hbar^4/MeV^3$ are shown in the inset. Data for ^{180}Hg bands are taken from Reference [Kon00b].

systematics of even-even Os, Pt and Hg nuclei with N=98-106, that the level energies of the negative parity bands relative to the prolate 6^+ state were insensitive to the neutron number. Instead, the negative parity levels seemed to follow the behaviour of the prolate minimum, thus contracting the two-quasineutron scenario. The same phenomenon is observed in Pb isotopes, where the candidate 7^- state in ^{186}Pb follows the behaviour of the prolate minimum as shown in Figure 4.1. This speculation can be continued by noting, that the $E1(I \rightarrow I+1)$ transitions from an octupole band are strongly favored. The non-observation of the $9^- \rightarrow 10^+$ transition can be explained by the energy factor, which favours the 918 keV $9^- \rightarrow 8^+$ transition by factor of 10. The same argument supports the non-observation of the transition feeding the oblate 6^+ state.

4.5 Odd-spin members of the γ-vibrational band

It is difficult to associate Band IV with a two-quasiparticle excitation as it lies relatively low in energy. Little evidence for low-lying odd-spin bands has been observed in the Pb isotopes, except very recently in ^{188}Pb [Dra04]. A few low-lying bands in light Pt isotopes, associated with γ-vibrational structures [Voi90, Pop97, Heb90], resemble Band IV observed in the present work.

Band IV is compared with the corresponding band in ^{188}Pb in Figure 4.8. Due to the complexity of the decay patterns of these candidate γ bands, it is difficult to associate them with any intrinsic structures. However, most of feeding goes to the prolate yrast band, which could suggest something about the intrinsic structure. Also, the change in the level energies of the prolate and these candidate γ bands are very similar. These observations support a prolate intrinsic structure, but it should be noted that the γ vibrations can arise from any minima.

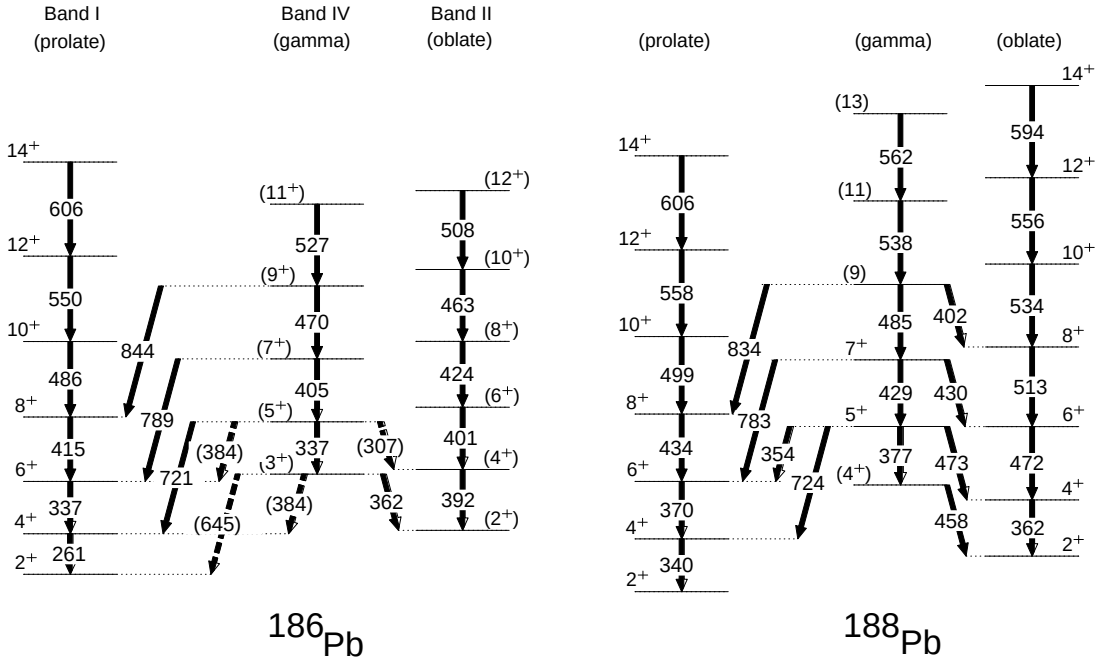

Figure 4.8: Comparison between the proposed γ-vibrational bands in ^{186}Pb and in ^{188}Pb together with the prolate and oblate bands observed in these nuclei. Level schemes have been lined up with the 6_1^+ levels. Data for ^{188}Pb are taken from [Dra04].

Non-observation of the even-spin candidates of the possible γ band suggests that the states are highly non-yrast. This could result from mixing with even-spin states of other K=0 bands. In the presence of mixing, the even-spin states would be pushed up in energy, whereas the odd-spin states remain unperturbed due to the absence of

other positive parity odd-spin states. Such mixing would introduce K=2 admixture into the K=0 bands enabling $M1$ components in the $I \rightarrow I$ transitions. This possibility has been discussed by Dracoulis *et al.* in ^{188}Pb, where the candidate for the odd-spin sequence of the γ band shown in Figure 4.8 was observed [Dra04]. Feeding of the candidate oblate band from the candidate γ band is observed in ^{186,188}Pb, whereas the corresponding inter-band transitions remain unobserved in isotopes$^{182-186}$Pt. This fact would support the interpretation that the oblate states and the even-spin states of the γ band are mixed in ^{186,188}Pb to some extent.

In Figure 4.9, the bands related to Band IV have been compared with the corresponding ones in the isobar ^{186}Pt. Again, the schemes are normalized to the 6_1^+ state. Even though there are deviations in the corresponding intra-band transition energies, the decay patterns of the odd-spin states of the candidate γ bands are fairly similar. In Figure 4.9, the even-spin states of the γ band in ^{186}Pt are also shown to illustrate the clustering of the γ band levels. Those states decay via $I \rightarrow I$ and $I \rightarrow I-2$ transitions to prolate yrast band (not shown in Figure 4.9), but no transitions between the odd-spin states have been observed. It is remarkable, that the lowest even-spin states of theγ band in ^{186}Pt are close to the excitation energies of Band II (when levels have been lined up with the low-lying yrast 6^+ state). This would result in mixing of Band II and the even-spin γ-band states if adapted to ^{186}Pb as they are. The odd-even staggering of the γ band is a signature of γ softness, whereas the clustering of the levels as $(2^+, 3^+)$, $(4^+, 5^+)\ldots$ is a signature of a triaxial rigid rotor. The candidate γ band in ^{186}Pb is associated with the γ bands in neutron-deficient Pt isotopes, which have shown to be soft against γ deformation.

The possibility that Band II consists of the even-spin states of a γ-vibrational band instead of rotational oblate states can not be excluded. However, this would be against the arguments supporting the oblate intrinsic structure of Band II given in Section 4.3.

4.6 Isomeric states in ^{186}Pb

Isomeric states have been observed in several even-even nuclei in the vicinity of^{186}Pb (see for example [Dra84, Dra98, Kac02, Dra04] and references therein). Level systematics for the even-even Pb isotopes reveals a parabolic behaviour of the level energies of the I^π=11^- and I$^\pi$=12^+ isomers with a minimum at N=108. Those isomers have been associated with the oblate $\pi(\mathrm{h}_{9/2}[505]9/2^-)\otimes(\mathrm{i}_{13/2}[606]13/2^+)$ and spherical $\nu(\mathrm{i}_{13/2})^{-2}$ configurations in ^{188}Pb with half-lives of 38 ns and 136 ns, respectively [Dra04]. When extrapolated to ^{186}Pb, an increase in the excitation energy relative to the prolate I^π=10_1^+ state is obvious (see Figure 4.1). Thus the half-lives of those states de-exciting to the I^π=10_1^+ state would be shorter giving rise to almost prompt de-excitation.

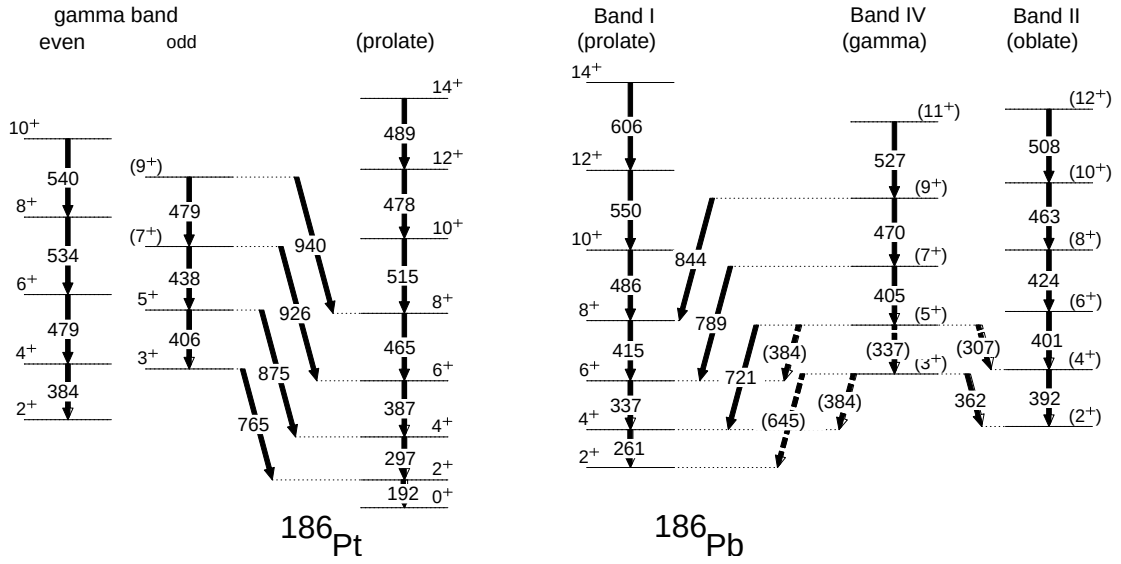

Figure 4.9: Comparison between the proposed γ-vibrational bands in ^{186}Pb and in ^{186}Pt together with the prolate oblate bands observed in these nuclei. Level schemes have been lined up with the 6_1^+ levels. Data for ^{186}Pt are taken from [Heb90].

No evidence for isomeric states was observed in the present work. However, the existence of isomeric states in ^{186}Pb is certainly not excluded by the results in the present work as the transmission time through RITU (500 ns) is considerably longer than the expected lifetimes. Thus, the possible isomeric states would most likely decay in-flight, never reaching the focal-plane detection system with the current reaction. It should also be noted, that the efficiency of the two external Phase I detectors at the focal plane is very low and the spectral response without Compton suppression is limited.

The 8^- isomeric state with a half-life of 1.2 μs, corresponding the Nilsson configuration $\nu((i_{13/2}[624]9/2^+)\otimes(f_{7/2}[514]7/2^-))$, has been found in ^{188}Pb and associated with prolate shape [Dra99]. If this state was considered to be present in ^{186}Pb, it would lie approximately at 2600 keV, i.e. close to the 9^- state. Excluding the 306 keV transition, Band III could be considered to be built on an 8^- state. It is intriguing to consider whether this state could be associated with the isomeric 8^- state in ^{188}Pb. However, the decay pattern of Band III does not correspond to the one for the 8^- isomer in ^{188}Pb and the strong intra-band $M1$ transitions above the 8^- state in ^{188}Pb are clearly not that what is observed in ^{186}Pb. Moreover, the 8^- isomeric state in ^{186}Pb would have a lifetime too long to be detected prompt, even if the gain in transition strength due to the energy factor is taken into account.

5 Summary

The Ge-detector array JUROGAM has been constructed and combined with the RITU gas-filled separator, the GREAT focal-plane set-up and the Total Data Readout system for Recoil-Decay Tagging measurements. This set-up forms the best spectrometer to date for in-beam γ-ray spectroscopic studies of neutron-deficient heavy nuclei. The versatility of the set-up is evident in the diverse running modes available. From the beginning, the JUROGAM has run smoothly and provided magnificent new data for nuclei from the rare earth to the super-heavy region [Had04, Eec05].

In the present work, the set-up has been used to collect high quality in-beam $\gamma\gamma$-coincidence data for ^{186}Pb. Three new bands in ^{186}Pb have been observed and the yrast band has been extended up to the 20^+ state revealing similar upbending of the prolate yrast band as observed in Hg isotopes. The three new bands have been tentatively interpreted to be built on different intrinsic structures. This is the first time non-yrast structures (excluding the 0^+ states) have been observed in ^{186}Pb.

A low-lying even-spin positive parity non-yrast band has been identified. On the basis of observed strong $I \rightarrow I$ and weak $I \rightarrow I-2$ inter-band transitions to the prolate yrast band, this band is associated with an oblate shape. This interpretation is further supported by configuration mixing calculations within the framework of the Interacting Boson Model. The moment of inertia behavior of the band may indicate a shape change towards a more deformed oblate shape.

The tentatively assigned negative parity band in ^{186}Pb is attributed to an octupole vibrational band crossed by two-quasiparticle excitation at higher frequencies. Such an interpretation was earlier proposed for similar bands in the light Hg, Pt and Os nuclei. Due to these similarities, the observation of such a band in ^{186}Pb also provides supporting arguments for the association of the yrast band in ^{186}Pb with the prolate minimum.

The arguments for odd-spin states of a candidate γ band support γ unstable interpretation of ^{186}Pb. However, more extensive data are needed to establish the exact nature of this band.

The Recoil-Decay Tagging technique is by far the most succesful method to probe ^{186}Pb in an in-beam measurement. It will take some time until significant improvements take place. Meanwhile, in-beam conversion electron spectroscopy employing

comparable RDT technology could be used to confirm the spin assignments of non-yrast states made in the present work. Electron measurements would also shed light on the band mixing and on the nature of the low-lying 0^+ states via the observation of $E0$ transitions. The lifetimes of the low-lying 0^+ states are most likely of the order of 100 ps, thus the recoil-shadow method could be employed. Lifetime measurements using the Recoil Distance Doppler-Shift method have very recently been carried out at JYFL. The preliminary analysis reveal that the lifetimes of the three lowest states of the yrast band in ^{186}Pb can be deduced [Gra05].

It will be interesting to see what the front-end digital electronics or combined e^--γ-ray spectrometers can provide for data taking and nuclear structure studies. It also remains to be seen whether the γ-ray tracking array projects [Baz01, Sim05, Del99] will be succesful and what will be the role of radioactive ion beam facilities [Hab98, Fair, Euri, Ria] for the future of γ-ray spectroscopy. Lifetimes and $B(E2)$ values of the low-lying excited states in medium heavy nuclei by using Coulomb excitation method have already been measured employing radioactive ion beams produced by ISOL method [Sch04, Nie04]. However, lots of improvements are still needed in order to apply the method for the light Pb isotopes. The advantage of using Coulomb excitation is the population of the non-yrast states, whereas Recoil Distance Doppler-Shift method is presently usable only for the yrast states. Projectile fragmentation could also be used to probe the low-lying 0^+ states via observation of $E0$ transitions. To conclude, there exists a rich variety of spectroscopic methods to extract more information on ^{186}Pb.

References

[Ala55] G. Alaga, K. Alder, A. Bohr and B.R Mottelson, Dan. Mat. Fys. Medd.**29**, 9 (1955).

[Ald56] K. Alder, A.Bohr, T. Huus, B. Mottelson and A. Winther, Rev. Mod. Phys. **28**, 432 (1956).

[And99a] A.N. Andreyev, N. Bijnens, M. Huyse, P. Van Duppen, M. Leino, T. Enqvist, P. Kuusiniemi, W. Trzaska, J. Uusitalo, N. Fotiades, J.A. Cizewski, D.P. McNabb, K.Y. Ding, C.N. Davids, R.V.F. Janssens, D. Seweryniak, M.P. Carpenter, H. Amro, P. Decrock, P. Reiter, D. Nisius, L.T. Brown, S. Fischer, T. Lauritsen, J. Wauters, C.R. Bingham and L.F. Conticchio, J. Phys. G: Nucl. Part. Phys. **25**, 835 (1999).

[And99b] A.N. Andreyev, D. Ackermann, P. Cagarda, J. Gerl, F. Heßberger, S. Hofmann, M. Huyse, A. Keenan, H. Kettunen, A. Kleinböhl, A. Lavrentiev, M. Leino, B. Lommel, M. Matos, G. Münzenberg, C. Moore, C.D. O'Leary, R.D. Page, S. Reshitko, S. Saro, C. Schlegel, H. Schaffner, M. Taylor, P. Van Duppen, L. Weissman and R. Wyss, Eur. Phys. J. A **6**, 381 (1999).

[And00] A.N. Andreyev, M. Huyse, P. Van Duppen, L. Weissman, D. Ackermann, J. Gerl, F.P. Heßberger, S. Hofmann, A. Kleinböhl, G. Münzenberger, S. Reshitko, C. Schlegel, H. Schaffner, P. Cagarda, M. Matos, S. Saro, A. Keenan, C. Moore, C.D. O'leary, R.D. Page, M. Taylor, H. Kettunen, M. Leino, A. Lavrentiev, R. Wyss and K. Heyde, Nature **405**, 430 (2000).

[And04] A.N. Andreyev, Hivap Calculations, Private Communications, (2004).

[Bal96] G. Baldsiefen, H. Hubel, W. Korten, U.J. van Severen, J.A. Cizewski, N.H. Medina, D.R. Napoli, C. Rossi Alvarez, G. Lo Bianco and S.Signorelli, Z. Phys. A**355**, 337 (1996).

[Bas74] R. Bass, Nucl. Phys. A **231**, 45 (1974).

[Bas80] R. Bass, *Nuclear Reactions with Heavy Ions*, Springer-Verlag, Berlin (1980).

[Bax93] A.M. Baxter, A.P. Byrne, G.D. Dracoulis, R.V.F. Janssen, I.G. Bearden, R.G. Henry, D. Nisius, C.N. Davids, T.L. Khoo, T. Lauritsen, H. Penttilä and M.P. Carpenter, Phys. Rev. C **48**, R2140 (1993).

[Baz01] D. Bazzacco, B. Cederwall, J. Cresswell, G. Duchéne, J. Eberth, W. Gast, J. Gerl, W. Korten, I. Lazarus, R.M. Lieder, J. Simpson and D. Weishaar, *Technical Proposal for an Advanced Gamma Tracking Array for the European Gamma Spectroscopy Community*, http://www.e12.physik.tu-muenchen.de/AGATA/ , edited by J. Gerl and W. Korten, (2001).

[Bea92] C.W. Beausang, S.A. Forbes, P. Fallon, P.J. Nolan, P.J. Twin, J.N. Mo, J.C. Lisle, M.A. Bentley, J. Simpson, F.A. Beck, D. Curien, G. deFrance, D. Duchêne and D Popescu, Nucl. Instr. and Meth. A **313**, 37-49 (1992).

[Ben89] R. Bengttson and W. Nazarewicz, Z. Phys. A**334**, 269 (1989).

[Bij96] N. Bijnens, I. Ahmad, A.N. Andreyev, J.C. Batchelder, C.R. Bingham, D. Blumenthal, B.C. Busse, X.S. Chen, L.F. Conticchio, C.N. Davids, M. Huyse, P. Mantica, H. Penttilä, W. Reviol, D. Seweryniak, P. Van Duppen, W.B. Walters, J. Wauters and B.E. Zimmerman, Z. Phys. A**356**, 3 (1996).

[Boh41] N. Bohr, Phys. Rev. **59**, 270 (1941).

[Boh52] A. Bohr, K. Dan. Vidensk. Mat.-Phys. Meddr. **26**, no. 14 (1952).

[Boh58] A. Bohr, B.R. Mottelson and D. Pines, Phys. Rev. **110**, 936 (1958).

[Bec92a] F.A. Beck, Prog. Part. Nucl. Phys. **28**, 443-461 (1992).

[Bec92b] F.A. Beck, Proc. Workshop Large Gamma-Ray Detector Arrays, Chalk River, Canada, AECL. 10613:364 (1992).

[Ben04] M. Bender, P. Bonche, T. Duguet, P.-H. Heenen, Phys. Rev. C**69**, 064303 (2004).

[Bil86] J. Billowes, Hyperfines interaction **30**, 265 (1986).

[Bin95] K.S. Bindra, P.F. Hua, B.R.S. Babu, C. Baktash, J. Barreto, D.M. Cullen, C.N. Davids, J.K. Deng, J.D. Garret, M.L. Halbert, J.H. Hamilton, N.R. Johnson, A. Kirov, J. Kormicki, I.Y. Lee, W.C. Ma, F.K. McGowan, A.V. Ramayya, D.G. Sarantites, F. Soramel and D. Winchell, Phys. Rev. C**51**, 401 (1995).

[Ced90] B. Cederwall, R. Wyss, A. Johnson, J. Nyberg, B. Fant, R. Chapman, D. Clarke, F. Khazaie, J.C. Lisle, J.N. Mo, J. Simpson and I. Thorslund, Z. Phys. A **337**, 283 (1990).

[Coc98] J.F.C. Cocks, M. Muikku, W. Korten, R. Wadsworth, S. Chmel, J. Domscheit, P.T. Greenlees, K. Helariutta, I. Hibbert, M. Houry, D. Jenkins, P. Jones, R. Julin, S. Juutinen, H. Kankaanpää, H. Kettunen, P. Kuusiniemi, M. Leino, Y. Le Coz, R. Lucas, E. Mergel, R.D. Page, A. Savelius and W. Trzaska, Eur. Phys. J. A **3**, 17 (1998).

[Coh58] B.L. Cohen and C.B. Fulmer, Nucl. Phys. **6**, 547 (1958).

[Del99] M.A. Deleplanque, I.Y. Lee, K. Vetter, G.J. Schmid, F.S. Stephens, R.M. Clark, R.M. Diamond, P.Fallon and A.O. Macchiavelli, Nucl. Instr. and Meth. A **430**, 292 (1999).

[Den95] J.K. Deng, W.C. Ma, J.H. Hamilton, A.V. Ramayya, J. Kormicki, W.B. Gao, X. Zhao, D.T. Shi, I.Y. Lee, J.D. Garrett, N.R. Johnson, D. Winchell, M. Halbert and C. Baktash, Phys. Rev. C **52**, 595 (1995).

[Dew03] A. Dewald,R. Peusquens, B. Saha, P. von Brentano, A. Fitzler, T. Klug, I. Wiedenhöver, M. P. Carpenter, A. Heinz, R. V. F. Janssens, F. G. Kondev, C. J. Lister, D. Seweryniak, K. Abu Saleem, R. Krücken, J. R. Cooper, C. J. Barton, K. Zyromski, C. W. Beausang, Z. Wang, P. Petkov, A. M. Oros-Peusquens, U. Garg and S. Zhu, Phys. Rev. C **68**, 034314 (2003).

[Dra82] G.D. Dracoulis, C. Fahlander and M.P. Fewell, Nucl. Phys. A **383**, 119 (1982).

[Dra84] G.D. Dracoulis, T. Lönnroth, S. Vajda, O.C. Kistner, M.H. Rafailovich, E. Dafni and G. Schatz, Phys. Lett. B **149**, 311 (1984).

[Dra98] G.D. Dracoulis, A.P. Byrne and A.M. Baxter, Phys. Lett. B**432**, 37 (1998).

[Dra99] G.D. Dracoulis, A.P. Byrne, A.M. Baxter, P.M. Davidson, T. Kibédi, T.R. McGoram, R.A. Bark and S.M. Mullins, Phys. Rev. C **60**, 014303 (1999).

[Dra03] G.D. Dracoulis, G.J. Lane, A.P. Byrne, A.M. Baxter, T. Kibédi, A.O. Macchiavelli, P. Fallon and R.M. Clark, Phys. Rev. C **67**, 051301 (2003).

[Dra04] G.D. Dracoulis, G.J. Lane, A.P. Byrne, T. Kibédi, A.M. Baxter, A.O. Macchiavelli, P. Fallon and R.M. Clark, Phys. Rev. C **69**, 054318 (2004).

[Don78] R.J. McDonald and J.E. Draper, Phys. Rev. C **17**, 944 (1978).

[Dup84] P. Van Duppen, E. Coenen, K. Deneffe, M. Huyse, K. Heyde and P. Van Isacker, Phys. Rev. Lett. **52**, 1974 (1984).

[Dup85] P. Van Duppen, E. Coenen, K. Deneffe, M. Huyse and P. Van Duppen, Phys. Lett. B **154**, 354 (1985).

[Dup90] P. Van Duppen, M. Huyse, K. Heyde and J.L. Wood, J. Phys. G: Nucl. Part. Phys. **16**, 441 (1990).

[Eec05] S. Eeckhaudt, P.T. Greenlees, N. Amzal, J.E. Bastin, E. Bouchez, P.A. Butler, A. Chatillon, K. Eskola, J. Gerl, T. Grahn, A. Görgen, R.-D. Herzberg, F.P. Heßberger, A. Hürstel, P.J.C. Ikin, G.D. Jones, P. Jones, R. Julin,

S. Juutinen, H. Kettunen, T.L. Khoo, W. Korten, P. Kuusiniemi, Y. Le Coz, M. Leino, A.-P. Leppänen, P. Nieminen, J. Pakarinen, J. Perkowski, A. Pritchard, P. Reiter, P. Rahkila, C. Scholey, Ch. Theisen, J. Uusitalo, K. Van de Vel and J. Wilson, to be published.

[Euri] European Isotope Separation On-Line Radioactive Ion Beam Facility, http://www.ganil.fr/eurisol/index.html .

[Fair] Facility for Antiproton and Ion Research, http://www.gsi.de/zukunftsprojekt/index_e.html .

[Fan91] B. Fant, R.J. Tanner, P.A. Butler, A.N. James, G.D. Jones, R.J. Poynter, C.A. White, K.L. Ying, D.J.G. Love, J. Simpson and K.A. Connell, J. Phys. G: Nucl. Part. Phys. **17**, 319 (1991).

[Fin72] M. Finger, R. Foucher, J.P. Husson, J. Jastrzebski, A. Johnson, G. Astner, B.R. Erdal, A. Kjelberg, P. Patzelt, A. Hoglund, S.G. Malmskog and R. Henck, Nucl. Phys. A **188**, 369 (1972).

[Fir96] R.B. Firestone, V.S. Shirley, C.M. Baglin, S.Y.F. Chu and J. Zipkin, *Table of Isotopes*, 8^{th} ed. Vol. II, John Wiley & Sons, Inc., New York (1996).

[Fos03] R. Fossion, K. Heyde, G. Thiamova, P. van Isacker, Phys. Rev. C**67**, 024306 (2003).

[Ghi88] A. Ghiorso, S. Yashita, M.E. Leino, L. Frank, J. Kalnins, P. Armbruster, J.-P. Dufour and P.K. Lemmertz, Nucl. Instr. and Meth. A**269**, 192 (1988).

[Goe49] M. Goeppert-Mayer, Phys. Rev. **15**, 1969 (1949).

[Gra05] T. Grahn, Private Communications, (2005).

[Gre04] P.T. Greenlees, A.N. Andreyev, J. Bastin, F. Becker, E. Bouchez, P.A. Butler, J.F.C. Cocks, Y. Le Coz, K. Eskola, J. Gerl, K. Hauschild, K. Helariutta, R.-D. Herzberg, F.-P. Heßberger, R.D. Humphreys, A. Hürstel, D.G. Jenkins, G.D. Jones, P. Jones, R. Julin, S. Juutinen, A. Keenan, H. Kankaanpää, H. Kettunen, T.-L. Khoo, W. Korten, P. Kuusiniemi, M. Leino, A.-P. Leppänen, M. Muikku, P. Nieminen, R.D. Page, T. Page, J. Pakarinen, P. Rahkila, P. Reiter, Ch. Schlegel, C. Scholey, Ch. Theisen, J. Uusitalo, K. Van de Vel, R. Wadsworth and H.-J. Wollersheim, Eur. Phys. J. A **20**, 87 (2004).

[Gör01] A. Görgen, N. Nenoff, H. Hübel, G. Baldsiefen, J.A. Becker, A.P. Byrne, S. Chmel, R.M. Clark, M.A. Deleplanque, R.M. Diamond, P. Fallon, K. Hauschild, I.M. Hibbert, W. Korten, R. Krücken, I.Y. Lee, A.O. Macchiavelli, E.S. Paul, U.J. van Severen, F.S. Stephens, K. Vetter, R. Wadsworth, A.N. Wilson and J.N. Wilson, Nucl. Phys. A **638**, 108 (2001).

[Hab98] D. Habs, O. Kester, T. Sieber, A. Kolbe, J. Ott, G. Bollen, F. Ames, D. Schwalm, R. von Hahn, R. Repnow, H. Podlech, A. Schempp, U. Ratzinger, L. Liljeby, K.-G. Rensfelt, F. Wenander, B. Jonsson, G. Nyman, P. Van Duppen, M. Huyse, A. Richter, G. Shrieder, G. Walter and REX-ISOLDE collaboration, Nucl. Instr. and Meth. B **139**, 128 (1998).

[Had04] B. Hadinia, B. Cederwall, K. Lagergren, J. Blomqvist, T. Bäck, S. Eeckhaudt, T. Grahn, P. Greenlees, A. Johnson, D.T. Joss, R. Julin, S. Juutinen, H. Kettunen, M. Leino, A.-P. Leppänen, R.J. Liotta, P. Nieminen, M. Nyman, J. Pakarinen, E.S. Paul, P. Rahkila, C. Scholey, J. Uusitalo, R. Wadsworth and D.R. Wiseman, Phys. Rev. C **70**, 064314 (2004).

[Har65] S.M. Harris, Phys. Rev. **138**, B509 (1993).

[Hax49] O. Haxel, J.H.D. Jensen and H.E. Suess, Phys. Rev. **15**, 1766 (1949).

[Heb90] G. Hebbinghaus, T. Kutsarova, W. Gast, A. Krämer-Flecken, R.M. Lieder and W. Urban, Nucl. Phys. A **514**, 225 (1990).

[Hee93] J. Heese, K.H. Maier, H. Grawe, J. Grebosz, H. Kluge, W. Meczynski, M. Schramm, R. Schubert, K. Spohr and J. Styczen, Phys. Lett. B **302**, 390 (1993).

[Hei95] P. Heikkinen and E. Liukkonen, 14th International Conference on Cyclotrons and Their Applications, Cape Town, October 8-13 (1995).

[Hel99] K. Helariutta, J.F.C. Cocks, T. Enqvist, P.T. Greenlees, P. Jones, R. Julin, S. Juutinen, P. Jämsen, H. Kankaanpää, H. Kettunen, P. Kuusiniemi, M. Leino, M. Muikku, M. Piiparinen, P. Rahkila, A. Savelius, W.H. Trzaska, S. Törmänen, J. Uusitalo, R.G. Allatt, P.A. Butler, R.D. Page, M. Kapusta Eur. Phys. J. A **6**, 289 (1999).

[Hel05] V. Hellemans, R. Fossion, De Baerdemacker and K. Heyde, Phys. Rev. C **71**, 034308 (2005).

[Hel04] V. Hellemans and K. Heyde, IBM calculations for ^{186}Pb, Private Communications, (2005).

[Hey83] K. Heyde, P. Van Isacker, M. Waroquier, J.L. Wood and R.A. Meyer, Phys. Rep. **102**, 291 (1983).

[Hey88] K. Heyde and R.A. Meyer, Phys. Rev. C **37**, 002170 (1988).

[Hey90] K. Heyde, *The Nuclear Shell Model*, Springer-Verlag, Berlin (1990).

[Hey91] K. Heyde, J. Schietse and C. De Coster, Phys. Rev. C **44**, 2216 (1991).

[Hey92] K. Heyde, C. De Coster, J. Jolie and J.L. Wood, Phys. Rev. C **46**, 541 (1992).

[Hug93] J.R. Hughes, Y. Liang, R.V.F. Janssens, A. Kuhnert, J.A. Becker, I. Ahmad, I.G. Bearden, M.J. Brinkman, J. Burde, M.P. Carpenter, J.A. Cizewski, P.J. Daly, M.A. Deleplanque, R.M. Diamond, J.E. Draper, C. Duyar, B. Fornal, U. Garg, Z.W. Grabowski, E.A. Henry, R.G. Henry, W. Hesselink, N. Kalantar-Nayestanaki, W.H. Kelly, T.L. Khoo, T. Lauritsen, R.H. Mayer, D. Nissius, J.R.B. Oliveira, A.J.M. Plompen, W. Reviol, E. Rubel, F. Soramel, F.S. Stephens, M.A. Stoyer, D. Vo, and T.F. Wang, Phys. Rev. C**47**, 1337 (1993).

[Hus76] J.P. Husson, R. Foucher, A. Knipper, G. Klozt, G. Walter, C.F. Liang, C. Richard-Serre and ISOLDE Collaboration, Proceedings of the International Conference on Nuclei Far From Stability, Cargese, Corsica, 1976, (CERN Report No. 76-13, 1976), p. A85.

[Jai02] H.C. Jain, P. Carlé, A. Källberg, L.O. Norlin, K.-G. Rensfelt, U. Rosengård and B. Fant Nucl. Phys. A **458**, 225 (2002).

[Jan83] R.V.F. Janssens, P. Chowdhury, H. Emling, D. Frekers, T.L. Khoo, W. Kühn, Y.H. Chung, P.J. Daly, Z.W. Grabowski, M. Kortelahti, S. Fraendorf and J.Y. Zhang, Phys. Lett. **131B**, 35 (1983).

[Jen00] D.G. Jenkins, M. Muikku, P.T. Greenlees, K. Hauschild, K. Helariutta, P.M. Jones, R. Julin, S. Juutinen, H. Kankaanpää, N. S. Kelsall, H. Kettunen, P. Kuusiniemi, M. Leino, C.J. Moore, P. Nieminen, C.D. O'Leary, R.D. Page, P. Rahkila, W. Reviol, M.J. Taylor, J. Uusitalo and R. Wadsworth, Phys. Rev. C **62**, 021302 (2000).

[Joh71] A. Johnson, H. Ryde and J. Sztarkier, Phys. Lett. **34B**, 605 (1971).

[Jul01] R. Julin, K. Helariutta and M. Muikku, J. Phys. G: Nucl. Part. Phys. **27**, R109 (2001).

[Jul02] R. Julin, *Lecture notes*, (2002).

[Kan95] J. Kantele, *Handbook of Nuclear Spectroscopy*, Academic Press, London (1995).

[Koi01] H. Koivisto, P. Heikkinen, V. Hänninen, A. Lassila, H. Leinonen, V. Nieminen, J. Pakarinen, K. Ranttila, J. Ärje and E. Liukkonen, Nucl. Instr. and Meth. B **174**, 379 (2001).

[Kac02] M. Kaci, M.-G. Porquet, I. Deloncle, M. Aiche, F. Azaiez, G. Bastin, C.W. Beausang, C. Bourgeois, R.M. Clark, R. Duffait, J. Duprat, B.J.P. Gall, F.

Hannachi, K. Hauschild, M.J. Joyce, A. Korichi, Y. Le Coz, M. Meyer, E.S. Paul, N. Perrin, N. Poffé, N. Redon, C. Schück, H. Sergolle, J.F. Sharpey-Schafer, J. Simpson, A.G. Smith and R. Wadsworth, Nucl. Phys. A**697**, 3 (2002).

[Kon00a] F.G. Kondev, M.P. Carpenter, R.V.F. Janssens, I. Wiedenhöver, M. Alcorta, L. T. Brown, C.N. Davids, T.L. Khoo, T. Lauritsen, C.J. Lister, D. Seweryniak, S.Siem, A.A. Sonzogni, J. Uusitalo, P. Bhattacharyya, S.M. Fischer, W. Reviol, L.L. Riedinger and R. Nouicer, Phys. Rev. C**61**, 044323 (2000).

[Kon00b] F.G. Kondev, R.V.F. Janssen, M.P. Carpenter, K. Abu Saleem, I. Ahmad, M. Alcorta, H. Amro, P. Bhattacharyya, L.T. Brown, J. Caggiano, C.N. Davids, S.M. Fischer, A. Heinz, B. Herskind, R.A. Kaye, T.L. Khoo, T. Lauritsen, C.J. Lister, W.C. Ma, R. Nouicer, J. Ressler, W. Reviol, L.L. Riedinger, D.G. Sarantites, D. Seweryniak, S. Siem, A.A. Sonzogni, J. Uusitalo, P.G. Varmette and I. Wiedenhöver, Phys. Rev. C**62**, 044305 (2000).

[Kra73] K.S. Krane, R.M. Steffen and R.M. Wheeler, Nuclear Data Tables, **11**, 3 (1973).

[Kra88] K.S. Krane, *Introductory Nuclear Physics*, Wiley, New York (1988).

[Kno89] G.F. Knoll, *Radiation Detection and Measurement*, Wiley, New York (1989).

[Laz03] I. H. Lazarus, D.E. Appelbe, P.A. Butler, P.J. Coleman-Smith, J.R. Cresswell, S.J. Freeman, R.-D. Herzberg, I. Hibbert, D.T. Joss, S.C. Letts, R.D. Page, V.F.E. Pucknell, P.H. Regan,J. Sampson, J. Simpson, J. Thornhill and R. Wadsworth, IEEE Trans. on Nucl. Sci. **48**, 12-67 (2001).

[Lei95] M. Leino, J. Äystö, T. Enqvist, P. Heikkinen, A. Jokinen, M. Nurmia, A. Ostrowski, W.H. Trzarska, J. Uusitalo, P. Armbruster and V. Ninov, Nucl. Instr. and Meth. B **99**, 653 (1995).

[Lie99] R.M. Lieder, Ts. Venkova, S. Utzelmann, W. Gast, H. Schnare, K. Spohr, P. Hoernes, A. Georgiev, D. Bazzacco, R. Menegazzo, C. Rossi-Alvarez, G. de Angelis, R. Kaczarowski, T. Rząca-Urban, T. Morek, G.V. Marti, K.H. Maier and S. Frauendorf, Nucl. Phys. A **645**, 465 (1999).

[Ma86] W.C. Ma, A.V. Ramayya, J.H. Hamilton, S.J. Robinson, J.D. Cole, E.F. Zganjar, E.H. Spejewski, R. Bengtson, W. Nazarewicz and J.-Y. Zhang, Phys. Lett. B **167**, 277 (1986).

[Ma93] W.C. Ma, J.H. Hamilton, A.V. Ramayya, L. Chaturvedi, J. Deng, W.B. Gao, Y.R. Jiang, J. Kormicki, X.W. Zhao, N.R. Johnson, J.D. Garrett, I.Y. Lee, C. Baktash, F.K. McGowan, W. Nazarewicz and R. Wyss, Phys. Rev. C **47**, 5 (1993).

[Mat74] E. Der Mateosian and A.W. Sunyar, Atomic Data and Nuclear Data Tables, **13**, 391 (1974).

[May77] F.R. May, V.V. Pashkewich and S Frauendorf, Phys. Lett. B**68**, 113 (1977).

[Mor63] H. Morinaga and P.C. Gugelot, Nucl. Phys. **46**, 210 (1963).

[Nab97] D.P. McNabb, J.A. Cizewski, K.Y. Ding, N. Fotiades, D.E. Archer, J.A. Becker, L.A. Bernstein, K. Hauschild, W. Younes, R.M. Clark, P. Fallon, I.Y. Lee, A.O. Macchiavelli and R.W. MacLeod, Phys. Rev. C **56**, 2474 (1997).

[Naz93] W. Nazarewicz, Phys. Lett. B **305**, 195 (1993).

[Nie04] O. Niedermaier, H. Scheit, V. Bildstein, H. Boie, J. Fitting, R. von Hahn, F. Köck, M. Lauer, U.K. Pal, H. Podlech, R. Repnow, D. Schwalm, C. Alvarez, F. Ames, G. Bollen, S. Emhofer, D. Habs, O. Kester, R. Lutter, K. Rudolph, M. Pasini, P.G. Thirolf, B.H. Wolf, J. Eberth, G. Gersch, H. Hess, P. Reiter, O. Thelen, N. Warr, D. Weisshaar, F. Aksouh, P. Van den Bergh, P. Van Duppen, M. Huyse, O. Ivanov, P. Mayet, J. Van de Walle, J. Äystö, P. A. Butler, J. Cederkäll, P. Delahaye, H.O.U. Fynbo, L.M. Fraile, O. Forstner, S. Franchoo, U. Köster, T. Nilsson, M. Oinonen, T. Sieber, F. Wenander, M. Pantea, A. Richter, G. Schrieder, H. Simon, T. Behrens, R. Gernhäuser, T. Kröll, R. Krücken, M. Münch, T. Davinson, J. Gerl, G. Huber, A. Hurst, J. Iwanicki, B. Jonson, P. Lieb, L. Liljeby, A. Schempp, A. Scherillo, P. Schmidt and G. Walter, Phys. Rev. Lett. **94**, 172501 (2005).

[Nol85] P.J. Nolan, D.W. Gifford and P.J. Twin, Nucl. Instr. and Meth. A**236**, 95 (1985).

[Nol90] P.J. Nolan, Nucl. Phys. A **520**, 657c (1990).

[Nol94] P.J. Nolan, F.A. Beck and D.B. Fossan, Annu. Rev. Nucl. Part. Sci.**45**, 561 (1994).

[Pag01] R.D. Page, D. Ackerman A.N. Andreyev, P. Cagarda, K. Eskola, J. Gerl, P.T. Greenlees, F.P. Heßberger, K. Heyde, S. Hofmann, M. Huyse, P. Jones, D.T. Joss, R. Julin, S. Juutinen, H. Kankaanpää, A. Keenan, H. Kettunen, A. Kleinböhl, P. Kuusiniemi, A. Lavrentiev, M. Leino, M. Matos, A. Melarangi, C.J.P. Moore, M. Muikku, G. Münzenberger, P. Nieminen, C.D. O'leary, P. Rahkila, S. Reshitko, H. Schaffner, C. Schlegel, C. Scholey, M.J. Taylor, J. Uusitalo, K. Van de Vel, P. Van Duppen, L. Weissman, C. Wheldon and R. Wyss, Proceedings of the Third International Conference on Exotic Nuclei and Atomic Masses ENAM2001, Hämeenlinna, Finland, 2-7 July 2001, edited by J. Äystö, P. Dendooven, A. Jokinen and M.

Leino, (ENAM2001 Proceedings, Springer-Verlag Berlin Heidelberg, Germany, 2003) p. 309.

[Pag03] R.D. Page, A.N. Andreyev, D.E. Appelbe, P.A. Butler, S.J. Freeman, P.T. Greenlees, R.-D. Herzberg, D.G. Jenkins, G.D. Jones, P. Jones, D.T. Joss, R. Julin, H. Kettunen, M. Leino, P. Rahkila, P.H. Regan, J. Simpson, J. Uusitalo, S.M. Vincent and R. Wadsworth, Nucl. Instr. and Meth. B **204**, 634 (2003).

[Pak05a] J. Pakarinen, I.G. Darby, S. Eeckhaudt, T. Enqvist, T. Grahn, P.T. Greenlees, F. Johnston-Theasby, P. Jones, R. Julin, S. Juutinen, H. Kettunen, M. Leino, A.-P. Leppänen, P. Nieminen, M. Nyman, R.D. Page, P.M. Raddon P. Rahkila, C. Scholey, J. Uusitalo and R. Wadsworth, Eur. Phys. J. A direct, (2005).

[Pak05b] J. Pakarinen, I.G. Darby, S. Eeckhaudt, T. Enqvist, T. Grahn, P.T. Greenlees, V. Hellemans, K. Heyde, F. Johnston-Theasby, P. Jones, R. Julin, S. Juutinen, H. Kettunen, M. Leino, A.-P. Leppänen, P. Nieminen, M. Nyman, R.D. Page, P.M. Raddon, P. Rahkila, C. Scholey, J. Uusitalo and R. Wadsworth, Phys. Rev. C **72**, 011304 (2005).

[Pau95] E.S. Paul, P.J. Woods, T. Davinson, R.D. Page, P.J. Sellin, C.W. Beausang, R.M. Clark, R.A. Cunningham, S.A. Forbes, D.B. Fossan, A. Gizon, J. Gizon, K. Hauschild, I.M. Hibbert, A.N. James, D.R. LaFosse, I. Lazarus, H. Schnare, J. Simpson, R. Wadsworth and M.P. Waring, Phys. Rev. C**51**, 78 (1995).

[Pen87] J. Penninga, W. H.A. Hesselink, A. Balanda1, A. Stolk, H. Verheul, J. van Klinken, H.J. Riezebos and M.J.A. de Voigt, Nucl. Phys. A**471**, 535 (1987).

[Plo93] A.J.M. Plompen, M.N. Harakeh, W.H.A. Hesselink, G. van 't Hof, N. Kalantar-Nayestanaki, J.P.S. van Schagen, M.P. Carpenter, I. Ahmad, I.G. Bearden1, R.V.F. Janssens, T.L. Khoo, T. Lauritsen, Y. Liang, U. Garg, W. Reviol and D. Ye, Nucl. Phys. A **562**, 61 (1993).

[Pop97] D.G. Popescu, J.C. Waddington, J.A. Cameron, J.K. Johansson, N.C. Schmeing, W. Schmitz, M.P. Carpenter, V.P. Janzen, J. Nyberg, L.L. Riedinger, H. Hübel, G. Kajrys, S. Monaro, S. Pilotte, C. Bourgeois, N. Perrin, H. Sergolle, D. Hojman and A. Korichi, Phys. Rev. C **55**, 1175 (1997).

[Rad00] D. Radford, http://radware.phy.ornl.gov/main.html (2000).

[Rah05] P. Rahkila, to be published (2005).

[Rev03] W. Reviol, C.J. Pechenaya, D.G. Sarantites, P. Fallon and A.O. Macchiavelli, Phys. Rev. C **68**, 054317 (2003).

[Ria] Rare Isotope Accelerator, http://www.orau.org/ria/ .

[Rod04] R.R. Rodríguez-Guzmán, J.L. Egido and L.M. Robledo, Phys. Rev. C **69**, 054319 (2004).

[Ros93] C. Rossi Alvarez, Nucl. Phys. News **3**, 3 (1993).

[Ruy86] J.J. Van Ruyven, J. Penninga, W.H.A. Hesselink, P. Van Nes, K. Allaart, E.J. Hengeveld, H. Verheul, M.J.A. de Voigt, Z. Sujkowskia and J. Blomqvist, Nucl. Phys. A **471**, 535 (1986).

[Sch04] H. Scheit, O. Niedermaier, M. Pantea, F. Aksouh, C. Alvarez, F. Ames, T. Behrens, V. Bildstein, H. Boie, P. Butler, J. Cederkäll, T. Davinson, P. Delahaye, P. Van Duppen, J. Eberth, S. Emhofer, J. Fitting, S. Franchoo, R. Gernhäuser, G. Gersch, D. Habs, R.v. Hahn, H. Hess, A. Hurst, M. Huyse, O. Ivanov, J. Iwanicki, O. Kester, F. Köck, T. Kröll, R. Krücken, M. Lauer, R. Lutter, P. Mayet, M. Münch, U.K. Pal, M. Pasini, P. Reiter, A. Richter, A. Scherillo, G. Schrieder, D. Schwalm, T. Sieber, H. Simon, O. Thelen, P. Thirolf, J. van de Walle, N. Warr, D. Weißhaar and the REX and MINIBALL collaborations, Nucl. Phys. A **746**, 96 (2004).

[Sch80] M.R. Schmorak, Nucl. Data Sheets, **31**, 283 (1980).

[Sea90] G.T. Seaborg and W.D. Loveland, *The Elements Beyond Uranium*, Wiley, New York (1990).

[Sim86] R.S. Simon, K.-H. Schmidt, F.P. Heßberger, S. Hlavac, M. Honusek, G. Münzenberg, H.-G. Clerc, U. Gollerthan and W. Schwab, Z. Phys. A **325**, 197-202 (1986).

[Sim97] J. Simpson, Z. Nucl. A **358**, 139-143 (1997).

[Sim05] J. Simpson, Acta Physica Polonica **36**, 1383 (2005).

[Ste83] Ch. Stenzel, H. Grawe, H. Haas, H. -E. Mahnke and K. H. Maier, Nucl. Phys. A **411**, 248 (1983).

[Ste85] C. Stenzel, H. Grawe, H. Haas, H.-E. Mahnke and K.H. Maier, Z. Nucl. A **322**, 83 (1985).

[Sun89] X.Sun, U. Rosengard, H. Grawe, H. Haas, H. Kluge, A. Kuhnert and K.H. Maier, Z. Phys. A **333**, 281 (1989).

[Trz90] W.H. Trzaska, Nucl. Instr. and Meth. A **297**, 223 (1990).

[Twi83] P.J. Twin, P.J. Nolan, R. Aryaeinejad, D.J.G. Love, A.H. Nelson and A. Kirwan, Nucl. Phys. A **409**, 343C (1983).

[Twi86] P.J. Twin, B.M. Nyakó, A.H. Nelson, J. Simpson, M.A. Bentley, H.W. Cranmer-Gordon, P.D. Forsyth, D. Howe, A.R. Mokhtar, J.D. Morrison, J.F. Sharpey-Schafer and G. Sletten, Phys. Rev. Lett. **57**, 811 (1986).

[Vel03] K. Van de Vel, A.N. Andreyev, R.D. Page, H. Kettunen, P.T. Greenlees, P. Jones, R. Julin, S. Juutinen, H. Kankaanpää, A. Keenan, P. Kuusiniemi, M. Leino, M. Muikku, P. Nieminen, P. Rahkila, J. Uusitalo, K. Eskola, A. Hürstel, M. Huyse, Y. Le Coz, M.B. Smith, P. Van Duppen and R. Wyss, Eur. Phys. J. A **17**, 167 (2003).

[Voi90] M.J.A. De Voigt, R. Kaczarowski, H.J. Riezebos, R.F. Noorman, J.C. Bacelar, M.A. Deleplanque, R.M. Diamond, F.S. Stephens, J. Sauvage and B. Roussière, Nucl. Phys. A **504**, 472 (1990).

[Wau94] J. Wauters, N. Bijnens, H. Folger, M. Huyse, Han Yull Hwang, R. Kirchner, J. von Schwarzenberg and P. Van Duppen, Phys. Rev. C **50**, 2768 (1994).

[Woo92] J.L. Wood, K. Heyde, W. Nazarewicz, M. Huyse and P. Van Duppen, Phys. Rep. **215**, 101 (1992).

[Yam67] T. Yamazaki, Nuclear Data, **3**, 1 (1967).